

Interfacial Energy Anisotropy and Growth Morphologies in Aluminum-Zinc Alloys

THÈSE N° 5128 (2011)

PRÉSENTÉE LE 21 OCTOBRE 2011

À LA FACULTÉ SCIENCES ET TECHNIQUES DE L'INGÉNIEUR

LABORATOIRE DE SIMULATION DES MATÉRIAUX

PROGRAMME DOCTORAL EN SCIENCE ET GÉNIE DES MATÉRIAUX

ÉCOLE POLYTECHNIQUE FÉDÉRALE DE LAUSANNE

POUR L'OBTENTION DU GRADE DE DOCTEUR ÈS SCIENCES

PAR

Jonathan FRIEDLI

acceptée sur proposition du jury:

Prof. F. Stellacci, président du jury

Prof. M. Rappaz, directeur de thèse

Dr S. Akamatsu, rapporteur

Dr M. Plapp, rapporteur

Prof. M. Stampanoni, rapporteur



ÉCOLE POLYTECHNIQUE
FÉDÉRALE DE LAUSANNE

Suisse
2011

“You didn’t think it was gonna be that easy, did you?”

“You know, for a second there, yeah, I kinda did.”

O-Ren Ishii and The Bride

Remerciements

J'ai eu la chance de pouvoir réaliser cette thèse au Laboratoire de Simulation des Matériaux (LSMX) de l'Ecole Polytechnique Fédérale de Lausanne (EPFL) avec le financement du Fonds national Suisse de la recherche scientifique (FNS) que je remercie ici. Malgré ce que pourrait laisser croire la couverture de ce document, une thèse n'est pas l'œuvre d'une seule personne. C'est pourquoi, j'aimerais profiter de ces pages pour remercier les personnes qui, d'une manière ou d'une autre, ont contribué à ce résultat durant ces quatre années et demie.

Ma plus profonde gratitude va à Michel Rappaz qui m'a accueilli au sein de son équipe, m'a donné l'opportunité de faire de la recherche de pointe sous sa direction avisée, de participer activement à l'enseignement, de voyager de par le monde, de rencontrer les meilleurs dans leurs domaines, d'accéder aux techniques les plus modernes et bien plus encore. Par sa passion du travail bien fait, sa confiance infaillible et son amitié, il a su m'accorder toute la liberté et l'encadrement dont j'avais besoin pour donner le meilleur de moi-même. En dehors de son puits de connaissances, "le chef" a su créer et maintenir un laboratoire d'où l'on ne ressort pas seulement avec un diplôme mais avec des amis.

Une aussi bonne ambiance de travail ne pourrait pas régner sans une équipe de choc qui rend chaque jour aussi stimulant que drôle. J'aimerais remercier les membres du LSMX, anciens comme actuels, avec qui j'ai eu le plaisir de travailler. Sans ordre particulier, Frédéric Kohler, Vincent Mathier, Stéphane Vernède, Christoph Niederberger, Denis Favez, Frédéric Gonzales, Amin Rostamian, Mario Salgado, Milan Felberbaum, Simona Moldovan, André Phillion, Jonas Valloton, Léa Deillon, Guillaume Pasche, Luc Rougier, Audrey Chaumartin, Alain Leger, Jérôme Lozat, Hossein Meidani, Meisam Sistaninia, Güven Kurtuldu, Patrick Schloth, Christoph Mondoux, Nicolas Chobaut, Alexandre Durussel, Susan Meuwly et Paolo Di Napoli. Un remerciement tout particulier va à Aurèle Mariaux, mentor de la console, roi des harmoniques sphériques et prince de la "chape", qui n'est jamais à court d'idées et de raisons pour lesquelles elles ne fonctionneront pas, pour sa précieuse aide et tout ce qu'il m'a appris. Merci également à Kamal Shahim, mon collègue de bureau qui a enduré nos nombreuses sessions musicales, tout en restant imperturbable.

J'aimerais exprimer toute ma reconnaissance à Jean-Luc Desbiolles, pour son infinie patience et sa disponibilité lors de ses explications de toutes les subtilités du code de champ de phase; à Jean-Daniel Wagnière, sans qui les expériences d'une telle finesse ne pourraient être abordées avec autant de sérénité et fêtées avec autant d'apéros; ainsi qu'à Emmanuelle Boehm-Courjault, pour son aide en métallo et avec l'EBSD.

My deepest gratitude also goes to Jon Dantzig, for the thrilling collaboration on the phase-field dendrites and seaweeds, his wise guidance, his lack of belief in french mountains and most importantly, his friendship.

Je remercie Arlette Blatti et Anne Roy pour la vie administrative qu'elles nous facilitent ainsi qu'Alain Jacot et Jean-Marie Drezet pour leurs questions toujours pertinentes

et leurs sens de l'humour si particuliers.

Merci à toute l'équipe de l'Atelier de l'Institut des Matériaux et plus particulièrement à Pierre-André Despont, Werner Bronnimann et Adrien Grisendi qui rendent l'impossible possible pour avant-hier.

Pour leurs précieux apports scientifiques, j'aimerais exprimer toute ma reconnaissance à:

Charles-André Gandin, Alain Karma et Arne Dahle pour les fructueuses discussions partagées;

Rohit Trivedi, Ralph Napolitano and Erin Sunseri at Iowa State University in Ames for sharing their knowledge and technique to produce equilibrium shapes; Peter Voorhees and Julie Fife at Northwestern University in Chicago for hosting me and trying to serial section my droplets;

Einen ganz herzlichen Dank geht auch an Markus Rettenmayr und Stephanie Fischer der Friedrich Schiller Universität, für ihre unglaublich nette Gastfreundschaft in Jena und die hoch effiziente und kompetente Hilfe bei dem Tröpfchen Experiment;

Jean Strautmann, Elizabeth Wann, Daniel Bernoulli ($\times 2$), Emmanuelle Rol ($\times 2$), Antoine Emery, Alexandre Durussel, Léonard Antoinat et Lionel Michelet, les étudiants qui par leurs projets de Master, Bachelor ou stage d'été ont contribué à faire progresser mes travaux;

Pierre Burdet et Marco Cantoni du Centre Interdisciplinaire de Microscopie Electronique pour leurs disponibilités et leurs précisions incomparables lors des mesures de gouttelettes par FIB;

Sam McDonald and Frederica Marone for their invaluable support during our days and nights at the TOMCAT beamline of the SLS;

Et enfin aux membres de mon jury de thèse Francesco Stellacci, Silvère Akamatsu, Mathis Plapp et Marco Stampanoni qui ont permis que je mette la touche finale à ce travail par leurs lectures attentives et leurs suggestions constructives.

Sur un plan plus personnel,

Vorrei anche ringraziare la mia tandem partner, Ilaria Vacca per avermi aiutato ad imparare ed esercitare l'italiano e per i numerosi pranzi insieme che mi hanno fatto scoprire la sua visione dell'Italia.

Merci à mes colocos du chemin des Ramiers 18, Tina et Sandra, Ian, Julien, Guillaume et Patricia, Florent, Julien et Martina, Patrick et Patricia, Remo, Dilan, Gustav et Sara ainsi qu'Anouk et Samuel qui ont dû manger bien trop de cervelas et de patates mais qui ont rendu ces repas si diversifiés et intéressants au cours de toutes ces années à Lausanne.

Qu'auraient été cette thèse et ces 10 ans à l'EPFL sans mon coloc, collègue de bureau, partner in crime et co-thésard en fin de droit Jonas Vannod? On ne le saura pas puisqu'il était là. Merci pour son épicurisme indéfectible, son franc-parler légendaire et son amitié inébranlable. Je remercie également sa ptite famille, Virginie, Antoine et Sylvain pour leur accueil inconditionnel et chaleureux et pour toutes nos aventures communes.

Merci à Céline pour son amour et sa patience pendant cette période aussi délicate qu'intense pour elle.

Finalement un tout grand merci à mes parents qui m'ont équipé du bon bagage, montré la voie sans me la dicter, soutenu et encouragé dans les moments difficiles pour eux comme pour moi. C'est à eux et à leur courage que je dédie cette thèse.

Abstract

This thesis presents an investigation aimed at the understanding of the effect of interfacial energy anisotropy on growth morphologies in Al-Zn alloys. Most low alloyed metals form dendritic structures that grow along directions that correspond to low index crystal axes, *e.g.*, $\langle 100 \rangle$ directions in fcc aluminum. However, recent findings [Gon06, Gon08] have shown that an increase in the zinc content of Al-Zn continuously changes the dendrite growth direction from $\langle 100 \rangle$ to $\langle 110 \rangle$ in the (100) plane. At intermediate compositions, $\langle 320 \rangle$ dendrites and textured seaweeds were even observed. The reason for this dendrite orientation transition (DOT) is that this system exhibits a large solubility of the element zinc, which forms hexagonal crystals, in the primary fcc aluminum phase, thus modifying its weak solid-liquid interfacial energy anisotropy γ_{sl} . Due to the complexity of the phenomenology, there is still no satisfactory theory that predicts all the observed microstructures. The goal of this work was to measure the anisotropy of γ_{sl} , to gain further insight in the dendrite growth morphologies and mechanisms in Al-Zn via X-ray tomography and investigate the relationship between dendrite growth directions and the anisotropy of γ_{sl} via phase-field modeling.

The values of the anisotropy in Al-82 wt.% Zn, obtained by equilibrium shape measurement, suggests a DOT in a regime with very low anisotropy, favoring the formation of seaweed structures. The enhanced experimental procedures and observation methods allowed an unprecedented characterization of such complex morphologies. Observations showed that seaweeds are far from random structures. They grow in a (100) symmetry plane by an alternating growth direction mechanism and are therefore less hierarchically ordered than common dendrites.

Phase-field simulations of equiaxed growth of a dilute alloy showed that the DOT is not a continuous transition of growth directions, but rather a competition between the $\langle 100 \rangle$ and the $\langle 110 \rangle$ character of dendrites. However, crystallographic orientation measurements showed that the macroscopic texture evolves as evidenced by Gonzales and Rappaz. This showed that the preferred growth direction is not the same as the final texture of a sample, which is uncommon. Simulations of directional growth showed that seaweeds, which do not appear in equiaxed growth, are in fact produced by the interplay of low or degenerate crystalline anisotropy and the misorientation of the crystal with respect to the thermal gradient.

Keywords: Al-Zn, solid-liquid interfacial energy anisotropy, equilibrium shape measurement, Bridgman solidification, growth morphologies, seaweeds, X-ray tomography, phase-field.

Résumé

Ce travail de thèse présente une étude visant à améliorer la compréhension de l'effet de l'anisotropie de l'énergie interfaciale sur les morphologies de croissance dans les alliages Al-Zn. La plupart des métaux faiblement alliés forment des structures dendritiques croissant selon des directions qui correspondent aux axes du cristal ayant des faibles indices de Miller, par exemple, les directions $\langle 100 \rangle$ dans l'aluminium FCC. Toutefois, de récents résultats [Gon06, Gon08] ont montré qu'une augmentation de la teneur en zinc dans des alliages Al-Zn change continûment la direction de croissance des dendrites, de la direction $\langle 100 \rangle$ vers la direction $\langle 110 \rangle$ dans le plan (100). Aux compositions intermédiaires, des dendrites $\langle 320 \rangle$ ainsi que des seaweeds texturés ont été observés. La raison de cette transition d'orientation de dendrite (DOT) est que ce système présente une grande solubilité de l'élément zinc, qui forme des cristaux hexagonaux, dans la phase primaire d'aluminium FCC, modifiant ainsi sa faible anisotropie d'énergie interfaciale solide-liquide γ_{sl} . En raison de la complexité de la phénoménologie, il n'existe pas encore de théorie satisfaisante prédisant toutes les microstructures observées. L'objectif de ce travail était de mesurer l'anisotropie de γ_{sl} , de mieux comprendre les morphologies et mécanismes de croissance dans les alliages Al-Zn grâce à des observations 3D par tomographie à rayons X et d'étudier la relation entre les directions de croissance des dendrites et l'anisotropie de γ_{sl} par la modélisation en champ de phase.

Les valeurs de l'anisotropie dans un alliage Al-82%pds. Zn, obtenues par mesure de formes d'équilibre, suggèrent une DOT dans un régime avec une très faible anisotropie, favorisant la formation de la structure seaweed. L'amélioration des procédures expérimentales et des méthodes d'observation a permis une caractérisation sans précédent de ces morphologies complexes. Les observations ont montré que les seaweeds sont loin d'être des structures aléatoires. Ils croissent dans un plan de symétrie (100) par mécanisme alternant les directions de croissance et ont donc une structure moins régulière que les dendrites.

Des simulations en champ de phase de la croissance équiaxe d'un alliage faiblement allié ont montré que la transition d'orientation des dendrites n'est pas une transition continue de directions de croissance, mais plutôt une compétition entre le caractère des dendrites à croître selon les directions $\langle 100 \rangle$ ou $\langle 110 \rangle$. Cependant, des mesures d'orientations cristallographiques ont montré que la texture macroscopique évolue comme montré par Gonzales et Rappaz. Cette observation montre que la direction de croissance préférentielle n'est pas la même que la texture finale d'un échantillon, ce qui est rare. Des simulations de croissance dirigée ont montré que les seaweeds, qui n'apparaissent pas lors de la croissance équiaxe, sont en fait produits par l'interaction de l'anisotropie cristalline faible ou dégénérée et de la désorientation du cristal par rapport au gradient thermique.

Mots-clés : Al-Zn, anisotropie de l'énergie interfaciale solide-liquide, mesure de forme d'équilibre, solidification Bridgman, morphologies de croissance, seaweeds, tomographie à rayons-X, champ de phase.

Contents

Remerciements	2
Abstract	5
Résumé	7
1 Introduction	11
1.1 Aluminum-Zinc	11
1.2 Motivation	12
1.3 Objectives and Structure	14
2 Literature Review	17
2.1 Interfacial Energy	17
2.1.1 Anisotropy Description	17
2.1.2 Relations Between Anisotropy Parameters	20
2.1.3 Normalization	20
2.1.4 Wulff Shape and the $\vec{\xi}$ -vector Formalism	21
2.1.5 Curvature	22
2.1.6 Stiffness	23
2.2 Measurement of the Interfacial Energy Anisotropy	25
2.2.1 Equilibrium Shape Measurements	25
2.2.2 Gradient Experiment	26
2.2.3 Molecular Dynamics	26
2.3 Dendritic Growth	28
2.3.1 Fundamentals	28
2.3.2 Phase-field	30
2.4 Dendrite Orientation Transition	33
2.4.1 Flow Induced	34
2.4.2 Velocity Induced	34
2.4.3 Solute Induced	34
2.4.4 Seaweeds	37
3 Experiments	39
3.1 Alloys	39
3.2 Bridgman Solidification	39
3.2.1 Thermal Gradient Characterization	40
3.2.2 Quench	44
3.3 Droplet Experiment	44
3.3.1 Orientation Selection	44

CONTENTS

3.3.2	Isothermal Annealing	45
3.3.3	Gradient Experiment	46
3.4	Characterization	47
3.4.1	Sample Preparation	47
3.4.2	Microscopy	48
3.4.3	Electron Backscattered Diffraction	48
3.4.4	Serial Sectioning	48
3.4.5	X-ray Tomography	49
3.4.6	Focused Ion Beam	52
4	Phase-field modeling	55
4.1	Codes Description	55
4.1.1	Finite Difference Code	55
4.1.2	Finite Elements Code	56
4.1.3	Data analysis	57
4.2	Simulation parametrization	57
4.3	Mesh Anisotropy Assessment and Correction	58
4.3.1	Static	59
4.3.2	Dynamic	64
5	Equilibrium Shapes and Interfacial Energy Anisotropy Measurement	69
5.1	Analytical Calculation of the Equilibrium Shapes	69
5.1.1	Phase-Field Equilibrium Shapes	69
5.1.2	Dendrite Orientation Criterion	71
5.2	Measurement of the Equilibrium Shapes	78
5.2.1	High Zinc Concentration Aluminum Phase Equilibrium Shape . . .	78
5.2.2	Zinc Phase Equilibrium Shape	85
6	Growth Morphologies and Directions	89
6.1	Improvement in the Analysis Method	89
6.2	Microstructural Study of Bridgman Solidified Al-Zn and Al-Cu Alloys . . .	95
6.2.1	Symmetries	95
6.2.2	Primary Trunk Orientation	97
6.2.3	Secondary Arm Bending	99
6.3	Phase-field simulations	101
6.3.1	Equiaxed Growth	102
6.3.2	Columnar Growth	104
7	Conclusion	109
7.1	Synthesis	109
7.2	Perspectives	111
A	Notation	125
B	List of X-ray tomography samples and scanning conditions	129
	Resume	133

Chapter 1

Introduction

Aluminum is the most abundant metal in the Earth's crust, but it has only been used in metallic form since the beginning of the 19th century. In fact, it was long considered to be a precious metal because of the difficulty of reducing aluminum oxide, the form in which it is found in nature. The discovery that allowed aluminum to become the most industrially used non-ferrous metal today was the electrolytic reduction of alumina in a bath of molten cryolite, a process developed simultaneously by Hall in the USA [Hal89] and Héroult in France [Hér86].

In 2010, the primary aluminum world production reached 24,3 million tons, extracted from roughly 100 million tons of bauxite. Despite its abundance and the fact that today, 35% of the worldwide needs in aluminum are covered by recycled material, which saves 95% of the very large energy costs, the price per ton of aluminum is still four times higher than steel.¹

The advent of aluminum in the field of transport and especially aeronautics, but also in electrical transmission, packaging and construction relies on its interesting combination of properties: low density, good formability and corrosion resistance provided by its thin native oxide that prevents further degradation of the material. However, in the pure state, aluminum is a very soft and ductile metal, thus it is almost exclusively used with alloying elements, mainly copper, manganese, silicon, magnesium, zinc and combinations of those, to increase its castability and mechanical properties.

1.1 Aluminum-Zinc

Aluminum-zinc alloys, often also alloyed with magnesium, constitute the 7000 series in the standard designations. They can be precipitation hardened to the highest strengths of any aluminum alloy. In this work, we study the full range of compositions in the Al-Zn binary system. The interest in these alloys here is more fundamental than practical, since when heavily alloyed the low density property is lost because the density of zinc is almost three times larger than aluminum. It is at higher zinc content that binary Al-Zn system becomes more interesting from a solidification point of view.

Indeed, the cigar-shaped eutectic phase diagram (Figure 1.1) provides a large spread of solidification intervals, liquidus slopes and partition coefficients, which produce a broad spectrum of solidification microstructures. Perhaps more interestingly, the high temperature solubility of zinc in aluminum reaches 67 at.% (83 wt.%), allowing for a wide range

¹Source: Zahlenspiegel/L'aluminium en chiffres, Ausgabe/Edition 2011, Aluminium-Verband Schweiz.

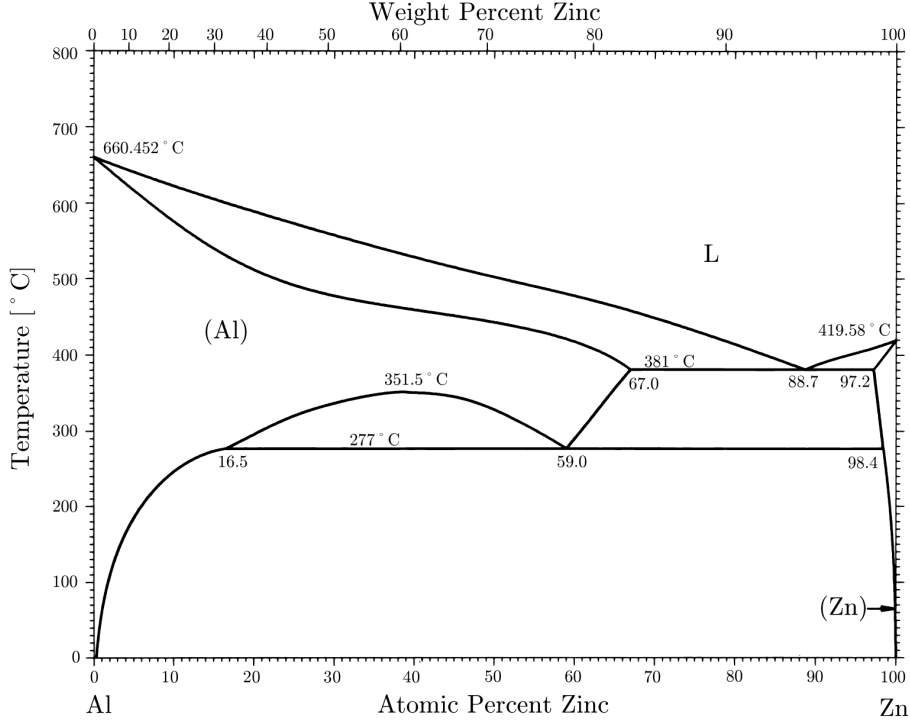


Figure 1.1: Aluminum-Zinc phase diagram, reproduced from Massalski [Mas86]

of primary solid compositions. This feature, in combination with the fact that aluminum is fcc and has a very low anisotropy of the solid-liquid interfacial energy γ_{sl} , whereas zinc is hexagonal and highly anisotropic, leads to a continuous transition in microstructures as the Zn content increases. This recent finding [Gon06] will be explored in more details in this work.

1.2 Motivation

During solidification of most ingots and castings, dendritic microstructures appear. The local compositional variations, as well as the length scales of the various patterns produced by dendritic growth, greatly influence the mechanical properties and homogenization kinetics of the final work piece. Thus, a fundamental understanding of this process is very important for controlling the entire processing chain. The microstructure resulting from the solidification of metals at moderate velocities originates from two concomitant phenomena, the diffusion of solute elements in the liquid and capillarity. The former has a tendency to destabilize the solid-liquid interface whereas capillarity has the opposite effect. The balance between these two competing phenomena produces the microstructural length scale. Numerous studies over the last two decades have demonstrated convincingly that the crystalline anisotropy, and the solid-liquid interfacial energy anisotropy it creates, guide the morphological development into a branched structure that reflects the underlying atomic symmetry of the crystal on a macroscopic scale [Ast09]. Although tremendous progress in the field of solidification has been made in terms of predictive theories and numerical models, closure with certain observations remains problematic and many open questions remain.

Dendrites of most low alloyed metals grow along directions that correspond to low

index crystal axes, *e.g.*, $\langle 100 \rangle$ directions in fcc aluminum. However, in hot-dipped Al-Zn coatings for example, $\langle 320 \rangle$ dendrites were observed by Sémoroz *et al.* [Sem01], thus giving some indication that the hcp zinc element ² could modify the solid-liquid interfacial anisotropy of aluminum at hypoeutectic compositions. Moreover, when trying to produce twin dendrites in laboratory scale experiments, regular $\langle 110 \rangle$ were observed by Henry *et al.* [Hen98b]. No theoretical criterion has yet been found to successfully predict those unusual dendrite orientations. More recently, Gonzales and Rappaz [Gon06] have shown that an increase in the zinc content of Al-Zn continuously changes the dendrite growth direction from $\langle 100 \rangle$ to $\langle 110 \rangle$ in the (100) plane. At intermediate compositions (around 50 wt.%), $\langle 320 \rangle$ dendrites were observed, whereas at the onset and end of this so-called Dendrite Orientation Transition (DOT), textured seaweeds grew with an average orientation following the master curve shown in Figure 1.2. Since these solidification experiments were conducted at low to moderate growth rate, the contribution of attachment kinetics could be discarded as a cause. Therefore, these variations of growth morphologies/directions were attributed to the influence of zinc on the weak anisotropy of the solid-liquid interfacial energy of aluminum. Phase-field simulations for pure materials with varying anisotropy in γ_{sl} suggested that such variations could produce this DOT from $\langle 100 \rangle$ to $\langle 110 \rangle$, even with $\langle 320 \rangle$ dendrites. However, textured seaweeds were not observed [Hax06b]. The term seaweed was first used to describe solidification morphologies by Ihle and Müller-Krumbhaar [Ihl93]. It designates a dense branching morphology less regular than dendrites that is characteristic for vanishing interfacial energy anisotropy and is thus also called degenerate structure. The building blocks of this pattern are local structures called doublons and more complex multiplets whose lifetime is long but finite [Aka95].

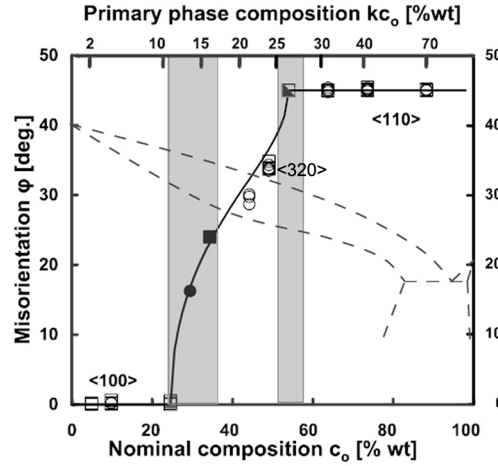


Figure 1.2: Misorientation between the $\langle hk0 \rangle$ direction of dendrites (open symbols) or of the main seaweed texture (filled symbols) and the $\langle 100 \rangle$ direction, as a function of the zinc concentration. The corresponding Al-Zn phase diagram is superimposed with dashed lines on an arbitrary vertical scale for temperature. [Gon06]

We note that this phenomenon is not limited to Al-Zn alloys. Indeed, off-crystal axes dendritic growth has also been observed in magnesium with $\langle 22\bar{4}5 \rangle$ off-basal plane dendrites [Pet89, Pet90] and $\langle 110 \rangle$ and $\langle 111 \rangle$ dendrites in ammonium chloride in aqueous

²although it is the crystal structure which is hexagonal and not the element itself, for the sake of simplicity, we will keep this wording throughout this work

solutions [Cha76]. Nevertheless, although the importance of such phenomena has been demonstrated, it has historically received only little attention.

One of the main obstacles to a better understanding of the solute-induced DOT is that the anisotropy of the solid-liquid interfacial energy is typically very weak for dendrite forming systems, with low entropy of melting and atomically rough interfaces. Thus, even if it is critically needed to make progresses in this field, the precise value of this key parameter controlling microstructural evolution has been measured experimentally only for a very limited number of metallic systems.

1.3 Objectives and Structure

The goals of this work have been elaborated as the continuation of the work by Gonzales [Gon09] in the framework of a Swiss National Science Foundation project to study solidification morphologies. The general aim is to combine newly developed and available techniques to extend the understanding of the DOT observed by Gonzales and Rap-paz [Gon06]. In particular, this task was divided into three tasks.

Due to the paucity of experimental data found in literature for this property, the first objective was a direct determination of the anisotropy of the solid-liquid interfacial energy, γ_{sl} , via the observation of quenched liquid droplets under near-equilibrium conditions in highly alloyed Al-Zn. The implementation of a technique recently developed by Liu *et al.* [Liu01, Nap02, Nap04] and its combination with a gradient remelting experiment enabled the production of very fine liquid droplets entrapped in a single crystal matrix. After quenching, X-ray tomography and focused ion beam serial sectioning have allowed the measurement of the resulting equilibrium shapes and the calculation of the associated γ_{sl} anisotropy parameters through the $\vec{\xi}$ -vector formalism.

The dendrite growth morphologies and mechanisms in Al-Zn were further elucidated using X-ray tomography on quenched Bridgman specimens. These techniques were applied for the first time in this work to study the detailed evolution of microstructure in a wide range of Al-Zn alloys. The 3D reconstruction capabilities allowed the detailed observation of seaweeds in a metallic alloy for the first time. Combining crystallographic analysis by electron backscattered diffraction with the X-ray tomography data further enabled us to clearly identify important differences between the macroscopic texture and the actual growth directions of individual dendrites in these alloys.

Previous computational studies of the role of crystalline anisotropy in pattern selection have been limited to two dimensional studies, pure materials, or only very simple descriptions of the γ_{sl} anisotropy. In this work, the relationship between dendrite growth direction and the anisotropy of the solid-liquid interfacial energy was investigated via phase-field modeling of 3D equiaxed and columnar growth in dilute alloys, using a generalized expression for the interfacial energy anisotropy to broaden our understanding of this phenomenon.

The presentation follows in 7 chapters. Chapter 2 provides the reader with an overview of the previous theoretical and experimental studies on the topic. It will introduce the fundamentals of solidification needed to understand more deeply the problem of interfacial energy anisotropy and its role in the dendrite orientation transition. As modeling plays a key role in the interpretation of the experimental findings, emphasis will also be given on the phase-field method, which will be used in this work.

The experimental procedures and characterization methods used to analyze the various

microstructures encountered will be presented in Chapter 3. Experimental procedures will be stressed since they are the key for producing microstructures that isolate the important phenomena. An emphasis will also be made on the 3D characterization methods that constitute the main observation tools of this work, namely synchrotron based X-ray tomography and focused ion beam serial sectioning.

Chapter 4 is dedicated to the problem of modeling low anisotropy and low undercooling dendritic solidification using phase-field. Changes in the microstructures being very sensitive to the anisotropy parameters, the method to correctly consider the effect of the mesh, which perturbs the crystalline anisotropy through its discrete description, will be the main focus of this chapter.

Chapter 5 presents the results obtained in the analytical investigations of the equilibrium shape, which leads to the determination of the interfacial energy anisotropy parameters. The consequences of this anisotropy and its relation to the growth mechanisms, directions, texture and morphologies are treated in Chapter 6. Particular attention will be given to the analysis of the complex textured seaweed microstructures.

Finally, Chapter 7 will provide a synthesis of the obtained results and the conclusions that they allow, as well as an outlook for future investigations that could follow and expand the findings of this work.

Chapter 2

Literature Review

2.1 Interfacial Energy

In solidification, most pattern forming mechanisms are somehow linked to the properties of the solid-liquid interface. An interface is mainly a perturbation in the equilibrium structure between two phases in contact. Not belonging to either of the phases, atoms at the interface have to accommodate for the structural differences between the solid and the liquid. The integral of the excess volumetric Gibbs free energy across the interface per unit area defines the solid-liquid interfacial energy, γ_{sl} . The consequence of this additional energy is that a system will tend to minimize the area of the interface if γ_{sl} is uniform. In such an isotropic case, the driving force of interface movement, the interfacial tension σ_{sl} is equivalent to the interfacial energy. In most cases however, since the solid is crystalline, γ_{sl} is anisotropic (orientation dependent). This equivalence is not valid anymore and this has important consequences when it comes to microstructure formation.

Above a critical radius, a seed in an undercooled melt continues to grow freely until growth with a nearly spherical shape becomes unstable. Once this point is reached, the disturbances to the shape are amplified and preferred growth directions expressing the underlying crystal symmetries appear. This phenomenon originates from the anisotropy of either the solid-liquid interfacial energy or the attachment kinetics [Cha76]. In non-facetted metallic alloys growing at low velocity, the latter does not play a significant role and the instability of the solid-liquid interface leading to the formation of dendrites is influenced by the anisotropy of the solid-liquid interfacial energy. The details of dendrite growth mechanism will be given in Section 2.3, but first the origin of the phenomenon will be described.

2.1.1 Anisotropy Description

In the shape stability analysis introduced by Mullins and Sekerka [Mul63], a crystal growing by diffusional process is subject to small perturbations of its shape. For an originally spherical crystal, a point $r(\theta, \varphi)$ on its surface would be displaced from $r = R$ to

$$r(\theta, \varphi) = R + \delta_l Y_l^m(\theta, \varphi) \quad (2.1)$$

where Y_l^m are the spherical harmonics ¹ with $\theta \in [0, \pi]$ and $\varphi \in [0, 2\pi]$, the polar and azimuthal coordinates, respectively, and where δ_l is the amplitude of the deformation. As

¹ $Y_l^m(\theta, \varphi) = \sqrt{\frac{2l+1}{4\pi} \frac{(l-|m|)!}{(l+|m|)!}} P_l^m(\cos \theta) e^{im\varphi}$ where P_l^m are the associated Legendre polynomials.

mentioned above, in the case considered here, the main contribution to the anisotropy in the initial stage of the growth stems from the interfacial energy.

One of the first way the anisotropy of the interfacial energy was described thus was

$$\gamma_{sl}(\theta, \varphi) = \gamma_{sl}^0 \left[1 + \frac{1}{2} \sum_{l,m} \delta_l^m Y_l^m(\theta, \varphi) \right] \quad (2.2)$$

where γ_{sl}^0 is the orientation averaged interfacial energy.

Based on group theory, Chan *et al.* [Cha76] conjectured that one should not consider a random perturbation of the shape represented by an arbitrary spherical harmonic Y_l^m but a restricted set which is determined from the physical properties responsible for the initial anisotropic growth, that is, the solid crystal structure and its symmetry.

These authors thus showed how to obtain the so-called cubic harmonics, a symmetry-adapted basis set for variables defined over the unit sphere with cubic point symmetry. Cubic harmonics are a linear combination of spherical harmonics and are orthogonal because of the properties of the spherical harmonics themselves. The combination of l and m respecting the symmetry are thus restricted to $l = 4, 6, 8, 10, \dots$ and $m = 0, \pm 4, \pm 8, \pm 12, \dots$ with $|m| \leq l$.

The three lowest order cubic harmonics, apart from $\mathcal{K}_0 = 1$, are thus

$$\mathcal{K}_4(\theta, \varphi) = \left[Y_4^0 + \sqrt{\frac{5}{14}} (Y_4^4 + Y_4^{-4}) \right] / N_4 \quad (2.3)$$

$$\mathcal{K}_6(\theta, \varphi) = \left[Y_6^0 - \sqrt{\frac{7}{2}} (Y_6^4 + Y_6^{-4}) \right] / N_6 \quad (2.4)$$

$$\mathcal{K}_8(\theta, \varphi) = \left[Y_8^0 + \sqrt{\frac{14}{99}} (Y_8^4 + Y_8^{-4}) + \sqrt{\frac{65}{198}} (Y_8^8 + Y_8^{-8}) \right] / N_8 \quad (2.5)$$

The N_i are non-essential normalization constants that will be covered in Section 2.1.3. Although \mathcal{K}_4 , \mathcal{K}_6 and \mathcal{K}_8 provide a basis for describing the interfacial energy as follows

$$\gamma_{sl}(\theta, \varphi) = \gamma_{sl}^0 \left[1 + \delta_4 \mathcal{K}_4(\theta, \varphi) + \delta_6 \mathcal{K}_6(\theta, \varphi) + \delta_8 \mathcal{K}_8(\theta, \varphi) \right] \quad (2.6)$$

this notation is rarely used in literature due to its complexity. Fehlner and Vosko [Feh76] proposed an alternative basis much more appropriate for computations. They defined the two functions respecting the fourfold symmetry of cubic crystals:

$$\begin{aligned} Q &= n_x^4 + n_y^4 + n_z^4 \\ &= \mu^4 + (1 - \mu^2)^2 [\cos(4\varphi) + 3] / 4 \\ &= \sin^4 \theta (\cos^4 \varphi + \sin^4 \varphi) + \cos^4 \theta \end{aligned} \quad (2.7)$$

$$\begin{aligned} S &= n_x^2 n_y^2 n_z^2 \\ &= \mu^2 (1 - \mu^2)^2 [1 - \cos(4\varphi)] / 8 \\ &= \sin^4 \theta \cos^2 \theta \sin^2 \varphi \cos^2 \varphi \end{aligned} \quad (2.8)$$

with $\mu = \cos^2(\theta)$ and where the n_i 's are the Cartesian components of the unit normal vector \vec{n} . These authors showed that \mathcal{K}_4 is a linear function of Q , \mathcal{K}_6 a linear function of Q and S and \mathcal{K}_8 a quadratic function of Q and linear function of S as follows

$$\mathcal{K}_1(\theta, \varphi) = \left[Q - \frac{3}{5} \right] / N_1 \quad (2.9)$$

$$\mathcal{K}_2(\theta, \varphi) = \left[3Q + 66S - \frac{17}{7} \right] / N_2 \quad (2.10)$$

$$\mathcal{K}_3(\theta, \varphi) = \left[65Q^2 - 94Q - 208S + 33 \right] / N_3 \quad (2.11)$$

Again, the N_i 's are non-essential normalization constants and the interfacial energy can be described as

$$\gamma_{sl}(\vec{n}) = \gamma_{sl}^0 \left[1 + \varepsilon_1 \left(Q - \frac{3}{5} \right) + \varepsilon_2 \left(3Q + 66S - \frac{17}{7} \right) + \varepsilon_3 \left(65Q^2 - 94Q - 208S + 33 \right) \right] \quad (2.12)$$

This expression could of course be expanded to higher orders but since this is of no practical use here the reader is referred back to the original paper by Fehlner and Vosko [Feh76]. Even though the third order is used in very specific cases where special growth direction such as $\langle 320 \rangle$ dendrites are needed [Nie06a], most authors use (2.12) only up to the second order and this will also be the case hereafter.

Most solidification models having first been developed in 2D, there is another description widely used in literature. In fact, in 2D, the interfacial energy is given by $\gamma_{sl} = \gamma_{sl}^0 [1 + \varepsilon_n \cos(n\varphi)]$, with $n = 4$ in the case of cubic symmetry. The direct extension of this relation into 3D usually takes the form

$$\gamma_{sl}(\theta, \varphi) = \gamma_{sl}^0 \left[1 + \varepsilon_4 \left(4 \left(\sin^4 \theta (\cos^4 \varphi + \sin^4 \varphi) + \cos^4 \theta \right) - 3 \right) \right] \quad (2.13)$$

which retrieves the 2D function in the symmetry planes $x-y$, $x-z$ and $y-z$ (*i.e.*, when $\theta = \pi/2$, $\varphi = 0$ and $\varphi = \pi/2$ respectively). Introducing (2.7) in (2.13), one recovers the relation most commonly encountered in literature.

$$\gamma_{sl}(\vec{n}) = \gamma_{sl}^0 \left[1 + \varepsilon_4 (4Q - 3) \right] \quad (2.14)$$

or equivalently

$$\gamma_{sl}(\vec{n}) = \gamma_{sl}^0 (1 - 3\varepsilon_4) \left[1 - \frac{4\varepsilon_4}{1 - 3\varepsilon_4} Q \right] \quad (2.15)$$

A simple function analysis shows that if ε_4 is positive, γ_{sl} has its maximum and minimum in the $\langle 100 \rangle$ and $\langle 111 \rangle$ crystallographic directions, respectively, and inversely if ε_4 is negative. Thus no $\langle 110 \rangle$ dendrites can be generated from such an anisotropy. To the author's knowledge, only three papers have used a higher order extension of (2.14), [Hoy01], [Hoy02] and [Mor02], with

$$\gamma_{sl}(\vec{n}) = \gamma_{sl}^0 [1 + \varepsilon_4 (4Q - 3) + \varepsilon_6 (M + 30S)] \quad (2.16)$$

with $M = n_x^6 + n_y^6 + n_z^6$. This relation has however never been used again since then because, as opposed to Fehlner and Vosko's expansion (2.12), the terms in (2.16) are not orthogonal to each other [Ast02].

The mathematical construction that allows to represent the orientation-dependent interfacial energy by a contour in 2D and a surface in 3D is simply given by $\vec{\rho}(\vec{n}) = C\gamma_{sl}(\vec{n})\vec{n}$: it is the so-called γ -plot and C is a proportion factor.

2.1.2 Relations Between Anisotropy Parameters

Since so many different descriptions for the interfacial energy are available in literature, it is necessary to be able to compare them. Unfortunately, given the very different approaches used to derive those expressions, the comparison is not always strictly possible and can even be impossible.

Due to their very similar nature, (2.6) and (2.12) can directly be compared and their anisotropy parameters $(\delta_4, \delta_6, \delta_8)$ and $(\varepsilon_1, \varepsilon_2, \varepsilon_3)$ related as follows

$$\begin{aligned} \delta_4 &= \frac{4\sqrt{\pi}}{15}\varepsilon_1 & \delta_6 &= \frac{8\sqrt{\frac{\pi}{13}}}{7}\varepsilon_2 & \delta_8 &= 8\sqrt{\frac{\pi}{17}}\varepsilon_3 \\ \varepsilon_1 &= \frac{15}{4\sqrt{\pi}}\delta_4 & \varepsilon_2 &= \frac{7}{8\sqrt{\frac{\pi}{13}}}\delta_6 & \varepsilon_3 &= \frac{1}{8\sqrt{\frac{\pi}{17}}}\delta_8 \end{aligned} \quad (2.17)$$

When attempting to put into relation the two most widely used expressions, (2.12) and (2.14), no straightforward correspondence appears between their first order expansions. The dependences are the same but $\gamma_{s\ell}^0$ is modified by ε_4 as shown in the reformulation of Equation (2.14)

$$\gamma_{s\ell}^0 \left[1 + \underbrace{\varepsilon_4 \left(4Q - \frac{12}{5} \right)}_{4 \times \varepsilon_1 (Q - 3/5)} - \frac{3}{5}\varepsilon_4 \right]$$

It also shows that ε_4 has a roughly four times stronger effect on Q , but the relation is not exact because of the non-matching constant terms multiplying ε_1 and ε_4 respectively. Thus, only an approximate relation can be established

$$\varepsilon_4 \approx 4\varepsilon_1 \quad (2.18)$$

and there is also no combination of ε_1 and ε_2 that would mimic the effect of ε_4 and only approaching estimations could be made.

Likewise, since (2.16) uses yet another construction, the comparison between this representation and the others is impossible.

Consequently, great care has to be taken when comparing results of anisotropy parameter determination or usage. Some can be compared, others however need to be re-evaluated with the appropriate expression to become comparable.

2.1.3 Normalization

As mentioned above, the cubic harmonics were given with normalization coefficients N_i . Chan *et al.* [Cha76] say that N_i are set such that the functions \mathcal{K}_i have unit amplitudes in the direction $\theta = 0^\circ$, $\varphi = 0^\circ$. Fehlner and Vosko [Feh76] then again set them in order to have

$$\int d\Omega (\mathcal{K}_i)^2 = 4\pi \quad (2.19)$$

which implies that the mean amplitude is one. Nevertheless, in literature N_i 's are almost always set to one. Yet, authors mention anisotropy strengths, without necessarily defining how this deviation from isotropy is considered or with respect to which formulation. This notion needs to be defined.

Table 2.1 shows the value taken by Q , S and 3 \mathcal{K}_i 's in the 3 crystallographic directions, where the maxima and minima of these functions are found. As one can tell from this table, the effect of the parameters ε_i 's is quite different. Equation (2.14) has the convenient property that when ε_4 is set to 0.01, the maximum of γ_{sl} is 1% above the isotropic situation. This could be one definition of the anisotropy strenght, *i.e.*, the difference between the maximum amplitude and the isotropic case. However, as we will see later on, the resulting properties are not only sensible to the maximum of the function, but also to its variation with respect to the minimum. We thus suggest that the strenght of anisotropy should consider the amplitude difference between the maximum and the minimum. The normalization would thus generate N_i 's that constrain the amplitude difference to unity. The corresponding values are presented in the last line of Table 2.1.

Table 2.1: Values taken by Q , S and three cubic harmonics in 3 crystallographic directions. Maxima are given in bold and minima in gray. The normalization coefficients N_i 's yield \mathcal{K}_i with amplitude differences of 1.

Dir.	Q	S	ε_4	ε_1	ε_2
			$4Q - 3$	$Q - 3/5$	$3Q + 66S - 17/7$
$\langle 100 \rangle$	1	0	1	2/5	4/7
$\langle 110 \rangle$	1/2	0	-1	-1/10	-13/14
$\langle 111 \rangle$	1/3	1/27	-5/3	-4/15	64/63
N_i			8/3	2/3	35/18

Keeping in mind that (2.12) and (2.14) have already widely been used as is, the formulations are unlikely to change amongst the authors, be it only for reproducibility reasons. Hence, these factors just have to be taken into account when comparing anisotropy strength a posteriori. In other words, 1% anisotropy corresponds to $\varepsilon_4 = 0.00375$ or $\varepsilon_1 = 0.015$, where the factor 4 from (2.18) is retrieved. Inversely, $\varepsilon_4 = 0.01$ would mean that the anisotropy strength is 2.67% with this definition.

Nonetheless, as soon as several terms of the expansion of γ_{sl} are combined, *i.e.* $\varepsilon_1 \neq 0$ and $\varepsilon_2 \neq 0$, the maxima and minima change and so do the normalization factors. Giving an anisotropy strength does then not make sense anymore and a set of ε_i should be given to characterize anisotropy.

2.1.4 Wulff Shape and the $\vec{\xi}$ -vector Formalism

When a crystal is in equilibrium with a liquid (or vapor) phase, free from any contact or body forces, Wulff's theorem [Wul01] states that the distance $d(\vec{n})$, projection on the normal \vec{n} of the vector from the gravity center to the point on the surface with a normal \vec{n} (see Figure 2.1), is proportional to the corresponding free energy per unit area, $\gamma_{sl}(\vec{n})$. In other words, $d(\vec{n})/\gamma_{sl}(\vec{n})$ is constant and the equilibrium shape can be geometrically constructed as the inner envelope of the planes going through a point $\vec{\rho}(\vec{n})$ of the γ -plot and perpendicular to \vec{n} . The proposed geometrical construction, the Wulff-plot, is a simple geometrical principle, but difficult to realize in three dimensions. Cahn and Hoffman [Hof72] proposed an easier concept to manipulate, the $\vec{\xi}$ -vector formalism,

which is defined as

$$\vec{\xi}_{sl}(\vec{n}) = \nabla [\gamma_{sl}(\vec{n})r] = \gamma_{sl}(\vec{n})\vec{n} + \frac{d\gamma_{sl}}{d\vec{n}} - \left(\frac{d\gamma_{sl}}{d\vec{n}} \cdot \vec{n} \right) \vec{n} \quad (2.20)$$

where $\vec{r} \in \mathbb{R}^3$ is the space vector which should not be confused with the position vector $\vec{\rho}(\vec{n})$ of the γ -plot. This equation satisfies

$$\vec{\xi}(\vec{n}) \cdot \vec{n} = \gamma_{sl}(\vec{n}), \quad \forall \vec{n} \quad (2.21)$$

which is Wulff's theorem and the parametric surface $\vec{\rho}_{\xi}(\vec{n}) = \vec{\xi}(\vec{n})$ is homothetic to the equilibrium shape of a crystal with interfacial energy $\gamma_{sl}(\vec{n})$. The so-called $\vec{\xi}$ -plot thus describes the equilibrium shape up to a scaling factor.

Using the equations from Section 2.1.1 for γ_{sl} , this formalism is then a very effective tool to go back and forth between the equilibrium shape and the γ -plot. Please note that, by construction, a given direction \vec{n} does not correspond to the normal to the γ -plot at point $\gamma_{sl}(\vec{n})\vec{n}$, but is parallel to the normal to the $\vec{\xi}$ -plot at point $\vec{\xi}(\vec{n})$ [Hof72].

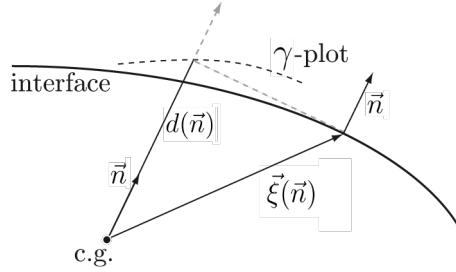


Figure 2.1: Schematic representation of the reverse Wulff construction for determining the γ -plot starting from the equilibrium shape. c.g. is the center of gravity of the equilibrium shape.

2.1.5 Curvature

Another quantity used to describe a surface or interface is its curvature. At a given point on a surface, there is always one particular choice of orthogonal directions on the tangent plane where the radii of curvature, R_1 and R_2 , attain their maximum and minimum values simultaneously and those define the principal curvatures K_1 and K_2 . Those are the diagonal elements of the curvature tensor matrix. The two important invariants of this tensor are the mean and the Gaussian curvatures. They are defined as half the trace of the matrix, $H = \frac{1}{2}(K_1 + K_2)$ for the mean curvature and the determinant $K = K_1 K_2$ for the Gaussian curvature.

Depending on the concerned surface, the curvatures of interest are presented differently. We will divide it into the analysis of equilibrium shapes and of fully developed growth structures.

For equilibrium shapes where γ_{sl} is a known function such as (2.12), the two principal curvatures present the main interest. For simple cases where γ_{sl} depends on ε_1 only, convexities of the equilibrium shape are such that the two principal radii of curvature of the equilibrium shape are minimum and equal along $\langle 100 \rangle$. However when the development of γ_{sl} goes up to the second order or more, this is no longer the case and the principal curvatures might not be maximum and equal along a given direction \vec{n} . (Please note that

“a” direction \vec{n} means all the equivalent directions \vec{n} that respect the cubic symmetry, e.g., when $\vec{n} = (\frac{1}{\sqrt{2}}, \frac{1}{\sqrt{2}}, 0)$, this includes the twelve $\langle 110 \rangle$ directions). In such complex cases, all four curvatures of the equilibrium shape for any expression of γ_{sl} can be established using the following relationships [Gra99]

$$K = \frac{eg - f^2}{EG - F^2} \quad H = \frac{eG - 2fF + gE}{2(EG - F^2)} \quad K_i = H \pm \sqrt{H^2 - K} \quad (2.22)$$

where E, F, G and e, f, g are the coefficients of the first, respectively second, fundamental forms of the equilibrium shape crystal surface. Taking into account the fact that \vec{n} is normal to the ξ -plot at point $\vec{\xi}(\vec{n})$, these expressions are given by

$$E = \frac{\partial \vec{\xi}}{\partial \theta} \cdot \frac{\partial \vec{\xi}}{\partial \theta} \quad F = \frac{\partial \vec{\xi}}{\partial \theta} \cdot \frac{\partial \vec{\xi}}{\partial \varphi} \quad G = \frac{\partial \vec{\xi}}{\partial \varphi} \cdot \frac{\partial \vec{\xi}}{\partial \varphi} \quad (2.23)$$

$$e = -\frac{\partial \vec{\xi}}{\partial \theta} \cdot \frac{\partial \vec{n}}{\partial \theta} \quad f = -\frac{1}{2} \left(\frac{\partial \vec{\xi}}{\partial \theta} \cdot \frac{\partial \vec{n}}{\partial \varphi} + \frac{\partial \vec{\xi}}{\partial \varphi} \cdot \frac{\partial \vec{n}}{\partial \theta} \right) \quad g = -\frac{\partial \vec{\xi}}{\partial \varphi} \cdot \frac{\partial \vec{n}}{\partial \varphi} \quad (2.24)$$

where again θ and φ are the polar and azimuthal angles of the spherical coordinate system, respectively.

When looking at developed structures, the mean curvature is important because it sets the concentration at the solid-liquid interface via the Gibbs-Thomson equation. The mean and Gaussian curvatures nonetheless play an essential role during the interface evolution since the rate of change of curvatures is related to both [Dre90]. In addition, both are necessary to characterize the shape of an interface. For example, a flat interface and a saddle-shaped interface can both have a mean curvature of zero, but will have different Gaussian curvatures.

A convenient way to visualize curvature data of dendrites has been suggested by Voorhees and co-workers [Men03], namely an interfacial shape distribution (ISD), which is a probability density map of (K_1, K_2) pairs measured on each point of the interface in a structure. Such an ISD (see Figure 2.2) presents four regions:

1. represents elliptic patches where $H > 0$ and $K > 0$.
2. represents hyperbolic patches where $H > 0$ and $K < 0$.
3. represents hyperbolic patches where $H < 0$ and $K < 0$.
4. represents elliptic patches where $H < 0$ and $K > 0$.

There can be no probability below $K_1 = K_2$ since, by definition, $K_2 \geq K_1$.

2.1.6 Stiffness

When it comes to preferred growth directions of dendrites, it is commonly stated in most solidification textbooks that dendrites in cubic metals grow along $\langle 100 \rangle$ directions, since these directions correspond to the maxima of γ_{sl} . This is true in some cases when the anisotropy of γ_{sl} is strong, e.g., for nickel-base alloys, but not always. Furthermore, this statement is incorrect and it is more precise to say that dendrites grow from the “most highly curved”² parts of the equilibrium shape crystal. These regions correspond

²The term “most highly curved” means a region of the equilibrium shape crystal where H , the mean curvature, is maximum.

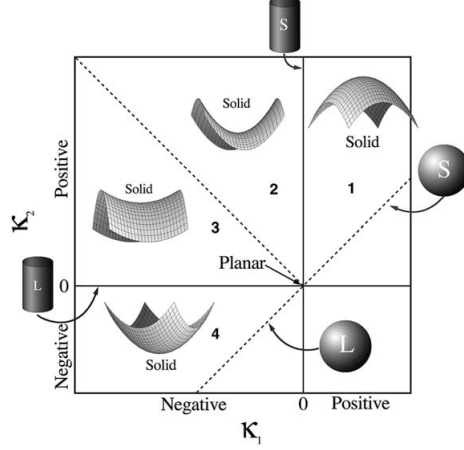


Figure 2.2: Map of the local interface shapes possible in an interfacial shape distribution [Men03].

to minima of the so-called solid-liquid interfacial “stiffness”. In simple cases, maxima of γ_{sl} indeed correspond to minima of the stiffness, but not always [Hax06b]. Additionally, the problem gets more complicated when the two principal radii of curvature are not maximized at a single location of the equilibrium shape crystal.

As the name indicates, the stiffness measures the variation of surface energy associated with a local deformation of a sphere. The lower the stiffness, the more easily the sphere can be made more convex at a given location. The definition of the interfacial stiffness originates from Herring’s relation [Her51] giving the variation of the chemical potential $\Delta\mu$ associated with the surface energy:

$$\frac{\Delta\mu}{V^m} = K_1 \left[\gamma_{sl}(\vec{n}) + \frac{\partial^2 \gamma_{sl}(\vec{n})}{\partial n_1^2} \right] + K_2 \left[\gamma_{sl}(\vec{n}) + \frac{\partial^2 \gamma_{sl}(\vec{n})}{\partial n_2^2} \right] \quad (2.25)$$

where V^m is the molar volume and the second derivative of γ_{sl} are taken along the corresponding principal directions of curvature (n_1, n_2) . Taking $K_1 = K_2$ for a sphere, the variations of chemical potential along the surface is directly proportional to Φ_{sl} , the generalized stiffness

$$\Phi_{sl}(\vec{n}) = \gamma_{sl}(\vec{n}) + \frac{1}{2} \left[\frac{\partial^2 \gamma_{sl}(\vec{n})}{\partial n_1^2} + \frac{\partial^2 \gamma_{sl}(\vec{n})}{\partial n_2^2} \right] \quad (2.26)$$

The first term in the definition determines the energy required to change the interface area, whereas the term in brackets determines the energy required for changes in local interfacial orientation.

Conversely, for an equilibrium crystal shape, the chemical potential is constant along the surface and the regions where the mean curvature is the highest are approximately given by the minima of the stiffness, but not exactly. Indeed, in 3 dimensions, the stiffness is actually not a scalar but a symmetric tensor [Du07]. It measures the variation of energy associated with curving a sphere along any arbitrary direction (this includes curving along one or two arbitrary axes). A more correct way to write Herring’s relation would thus be [Du07]

$$\frac{\Delta\mu}{V^m} = \underline{\underline{K}} : \underline{\underline{\Phi}}_{sl} = \begin{bmatrix} K_1 & 0 \\ 0 & K_2 \end{bmatrix} : \begin{bmatrix} \gamma_{sl}(\vec{n}) + \frac{\partial^2 \gamma_{sl}(\vec{n})}{\partial n_1^2} & \frac{\partial^2 \gamma_{sl}(\vec{n})}{\partial n_1 \partial n_2} \\ \frac{\partial^2 \gamma_{sl}(\vec{n})}{\partial n_2 \partial n_1} & \gamma_{sl}(\vec{n}) + \frac{\partial^2 \gamma_{sl}(\vec{n})}{\partial n_2^2} \end{bmatrix} \quad (2.27)$$

where $A : B = A_{ij}B_{ij}$. Again, this expression must be constant for an equilibrium crystal shape.

2.2 Measurement of the Interfacial Energy Anisotropy

The two most common experimental methods to indirectly measure the solid-liquid interfacial energy anisotropy of metallic alloys are the grain boundary groove [Gün85] (GBG) method and the equilibrium shape measurement [Bas69, Mil69a]. The former technique uses the equilibration of a grain boundary in a temperature gradient, and from the shape of the groove deduces the Gibbs-Thomson coefficient and the interfacial energy. In equilibrium shape measurements (ESM), one would ideally want to equilibrate a very small crystal seed in its melt. However since equilibration of solid particles in suspension in a melt is very difficult due to nucleation, sedimentation and convection issues, the inverse method is generally preferred, *i.e.*, measure liquid droplets trapped in a solid matrix. The principle advantage of this method over GBG is clearly that one experiment gives information about more than only one crystallographic direction. Therefore, we only focus on this second method.

2.2.1 Equilibrium Shape Measurements

The first trials to use a similar technique for solid-gas interfaces were done on faceted systems [Sun64] and only later on solid-liquid interfaces in hexagonal metals [Bas69, Mil69a, Pas82]. The real innovation which largely improved this technique was developed recently by Liu et al. [Liu01], the salient feature of which is that it avoids nucleation from a single solid phase in addition to the fact that the solid matrix is a single crystal which eases the orientation determination and avoids the formation of droplets at grain boundary. This is achieved through directional solidification of a specimen followed by a dual step heat treatment, the first one to homogenize the solute composition and the second to liquify the discontinuous eutectic phase into fine liquid droplets in equilibrium with the solid matrix. After quench, this leads to a controlled distribution of quenched liquid droplets, embedded in a single crystal matrix. As the matrix is a single crystal, it offers the advantage that only one experiment is necessary for the interfacial energy to be known in all crystallographic directions. The orientation of the single crystal can be determined by X-ray diffraction and the equilibrium shapes were up to now measured by serial sectioning.

Despite the progress, this technique is very delicate, especially when the anisotropy of γ_{sl} is low as in aluminum alloys. During heat treatment, great care has to be taken regarding the temperature stability, and thus phase fraction fluctuations, as well as thermal gradients. The latter must be very low in order to avoid displacement, and thus elongation, of the droplets due to diffusion of solute in the liquid droplets (the so-called “Thermal Gradient Zone Melting” (TGZM) effect [Til69]). Furthermore, serial sectioning is a tedious method where careful sample preparation is required.

Liu *et al.* were nevertheless able to measure quantitatively the anisotropy in weakly alloyed fcc aluminum alloys (Al-Cu [Liu01] and Al-Si [Nap02] and even to assess the influence of temperature [Nap04] (in Al-Sn). Their measurements are reported in Figure 2.3.

Results from 2004 could be plotted directly and measurements from 2001 and 2002 were adapted using (2.18).

2.2.2 Gradient Experiment

The droplet density in samples obtained using the above mentioned technique is relatively low when it comes to the different characterization methods used to analyze the equilibrium shapes. Thus the idea arose to combine Liu's method with a procedure providing finer and more numerous droplets before equilibration.

Recent work by Rettenmayr *et al.* [Fis11, Bös07, Ret06, Buc05] suggests that remelting a sample in a strong thermal gradient ($\sim 12\,000\text{ K/m}$) for a very short period of time ($\leq 1\text{ s}$) generates a small region (few mm) between the totally molten and the unaffected zone, with a fine dispersion of resolidified and unequilibrated droplets with sizes between 300 nm and 2 μm .

Such a fine distribution has the advantage of a much faster equilibration, but also bears the risk of a rapid evolution toward unwanted solution annealing if the temperature is kept too long in a single phase domain upon heating for example.

2.2.3 Molecular Dynamics

Another way to access the value of the interfacial energy and its anisotropy, is through molecular dynamics (MD) calculations, but as these methods are not used explicitly in this work, the reader is left with the original sources for the details of the different models and methods.

Since the pioneering work of Broughton and Gilmer [Bro86], atomistic simulations have been applied extensively to the calculation of γ_{sl} for a variety of systems [Hoy03, Hoy04, Lai05] using the embedded atom method (EAM). Yet, extracting the anisotropy parameters of the crystal-melt interfacial energy from the computation, with uncertainties of several percents, is impossible. Considering the importance of γ_{sl} anisotropy for the evolution of solidification microstructure and particularly for dendritic solidification, it was later suggested to circumvent this difficulty by computing the stiffness, which is much more anisotropic than γ_{sl} , for more accurate results. Most MD calculations thus use the known fact that the stiffness for a given orientation can be related to the spectrum of interfacial fluctuations in thermodynamic equilibrium [Fis82], the so-called capillary fluctuation method (CFM). These calculations established that the accurate parameterization of $\gamma_{sl}(\vec{n})$ for fcc metals requires not only the classical fourfold term of (2.14) but an expansion with a sixfold term such as (2.12). This was first demonstrated for Ni [Hoy01] and Al [Mor02]. The results from those two studies and other fcc metals and alloys are summarized in Figure 2.3. It shows that ε_1 is found positive and ranging between 2 and 11%, while ε_2 is negative and approximately one order of magnitude smaller. Remember however that, as seen in Section 2.1.3, the normalization factor of ε_2 is almost a factor 3 higher than ε_1 .

These anisotropy properties of fcc metals calculated by EAM, have been confirmed by a wide variety of model fcc systems, such as hard spheres [Dav06], repulsive power-law [Dav05], Lennard-Jones potential [Mor03, Dav03] and interface cleaving methods [Bro86, Dav03, Dav00] and seem thus to be independent of the calculation method. A recent review [Ast09] showed that all fcc systems modeled to date, with a wide variety of interaction potentials, have been found to yield positive values for ε_1 and negative (or statistically

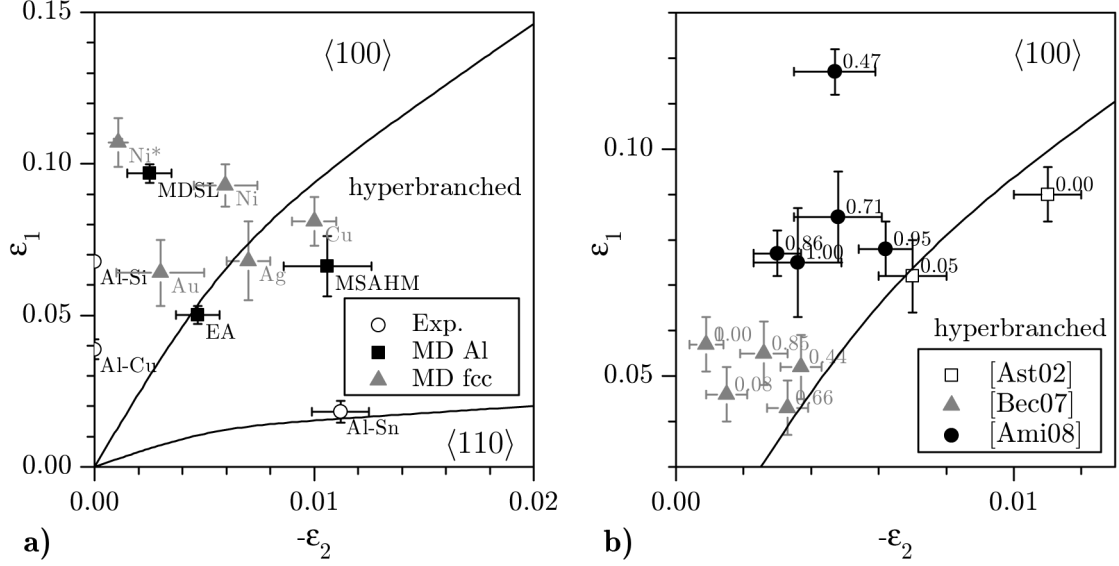


Figure 2.3: Values of the anisotropy parameters found in literature. Anisotropy parameters which were originally obtained with γ_{sl} formulations different from (2.12) were recalculated from the original stiffness data when available. If not, (2.18) was used. The solid lines indicate the limits between $\langle 100 \rangle$, hyperbranched and $\langle 110 \rangle$ dendrites as derived from solvability and phase-field simulations [Hax06b]. a) Experimental measurements for different Al alloys, Al-Sn [Nap04], Al-Cu and Al-Si [Nap02]. MD-CFM measurements [Mor02, Mor07] for pure Al with different potentials, EA [Erc94], MDSL [Mei92, Stu00] and MSAHM [Men05]. MD-CFM measurements for different fcc metals, Ag and Au [Hoy02], Cu [Hoy03], Ni [Hoy01], Ni* [Roz11]. b) MD calculations of the effect of composition in Ni-Cu with the label showing the atomic fraction of Cu in the solid.

insignificant) values of ϵ_2 . A conclusion of this review thus was that this fact suggests that this feature of fcc γ_{sl} anisotropy, and the inherent competition between $\langle 100 \rangle$ and $\langle 110 \rangle$ dendrite growth it implies, is an intrinsic feature dictated primarily by the symmetry of the crystal.

However, most simulations focused on pure materials and to date only few have examined alloys [Ast02, Bec07, Ami08]. Those three studies investigated the effect of the addition of lower melting point Cu to Ni. Asta *et al.* and Becker *et al.* used an EAM, whereas Amini and Laird used a hard sphere model. Becker *et al.* examined the effect on γ_{sl} of alloying two types of atoms of identical size, but differing energy scales, whilst Amini and Laird studied the effect of atoms with differing sizes but equal energy scales. Their conclusions all agreed that the addition of a lower melting point solute decreases the interfacial free energy. Given the difference in the models of Becker *et al.* and Amini *et al.* and their different findings on the effect of alloying on the anisotropy parameters (see Figure 2.3 b), the later speculates that size asymmetry affects ϵ_1 primarily, but energy asymmetry has more of an effect on the value of ϵ_2 .

As shown in Figure 2.3, the trends indicated by MD calculations show that alloying has an influence on the anisotropy, but there are still non-negligible discrepancies between the models for the exact prediction of anisotropy parameters, even for pure elements such as Al, Ni and Cu. Accurate experimental data are thus crucial for a better understanding and prediction of solidification phenomena. This is especially true for Al-Zn, since there is apparently no good potential to describe the zinc element forming hexagonal crystals.

2.3 Dendritic Growth

2.3.1 Fundamentals

Upon solidification, grains grow from seeds as nearly spherical or smooth globules up to a critical radius. Above this size, the solidification front destabilizes and forms dendrites [Mul63]. Papapetrou originally suggested the shape of the dendrite tips to be parabolic [Pap35], and slightly more than a decade later, Ivantsov [Iva47] found the exact solution of steady-state diffusion around a parabola in 2D and a paraboloid of revolution in 3D when capillary effects are entirely neglected and the interface is isothermal. Horvay and Cahn [Hor61] further generalized the analysis and Trivedi and Kurz [Tri94] provided a relation between the speed, v , the tip radius, R_{tip} , and the undercooling, ΔT , of a dendrite tip controlled by solute diffusion:

$$\Delta T = m_\ell c_0 (k_0 - 1) \frac{\text{Iv}(\text{Pe})}{1 + (k_0 - 1)\text{Iv}(\text{Pe})} + \frac{2\Gamma_{s\ell}}{R_{\text{tip}}} \quad (2.28)$$

with c_0 the nominal composition, m_ℓ the slope of the liquidus, k_0 the partition coefficient, $\text{Iv}(x) = xe^x \int_{-\infty}^x \frac{e^t}{t} dt$ the Ivantsov function, $\Gamma_{s\ell}$ the Gibbs-Thomson coefficient and $\text{Pe} = R_{\text{tip}}v/(2D_\ell)$ the solutal Péclet number. D_ℓ is the diffusion coefficient of the solute element in the liquid. Since (2.28) still has two unknowns (ΔT and R_{tip} if v is imposed), a selection criterion has to be added. Assuming that the dendrite tip grows at the marginal stability limit [Lan78], neglecting the capillary contribution in (2.28), this provides the relationship:

$$R_{\text{tip}}^2 \left(\frac{v}{D_\ell} \frac{m_\ell c_0 (k_0 - 1)}{1 + (k_0 - 1)\text{Iv}(\text{Pe})} - G \right) = \frac{\Gamma_{s\ell}}{\sigma^*} \quad (2.29)$$

where G is the thermal gradient in directional solidification and $\sigma^* = 1/(4\pi^2)$ is the dendrite tip selection constant. This model is known as the Ivantsov with marginal stability model. The expression (2.29) is however not very convenient to compute analytically and simpler forms of the LGK model are usually used. When considering free growth in the regime where $\text{Pe} \ll 1$, which also implies $\text{Iv}(\text{Pe}) \ll 1$, and G much smaller than the solute gradient ahead of the tip (first term in the parenthesis of (2.29)), the relation becomes

$$R_{\text{tip}} = \sqrt{\frac{D_\ell}{v} \frac{\Gamma_{s\ell}}{m_\ell c_0 (k_0 - 1) \sigma^*}} \quad (2.30)$$

To establish the relation with undercooling, an analytical expression for the Ivantsov function is needed and a simple and accurate candidate for $\text{Pe} \leq 0.1$ is [Dan09a]

$$\text{Iv}(\text{Pe}) \approx 1.5\text{Pe}^{0.8} \quad (2.31)$$

Finally, the relations between R_{tip} , v and ΔT are given by

$$R_{\text{tip}} = 0.83 \frac{\Gamma_{s\ell}}{\sigma^*} \left(\frac{(m_\ell (k_0 - 1) c_0)^{1/4}}{\Delta T^{5/4}} \right) \quad (2.32)$$

$$v = 1.45 \frac{\sigma^*}{\Gamma_{s\ell}} D_\ell \left(\frac{\Delta T^{5/2}}{(m_\ell (k_0 - 1) c_0)^{3/2}} \right) \quad (2.33)$$

Although the value of σ^* was shown to agree with numerous correlations on transparent alloys [Mus92], such model are missing an important parameter which is the solid-liquid

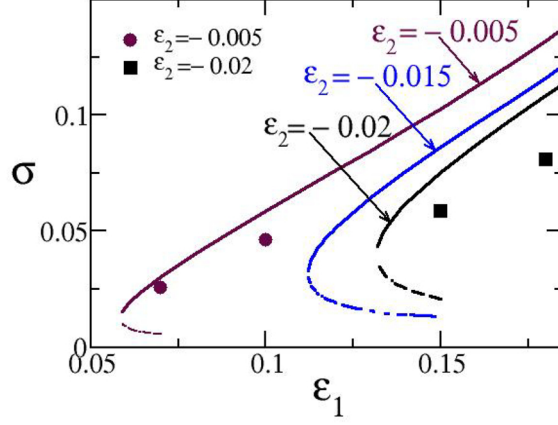


Figure 2.4: Dendrite tip selection parameter, designated by σ in the original source, as function of ε_1 and ε_2 for $\langle 100 \rangle$ dendrites calculated using solvability theory (solid and dashed lines) and phase-field simulations (symbols) [Hax06a]. Solid (dashed) lines correspond to stable (unstable) branches of steady-state dendrite growth solutions. These branches meet at a minimum value ε_1^* , which shifts further to the right with more negative ε_2 . The function $\varepsilon_1^*(\varepsilon_2)$ defines the lower limit of existence of $\langle 100 \rangle$ dendrite growth solutions which has been seen in Figure 2.3 and is in good agreement with the $\langle 100 \rangle$ -hyperbranched boundary determined by phase-field simulations which will be seen in Section 2.4.[Ast09]

interfacial energy anisotropy. Without it, seaweeds form instead of dendrites as shown by observations on organics [BJ86, Aka95] or by phase-field simulations [Pro03, Gra04].

The development of the solvability theory [Lan87, Kes88] led to the understanding that the stability parameter

$$\sigma^* = \frac{2D_\ell d_0}{R_{\text{tip}}^2 v} \quad (2.34)$$

which controls the operating state of the dendrite tip is uniquely determined by the anisotropy of $\gamma_{s\ell}$ at low velocities. Here d_0 is the chemical capillary length, defined as

$$d_0 = \frac{\Gamma_{s\ell}}{m_\ell c_\ell^0 (k_0 - 1)} \quad (2.35)$$

with c_ℓ^0 , the equilibrium interface concentration in the liquid side for a flat interface. When $\gamma_{s\ell}$ is described with the fourfold symmetry of (2.14), it has been shown that the stability parameter scales as $\sigma^* \propto \varepsilon_4^{7/4}$ [Bar89, BA93]. This predictive theory has meanwhile been validated by phase-field calculations [Kar97, Kar98, Pro99b], but only rarely by experiments [Liu06] because of the difficulty to obtain accurate anisotropy parameters measurements in metals.

Section 2.2 suggests that at least two anisotropy parameters are needed to characterize $\gamma_{s\ell}$ in fcc metals. This fact was for now only used once in conjunction with solvability. With this theory and phase-field calculations, Haxhimali [Hax06a] showed a high sensitivity of σ^* to ε_1 and ε_2 (see Figure 2.4). This again shows the importance of a precise determination of those parameters in metallic alloys.

2.3.2 Phase-field

Over the past fifteen years, phase-field has become the method of choice to model dendritic growth and provides a very powerful tool helping to understand microstructure development [Boe00, Ast09]. This is so because modeling this phenomenon basically consists in monitoring the evolution of the solid-liquid interface and the phase-field approach avoids the mathematical difficulty of applying boundary conditions at an interface whose location is part of the (unknown) solution. To this purpose, this method considers a diffuse interface of thickness δ over which a continuous variable ϕ , indicates the phase present at a given location on a fixed or adaptive grid [Boe02]. As ϕ is a continuous function, the modeled interface differs from the usual “sharp” interface ($\sim \text{nm}$ as predicted by MD). Several formulations have been proposed, with different values of the phase parameters in the homogeneous phases. This however makes no fundamental difference and $\phi = 1$ in solid and $\phi = 0$ in liquid will be considered here as this choice has been implemented in the phase-field code of the LSMX [Jac08].

The equation for the evolution of the phase-field is based on minimization of the free energy of the system [Whe92]

$$\mathcal{F} = \int_V \left[f(\phi, T, c) + \frac{\epsilon^2}{2} (\nabla \phi)^2 + \mathcal{H}g(\phi) \right] dV \quad (2.36)$$

It consists of three contributions. The first one is the integral over the volume of the free energy of the phases which is also the driving force for the interface motion. In areas where $\phi = 1$ or $\phi = 0$, f takes the value of the solid and liquid volumetric free energy and within the interface, f is interpolated over the solid fraction and classically takes the form [Boe02]:

$$f(\phi, T, c) = f_\ell(T, c) + p(\phi)[f_s(T, c) - f_\ell(T, c)] \quad (2.37)$$

$$p(\phi) = \phi^3(10 - 15\phi + 6\phi^2) \quad (2.38)$$

The second and third terms in (2.36) account for the interface contribution: $\frac{\epsilon^2}{2} (\nabla \phi)^2$ adds an energy penalty for the spatial variation of ϕ and has the tendency to keep the interface diffuse, while $\mathcal{H}g(\phi)$ introduces a penalty for ϕ being off its value for homogeneous phases, and keeps the interface from spreading over the whole volume. $g(\phi)$ takes the form of a double-well function with minima at $\phi = 0$ and $\phi = 1$

$$g(\phi) = \phi^2(1 - \phi)^2 \quad (2.39)$$

and \mathcal{H} is proportional to the height of this double-well.

The phase-field evolution equation for an isotropic system is given by the functional derivative of \mathcal{F} :

$$\frac{\partial \phi}{\partial t} = -M \frac{\delta \mathcal{F}}{\delta \phi} = M \left[\epsilon^2 \nabla^2 \phi - \mathcal{H}g'(\phi) - \frac{\partial f}{\partial \phi} \right] \quad (2.40)$$

where M is the mobility coefficient related to the interface kinetic coefficient. The composition, c and the diffusion coefficient $D(\phi)$, are interpolated between their values in the solid and the liquid phase:

$$c = \phi c_s + (1 - \phi) c_\ell = (1 - \phi + k_0 \phi) c_\ell \quad (2.41)$$

$$D(\phi) = D_s + \frac{1 - \phi}{1 - \phi + k_0 \phi} (D_\ell - D_s) \quad (2.42)$$

where c_s and c_ℓ are the concentration fields in the solid and liquid phases respectively. The composition in the solid and the liquid are simply linked by $c_s = k_0 c_\ell$ and the coupled diffusion equation for the solute is thus given by:

$$\frac{\partial c}{\partial t} = \nabla \cdot \left[D(\phi) \left(\nabla c + \frac{(1 - k_0)c}{1 - \phi + k_0 \phi} \nabla \phi \right) \right] \quad (2.43)$$

Since the diffusivity of heat is much larger than that of solute, the temperature field needs not be modeled at this small scale and it can thus be imposed according to external conditions of cooling rate and thermal gradient.

In the limit of the thin interface approximation, the steady-state solution for the interface shape in one dimension is [Kim99]

$$\phi_0(x) = \frac{1}{2} \left[1 - \tanh \left(\frac{\sqrt{\mathcal{H}}}{\epsilon \sqrt{2}} x \right) \right] \quad (2.44)$$

which gives the relation to the thickness of the interface

$$\delta = \frac{\epsilon}{\sqrt{2\mathcal{H}}} \quad (2.45)$$

The integration of the free energy over the interface leads to the following relation for the interfacial energy:

$$\gamma_{sl}^0 = \frac{\epsilon \sqrt{\mathcal{H}}}{3\sqrt{2}} \quad (2.46)$$

With this, the numerical parameters ϵ and \mathcal{H} can be related to physical variables [Boe02]:

$$\epsilon = \sqrt{6\gamma_{sl}^0 \delta} \quad (2.47)$$

$$\mathcal{H} = \frac{3\gamma_{sl}^0}{\delta} \quad (2.48)$$

When the interfacial energy anisotropy is included via the parameter, $\epsilon = \epsilon_0 \eta(\vec{n})$, (2.40) becomes

$$\frac{\partial \phi}{\partial t} = -M \frac{\delta F}{\delta \phi} = M \left[\nabla \cdot (\epsilon^2 \nabla \phi) + \nabla \cdot |\nabla \phi|^2 \epsilon \frac{\partial \epsilon}{\partial (\nabla \phi)} - \mathcal{H} g'(\phi) - \frac{\partial f}{\partial \phi} \right] \quad (2.49)$$

and $\eta(\vec{n})$ takes a similar form to the cubic harmonics expansions presented for $\gamma_{sl}(\vec{n})$ in (2.12) or (2.14). The mobility coefficient M is also anisotropic and takes the form of Equation (2.63) which will be introduced when comparing this model to the next. Equations (2.45) and (2.46) remain valid and the same anisotropy is introduced into the interface thickness and the interfacial energy [McF93]:

$$\delta(\vec{n}) = \frac{\epsilon_0 \eta(\vec{n})}{\sqrt{2\mathcal{H}}} \quad (2.50)$$

$$\gamma_{sl}(\vec{n}) = \frac{\epsilon_0 \sqrt{\mathcal{H}}}{3\sqrt{2}} \eta(\vec{n}) \quad (2.51)$$

Such a phase-field approach is however not suitable for quantitative analysis. Indeed, the artificial thick solid-liquid interface induces a chemical potential jump across the interface associated with so-called solute trapping, *i.e.*, atoms that cannot escape the advancing

solidification front fast enough to maintain equilibrium at the interface. Furthermore, this modifies the solute conservation condition at the interface. Karma [Kar01] proposed a solution that accounts for, and eliminates those effects by including an antitrapping solute current term, $\nabla \vec{j}$ in the formulation (left hand side of (2.43)).

This flux of solute \vec{j} must occur from the solid to the liquid and should thus be expressed in terms of the normal to the interface pointing towards the liquid

$$\vec{n} = \frac{-\nabla\phi}{|\nabla\phi|} \quad (2.52)$$

the sign appearing because of the values taken by the phase variable in the present model. Moreover, the flux must be proportional to the speed of the interface (critical stability value $v \approx D_\ell/\delta$, hence to $\partial\phi/\partial t$), to the interface thickness δ and to the local composition difference between solid and liquid. According to Jacot [Jac08], in this formulation this term therefore takes the form

$$\vec{j} = -\delta \frac{(1-k_0)}{1-\phi+k_0\phi} c \frac{\partial\phi}{\partial t} \frac{\nabla\phi}{|\nabla\phi|} \quad (2.53)$$

A 2D finite difference implementation of this model has already been used for the simulation of dendritic growth in hot-dipped galvanized coatings [Sem00, Nie06b] and was further adapted for 3D calculations on massively parallel clusters. Recent developments included an isotropic wetting angle as a boundary condition for the modeling of twinned dendrites [SO09a, SO09b] and anisotropic wetting for 3D simulations of hot-dipped galvanized coatings of zinc [Mar10a, Rap10].

The above presented formulation implemented at EPFL is directly linked to the physical properties of alloys. Since another, non-dimensional phase-field model [Pro05] was made available for this work, its formulation will be presented shortly. Although different, the following formulation [Ech04] has been shown to be equivalent to the one outlined above by Jacot [Jac08].

The phase parameter ψ is purposely chosen different than in the previous formulation, because here it takes the value $\psi = +1$ in the solid and $\psi = -1$ in the liquid. The two thus relate through

$$\phi = \frac{\psi + 1}{2} \quad (2.54)$$

The phase and concentration equations are given by:

$$\begin{aligned} [1 - (1 - k_0)\tilde{\Theta}] \eta^2(\vec{n}) \frac{\partial\psi}{\partial\tau} &= \nabla [\eta^2(\vec{n})\nabla\psi] + \nabla \left(|\nabla\psi|^2 \eta(\vec{n}) \frac{\partial\eta(\vec{n})}{\partial(\nabla\psi)} \right) \\ &\quad + \psi - \psi^3 - \lambda(1 - \psi^2)^2(\tilde{U} + \tilde{\Theta}) \end{aligned} \quad (2.55)$$

$$\left(\frac{1+k_0}{2} - \frac{1-k_0}{2}\psi \right) \frac{\partial\tilde{U}}{\partial\tau} = \nabla \left(\tilde{D}_\ell \frac{1-\psi}{2} \nabla\tilde{U} + \tilde{v} \right) + \frac{1}{2} [1 + (1 - k_0)\tilde{U}] \frac{\partial\psi}{\partial\tau} \quad (2.56)$$

This is a one-sided ($D_\ell \gg D_s = 0$) dimensionless formulation with a frozen temperature assumption. Space and time variables are normalized by W_0 , the interface thickness, and τ_0 the relaxation time respectively. Thus $\tau = t/\tau_0$. \tilde{U} is the local dimensionless supersaturation with respect to the reference point c_ℓ^0 , measured in units of the equilibrium concentration gap at that point,

$$\tilde{U} = \frac{1}{1-k_0} \left(\frac{c}{c_\ell^0} - 1 \right) \quad (2.57)$$

where, in isothermal solidification, $c_\ell^0 = (T_M - T_0)/m_\ell$ is the equilibrium concentration of the liquid at a temperature T_0 and T_M is the melting point of the pure substance. In directional solidification this concentration is defined as $c_\ell^0 = c_\infty/k_0$, where c_∞ is the composition far from the interface, generally the nominal concentration, and thus c_ℓ^0 is the concentration on the liquid side of a steady-state planar interface. \tilde{D}_ℓ is the dimensionless diffusion coefficient in the liquid defined as

$$\tilde{D}_\ell = \frac{D_\ell \tau_0}{W_0^2} = a_1 a_2 \frac{W_0}{d_0} \quad (2.58)$$

where $a_1 = 0.8839$ and $a_2 = 0.6267$, are numerical constants of the model. $\vec{\tau}$ is the antitrapping current

$$\vec{\tau} = \frac{1}{2\sqrt{2}} \left[1 + (1 - k_0)\tilde{U} \right] \frac{\partial \psi}{\partial \tau} \frac{\nabla \psi}{|\nabla \psi|} \quad (2.59)$$

Finally $\tilde{\Theta}$ is linked to the temperature imposed on the simulation domain. This model allows growth in a thermal gradient G and to follow the dendrite tip with a moving frame.

$$\tilde{\Theta} = \frac{\tilde{z} - \tilde{v}_P \tau}{\tilde{l}_T} \quad (2.60)$$

where $\tilde{z} = z/W_0$ is the dimensionless position along the z -axis (the imposed thermal gradient), $\tilde{v}_P = v_P \tau_0/W_0$ the dimensionless pulling velocity and $\tilde{l}_T = l_T/W_0$, the dimensionless thermal length defined as

$$l_T = \frac{m_\ell(k_0 - 1)c_\ell^0}{G} \quad (2.61)$$

The relation between the two formulations is thus finally given by the two following equations:

$$W_0 = \sqrt{2}\delta \quad (2.62)$$

$$M = \frac{D_\ell}{m_\ell \sqrt{2}\delta(k_0 - 1)a_1 a_2 \eta^2(\vec{n})c_\ell^z} \quad (2.63)$$

where $c_\ell^z = (T_z - T_m)/m_\ell$ is the equilibrium concentration at the temperature T_z .

2.4 Dendrite Orientation Transition

As stated in Section 2.1.6, in general textbooks of solidification [Cha64, Kur98], it is commonly taught that dendrites in cubic metals grow along $\langle 100 \rangle$ directions, since these directions correspond to maxima of $\gamma_{s\ell}$. This is indeed the case in many systems, *e.g.*, steel, Ni-base superalloys, Cu-base alloys, but aluminum alloys seem to behave differently. For example, this alloy system is the only one in which $\langle 110 \rangle$ twinned dendrites can form [Hen98a, Hen98b], although twinned dendrites have apparently been observed in Cu-Sn but at very large undercooling [Mul01]. Furthermore, when trying to reproduce twinned dendrites in laboratory-scale experiments, a whole variety of morphologies were seen in Al alloys [Hen98b]. Finally, in thin coatings of Al-Zn deposited by hot dipping on steel sheets, $\langle 320 \rangle$ growth directions were clearly identified [Sem01]. Given this wide variety of structures observed in aluminum, more studies have been carried out on

twinning [SO08, SO09c, SO09a] and coatings [Nie06a, Nie07]. The present work emphasize on the continuation of the research on Dendrite Orientation Transition (DOT) in aluminum-zinc alloys [Gon06, Gon08, Gon09].

A general survey of the literature shows that a change in the orientation of dendrites can be induced by different phenomena, namely flow of the melt, growth velocity and modification of the interfacial energy anisotropy via a change in alloying element concentration.

2.4.1 Flow Induced

Murakami *et al.* [Mur83, Mur84] showed that the solidification of Al-Cu alloys in flowing melt results in the formation of columnar dendrites deflected towards incoming flow. They showed that an increase in the solute content and/or growth rate favors the growth of dendrites along their preferred crystallographic directions rather than cells. The deflection becomes larger with increasing flow rate and decreasing copper content. This phenomenon can be accounted for in terms of the balance between the nature of dendrite to grow along the preferred ($\langle 100 \rangle$) crystallographic direction but also along the highest solutal (thermal) gradient which occurs along the upstream direction. It is important to recognize that even though the average solidification direction tilts upstream, the underlying crystal symmetry remains unchanged. This perturbed growth due to flow has later been studied using the phase-field method in 2D [Tön98, Bec99] and 3D [Jeo01], but will not be addressed more in detail since this is not the main subject.

2.4.2 Velocity Induced

Another well-known phenomenon is that dendrites can change their growth direction with their growth velocity in organic systems such as $\text{CBr}_4\text{-C}_2\text{Cl}_6$ and a succinonitrile alloy [Aka97, Des06] or in faceted systems such as $\text{NH}_4\text{Cl-H}_2\text{O}$ [Cha76]. However, the mechanism is unclear as the dendrite growth directions in these systems is influenced both by the anisotropy of the solid-liquid interfacial energy and by that of the attachment kinetics. In metallic alloys, the attachment kinetics does not play a significant role unless high growth rates (typically $> 0.1 \text{ m/s}$) are achieved. Therefore, the change of dendrite growth directions in Al alloys can only be attributed to the first contribution, *i.e.*, to a modification of the interfacial energy anisotropy by solute elements.

2.4.3 Solute Induced

As shown by the measurements in Section 2.2, aluminium has a very low interfacial energy anisotropy that could easily be perturbed by the addition of an alloying element with a different crystal structure, such as zinc, an hcp element, that exhibits an anisotropy of about 30% between the c-axis and the basal plane. A systematic effect of one alloying element has been identified by Gonzales *et al.* [Gon06, Gon08, Hax06b]. These authors have shown recently that an increase in the zinc content of Al-Zn alloys continuously changes the dendrite growth direction from $\langle 100 \rangle$ to $\langle 110 \rangle$ in a $\{100\}$ plane (see Figure 2.5).

Gonzales *et al.* observed that at nominal concentrations below 25 wt.% and above 55 wt.% Zn, dendrites are growing along $\langle 100 \rangle$ and $\langle 110 \rangle$ directions, respectively. It should be pointed out that a nominal composition of the liquid of 25 wt.% Zn (bottom scale) corresponds to only 10 wt.% in the solid phase (upper scale in Figure 2.5) if one

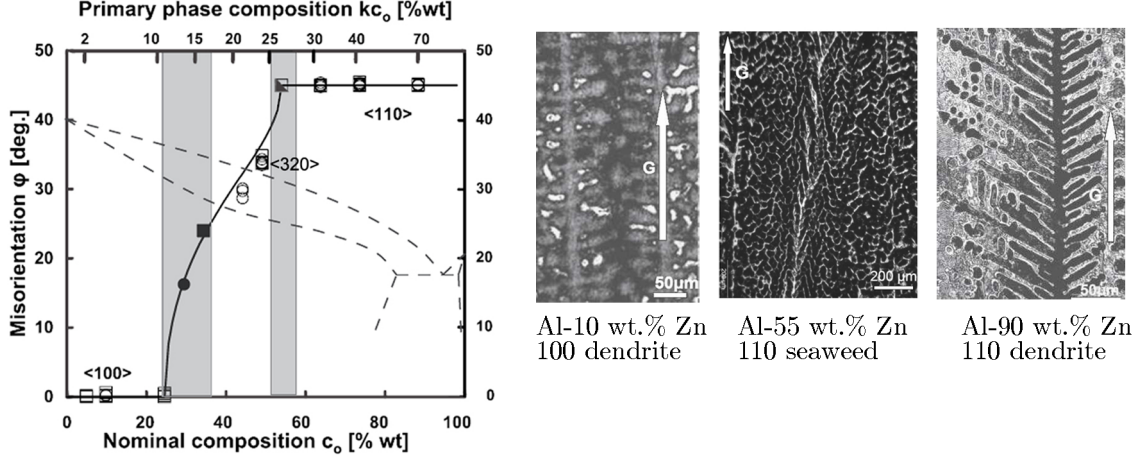


Figure 2.5: Angle between the $\langle 100 \rangle$ direction and the growth direction of Al-Zn dendrites as a function of the nominal concentration, c_0 , of Zn. The equilibrium concentration of the first solid, $k_0 c_0$, is also indicated on the upper scale. Open circles and squares correspond to Bridgman and directional solidification specimens, respectively. The two shaded areas near 25 and 55 wt.% correspond to concentrations for which textured seaweed structures were observed (filled circles and squares). The high temperature part of the Al-Zn phase diagram is superimposed in dashed lines. The micrographs to the left represent longitudinal sections obtained in Bridgman solidification (Al-10 wt.% and Al-90 wt.% Zn) and directional solidification (Al-55 wt.% Zn). [Gon06]

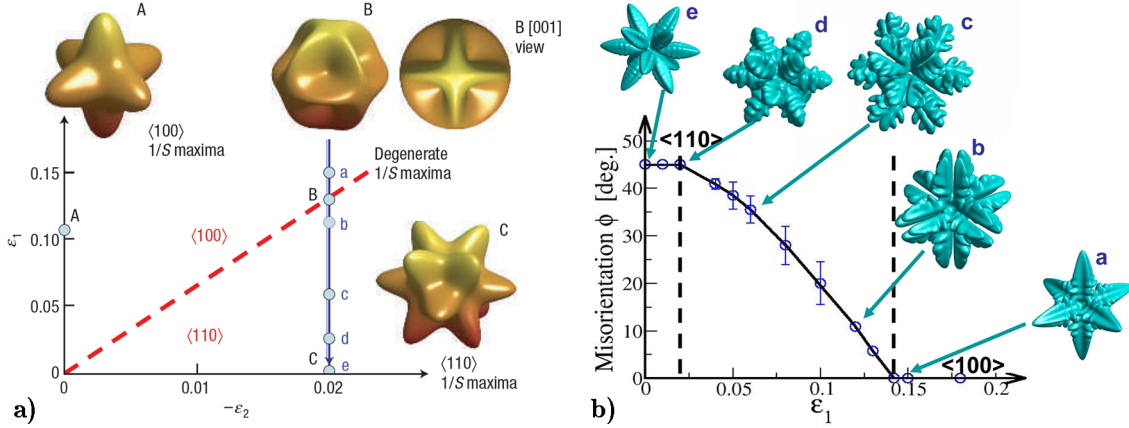


Figure 2.6: a) Orientation selection map from minimum interfacial stiffness. The trace of the interfacial stiffness, here called S , has minima that correspond to $\langle 100 \rangle$ and $\langle 110 \rangle$ above and below the dashed line ($\epsilon_1 = -20\epsilon_2/3$), respectively. There is a continuous degeneracy of orientation on this line where all directions contained in $\{100\}$ planes have equal stiffness minima. Illustrative spherical plots of $1/S$ are also shown for: A, $\langle 100 \rangle$ ($\epsilon_2 = 0$, $\epsilon_1 = 0.11$); B, degenerate minima ($\epsilon_2 = -0.02$, $\epsilon_1 = 0.13$); and C, $\langle 110 \rangle$ ($\epsilon_2 = -0.02$, $\epsilon_1 = 0$). The lower-case letters (a-e) correspond to the parameters of the phase-field simulations shown in b). b) Equiaxed dendrites and growth directions from phase-field simulations in pure undercooled melt. The phase-field simulations show the different equiaxed growth morphologies obtained for different values of ϵ_1 at fixed $\epsilon_2 = -0.02$, following the arrow (a-e) that crosses the degenerate $\langle 100 \rangle$ - $\langle 110 \rangle$ boundary. Instead of making an abrupt change from $\langle 100 \rangle$ to $\langle 110 \rangle$ as this boundary is crossed, the misorientation ϕ increases continuously from $\phi = 0$ ($\langle 100 \rangle$ dendrites) to 45° ($\langle 110 \rangle$ dendrites) over a large range of ϵ_1 between the two dashed lines. [Hax06b]

neglects the small solutal undercooling, *i.e.*, if the initial solid (or dendrite tip) is assumed to form at $k_0 c_0$. Switching to atomic percent, it appears that only 5 at.% of zinc in solid solution in fcc aluminium can induce this DOT. Between 25 and 55 wt.% , Gonzales *et al.* observed seaweeds at the beginning and end of the DOT (areas shaded in grey in Figure 2.5) and $\langle 320 \rangle$ dendrites around 50 wt.% Zn. The seaweed microstructure did not exhibit clear trunks and arms but was nevertheless textured, their main texture direction being shown with filled symbols in Figure 2.5.

The influence of $\langle hk0 \rangle$ dendrite growth directions on the evolution of the grain structures in DS specimens was investigated [Gon08] and it was found that similar mechanisms of grain selection outlined by Chalmers[Cha64] for $\langle 100 \rangle$ growth directions operate for $\langle hk0 \rangle$ dendrites and seaweeds in Al-Zn. However, the selection was found less severe for seaweed, since in those alloys many grains were still misoriented with respect to the thermal gradient after a long selection length. Besides a slower grain selection, the grain morphology in the seaweed specimens, after some selection has occurred, is more elongated. The elongation direction corresponds to the trace of $\{001\}$ planes and SEM observations revealed that this is due to the fact that seaweed microstructures make multiple branching in this plane and much less in the perpendicular direction.

The main feature that was lacking at the time of Gonzales *et al.* study in order to make more precise statements about the obtained structure, was the ability to analyze them in 3D. The very few that could be described in the Section 2.4.4 at the end of this chapter.

Extremum stiffness criterion

Dendrite growth directions have traditionally been assumed to correspond to maxima of γ_{sl} . In the simplest two-dimensional situation, these maxima also correspond to minima of the interface stiffness. This assumption was physically motivated by the fact that capillary forces are least effective at smoothing out protrusions of the solid-liquid interface in directions where the stiffness is minimum. As seen in Section 2.1.6, in 3D the minima of the generalized stiffness do not necessarily correspond to the maxima of the γ -plot. Furthermore, the interface stiffness becomes a tensor quantity and the trace of this tensor was proposed to formulate an extremum criterion for dendrite growth directions [Hax06b, Hax06a, Ast09]. An analytical calculation with (2.12) for the expression of the anisotropy reveals that minima of the stiffness trace (maxima of $1/S$ in Figure 2.6 a)) correspond either to $\langle 100 \rangle$ directions or $\langle 110 \rangle$ directions. These two regions of anisotropy parameters space are separated by a boundary ($\varepsilon_1 = -20\varepsilon_2/3$) where the stiffness trace is minimum for all directions contained in the $\{100\}$ planes. This situation has generally been called degenerate. Therefore, using this minimum stiffness criterion, one would conclude that dendrites select either $\langle 100 \rangle$ or $\langle 110 \rangle$ directions and, exactly on the boundary some unspecified directions contained in the $\{100\}$ plane.

In parallel to the experimental results by Gonzales *et al.*, another group did phase-field simulations of dendrite growth in a pure undercooled melt using the anisotropy form defined by (2.12) [Hax06b]. Their results reveal $\langle 100 \rangle$ and $\langle 110 \rangle$ dendrite growth near the positive ε_1 and negative ε_2 axis, respectively, as expected from the minimum stiffness criterion. However, this criterion does not predict the large region between the $\langle 100 \rangle$ and $\langle 110 \rangle$ regions (see Figure 2.3) where the dendrite growth directions vary continuously from $\langle 100 \rangle$ to $\langle 110 \rangle$, as illustrated in Figure 2.6 b). These so-called hyperbranched structures occupy a large region of the anisotropy parameter space, while the $\langle 110 \rangle$ dendrites

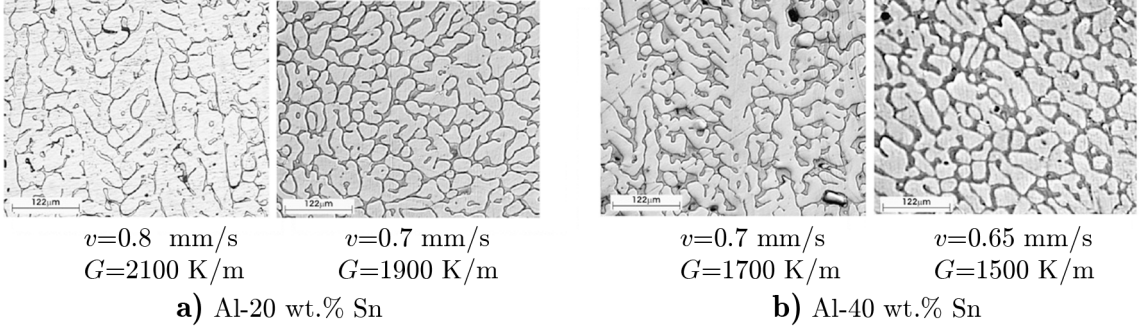


Figure 2.7: Longitudinal (left) and transversal (right) micrographs of directionally solidified Al-Sn alloys [Cru08]. In the longitudinal section the thermal gradient is pointing towards the top.

are constrained to a narrow region above the negative ε_2 axis. The similarity of those observations with the continuous change of dendrite misorientation found by Gonzales *et al.*, shows that the growth directions of dendrites are an indirect and amplified effect of the interfacial energy anisotropy, but that this minimum stiffness criterion cannot fully explain this intermediate and complex situation encountered here. Therefore, a generally valid theory predicting dendrite growth directions in three dimensions for complex expressions of γ_{sl} is still lacking and a direct measurement of the anisotropy parameter in Al-Zn seems essential to understand the phenomenon.

With the values of anisotropy found for Al-Sn by Napolitano *et al.* [Nap04], a stiffness minimum criterion suggests that dendrites should grow along $\langle 110 \rangle$ or according to Figure 2.3 at least be hyperbranched. But according to their X-ray diffraction findings, the selected orientation was $\langle 100 \rangle$. This effect was attributed to kinetics, but at a growth speed of 0.05 mm/s this seems unlikely. Recent work by Garica and co-workers [Oso06, Cru08, Cru09] on directional solidification of a wide variety of Al-Sn alloys, ranging from 10 to 40 wt.%, shows that the dendrites could very well be hyperbranched or even $\langle 110 \rangle$ (see Figure 2.7). Although difficult to interpret from simple metallographic transverse and longitudinal cuts, the secondary arms seem to deviate from $\langle 100 \rangle$. More details about the 3D structure and dendrite orientation in such alloys would be necessary. As mentioned by Napolitano *et al.*, this phenomenon could also be of solutal origin since for their droplets measured in Al-5 wt.% Sn, the liquidus composition corresponded to 93 wt.% or 99 wt.% Sn, depending on equilibration temperature. As the solubility of tin in the solid is null and the anisotropy of γ_{sl} should come from the solid, this could indicate that the difference between the droplet experiments ($v = 0$ and $c_\ell^* = 93$ wt.%) and the dendrite observations ($v \neq 0$ and $c_\ell^* \approx 5$ wt.%) is not due to a change of γ_{sl} .

Lastly, Rhême *et al.* [Rhe08] studied the effect in the hypereutectic part of the Al-Zn phase diagram and showed that the addition of Al to the primary hcp Zn phase did not influence the $\langle 10\bar{1}0 \rangle$ growth direction of zinc dendrites.

2.4.4 Seaweeds

The seaweed morphology has already been predicted in theory [Bre96] and modeled in 2D [Bre94, Emm99] but was until recently only observed experimentally in constrained 2D growth of transparent organic alloys [Aka95, Aka98]. In 2D, seaweeds commonly

appear, when the interfacial energy anisotropy is very low or null, but also when in constrained growth, the crystal is oriented in such a way that a crystallographic plane with a degeneracy of the stiffness is parallel to the 2D growth plane.

Observations of seaweed morphologies in 3D growth of metallic alloys are rare in literature. Mullis *et al.* [Mul04] observed them in ultra pure copper and Gonzales *et al.* [Gon06, Hax06b, Gon08] in Al-Zn alloys. The major difficulties in the interpretation of the analyzed microstructures and thus the lack for a general predicting criterion comes from the drawbacks of the analysis methods themselves. In fact, those very complex morphologies were, up to now, only analyzed in 2D and their random character was hard to overlook.

The only two examples where these complex 3D morphologies were also analysed with 3D methods are those of Assadi *et al.* [Ass09] and Gonzales [Gon09]. In both studies, optical serial sectioning was used to reconstruct the special microstructures. In $\text{Ni}_{51}\text{Al}_{49}$ solidified at very high velocity (2 m/s), Assadi *et al.* attributed the seaweed formation to kinetic effects in this intermetallic alloy. Gonzales observed Al-55 wt.% Zn textured seaweeds. Although this specimen exhibited a $\langle 110 \rangle$ texture, its 3D morphology clearly differed from a $\langle 110 \rangle$ dendrite where trunks and arms are visible. The seaweed structure was very tortuous and did not exhibit clear growth directions, yet it was textured. The reconstructed structures were analyzed in terms of the two principal curvatures, as described in Section 2.1.5, which clearly revealed the different nature of these two morphologies. In the dendritic specimen, curvatures were typical of the cylindrical geometry of dendrites trunks and arms. The seaweed corresponded more to a saddle-type geometry. These two morphologies exhibiting the same $\langle 110 \rangle$ texture, their associated growth mechanisms must thus clearly be different.

However, neither of those two studies quenched the growing structure and diffusion smeared the sharp solid-liquid interface, making the interpretation of growth directions or more subtle aspects of the microstructure very hard or impossible. Thus, those new microstructures and their 3D growth and orientation selection mechanisms are poorly understood and a study with adapted 3D methods is essential to shed light on this phenomenon.

Chapter 3

Experiments

The microstructural characterization of both equilibrium and growth morphologies is one of the main means to attain this work objectives. This chapter describes how the specific microstructures were produced and then studied. A Bridgman experiment was the key method for generating microstructures with control over the main solidification parameters, namely thermal gradient and growth velocity. This Bridgman setup was used in two distinct ways. First, as part of the quench experiment aiming at freezing structure during solidification, and second, to create precursor structures for the later droplet experiments. In the third section, the emphasis is thus put on how the different techniques are combined to yield equilibrium shapes. The last part of this chapter will detail the various methodologies and techniques used to characterize the dendrite morphologies and droplets shapes.

3.1 Alloys

Like in previous studies[Gon06, Gon08, Gon09], this work primarily focuses on binary aluminum-zinc alloys, for the reasons already exposed in Chapter 1. Nine Al-Zn alloys of various compositions ranging from 5 to 90 wt.% Zn were prepared from 99.995 wt.% purity base metals. The alloys were cast in a brass mold ($25 \times 25 \times 250 \text{ mm}^3$) and then machined and turned to rods of 3.6 mm diameter. The chemical composition of each casting was verified by EDX as will be described in Section 3.4.2.

The same procedure was used for two aluminum-copper alloys, Al-4 and 15 wt.% Cu. Those alloys were chosen to serve as reference, since they are widely used and were already extensively studied in the literature, specifically in the context of X-ray tomography due to the excellent contrast they provide. This choice is also interesting as it combines a solute element with the same crystallography as Al (fcc), and not hexagonal like zinc, thus perturbing differently the interfacial energy anisotropy.

3.2 Bridgman Solidification

The principle of a Bridgman experiment is to solidify a sample by pulling it from a hot to a cold zone in a controlled thermal gradient. Clyne [Cly80a, Cly80b] has observed that for metals with high thermal diffusivity, the solidification interface velocity (v^*) could differ from the pulling velocity (v_P) by as much as 50% or more for many Bridgman designs presented in the literature. Even if the initial transient might be long, it is not

EXPERIMENTS

infinite and steady state should be recovered after a characteristic time D_ℓ/v^{*2} [Smi55]. Clyne investigated this off-steady state behaviour both experimentally and numerically and wrote guidelines to avoid this deviation and have a better control of the solidification parameters. These guidelines have been scaled to the present case and applied within the limitations of the experimental setup.

- As suggested by Flemings *et al.* [Mol67, Rin72] and proven by Clyne, the specimen should be positioned with a certain length of it already in the cooling device so that it is solid and the system left to reach thermal equilibrium. This shortens the initial transient and the behaviour is closer to the ideal steady state, the interface remaining stationary relative to the furnace. Likewise, higher pulling velocity contracts the initial transient.
- To approach the ideal Bridgman experiment with infinite sample length, specimens at least 200 mm in length should be used to ensure that v^* is less than 10% away from v_P . Again, higher pulling velocity reduces this discrepancy because the transport of heat by specimen motion tends to limit the spreading of the isotherms which is responsible for the velocity deviation (high axial Peclet number).
- Since the main heat exchange is radial, it can be increased by a reduction in the diameter of the specimen, which has no influence on the tendency of axial conduction to flatten gradients along the specimen, but accentuates the radial component by decreasing the thermal mass (small radial Peclet number).
- The final transient at the end of solidification should not be forgotten and if necessary the sample quenched before its start (~ 50 mm from the end).

The Bridgman solidification setup used here is a modified version of the two-zone vertical tubular furnace (350 mm in length and 30 mm in diameter) presented by Gonzales and Rappaz [Gon06] in their DOT analysis. Figure 3.1 (a) depicts a schematic of the setup. The modification consisted in a reduction in diameter of the cold-zone copper water-cooled tube from 10 mm to 7 mm (minimum practical value for the desired crucible size), allowing for a reduction of the specimen diameter and thus a more efficient quenching, but also as seen above a better steady state behaviour of the isotherms.

The alloy rods were inserted in quartz or alumina crucibles (4/6 mm inner/outer diameter and 800 mm length) and hung in the furnace with the bottom of the specimen already partly inserted in the cooler for centering reasons. The hot zone temperature was selected to be 50 °C above the liquidus temperature of the respective alloys (see Table 3.1). The nature of the crucible was dependent on that temperature. Indeed, above 690 °C, quartz had a tendency to break and alumina was used instead. The setup was then maintained to equilibrate for 30 min before pulling started. The magnitude of the thermal gradient, which is dependent on the alloy properties and the hot zone temperature, was characterized in its own set of experiments which will be detailed in the next section. The crucibles comprising the specimen were pulled through the furnace at four different velocities between 1 and 20 mm/min.

3.2.1 Thermal Gradient Characterization

Thermal gradients in this Bridgman setup were characterized by introducing two K-type thermocouples in the same sheath, with a vertical separation of 10 mm into the

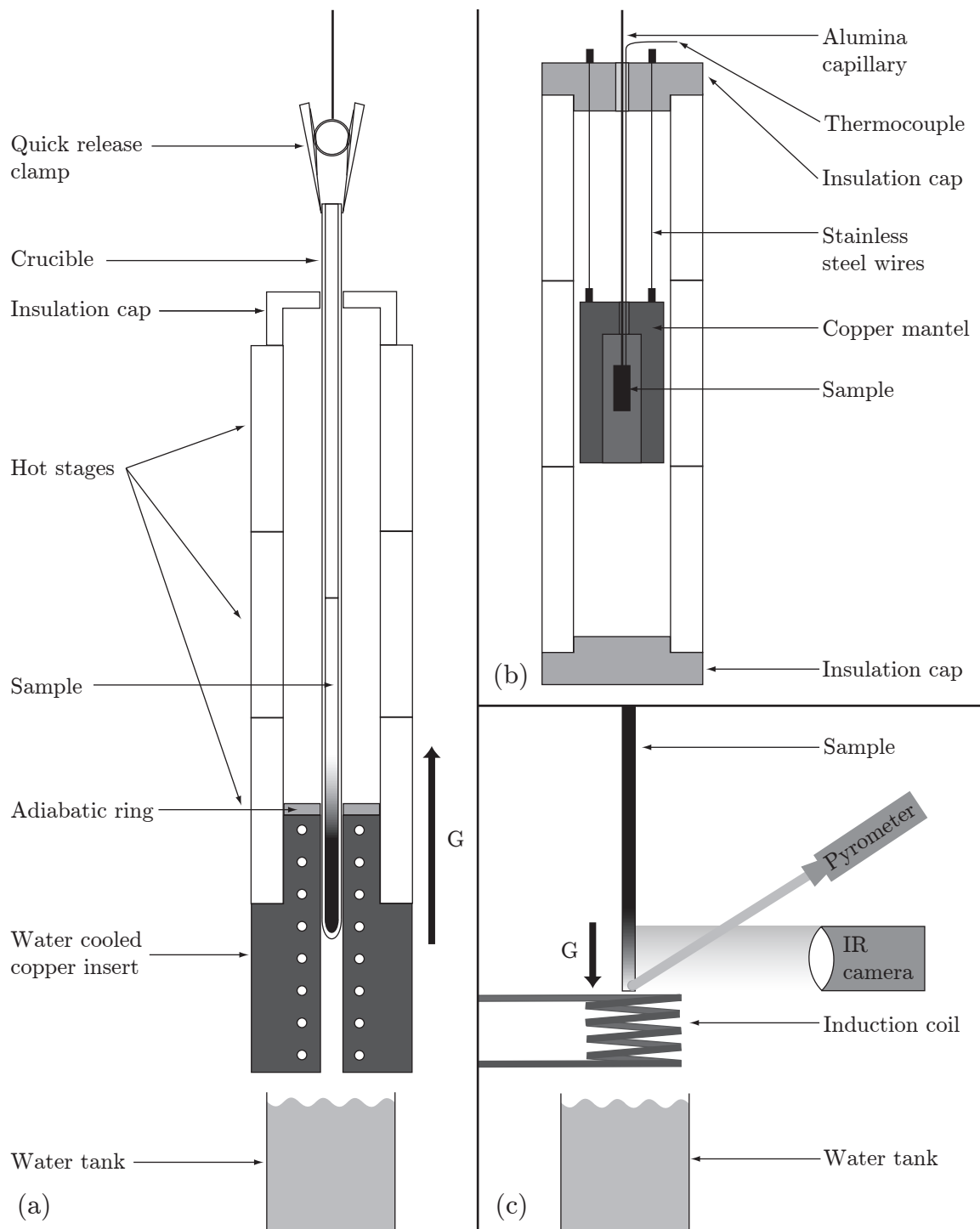


Figure 3.1: Schematic view of the different experimental setups. (a) Bridgman setup featuring independent control of three hot stages, which however were set at identical temperature, and a water-cooled copper insert, separated by a 7 mm thick ceramics ring serving as adiabatic zone. The quick release clamp allows for a rapid quench in the water container. (b) Isothermal annealing setup. (c) Gradient experiment setup with the control IR camera and pyrometer.

EXPERIMENTS

Table 3.1: Liquidus and solidus temperatures of Al-Zn and Al-Cu alloys obtained from the ThermoCalc database [Mey86, Din91].

Alloy [wt.%]	T_ℓ [°C]	T_s [°C]
Al-5Zn	652.3	641.0
Al-10Zn	643.8	621.3
Al-20Zn	626.0	581.7
Al-35Zn	597.4	521.5
Al-50Zn	566.2	469.0
Al-55Zn	555.0	457.5
Al-65Zn	531.0	439.5
Al-82Zn	474.5	388.0
Al-90Zn	427.0	381.0
Al-4Cu	646.3	579.5
Al-15Cu	608.7	548.2

melt. The general procedure for this set of experiment was exactly the same as for the quench experiments, except that one sample of each composition (Al-10, 20, 50 and 90 wt.% Zn) was used to test all pulling speeds. The sample were totally remelted and allowed to equilibrate for 30 min between each run. The acquisition of the temperature data was made through a NetDAQ Data Acquisition System. The absolute precision of the temperature measurement is on the order of 2°C, which is however of relative importance since a gradient has to be measured and not an absolute temperature. The relative precision is thus one order of magnitude better.

Figure 3.2 presents cooling curves for three different pulling velocities in Al-20 wt.% Zn. Values of the gradients were determined from the slope of the position-temperature curve in the solidification interval. Furthermore, following another guideline by Clyne, the lower thermocouple was situated 60 mm from the bottom of the specimen which should be far enough not to be influenced by the initial transient.

Table 3.2 summarizes the measured thermal gradient for the four tested alloys and four pulling velocities. Gradients across the interface were observed to depend on the pulling speed, although they were approximately constant within the regime of steady state growth, as shown in Figure 3.3. It might thus be argued that the experiment deviates from the ideal Bridgman conditions, but the trends being within the measurement errors, the deviation from the ideal scenario can be assessed to be negligible.

It can also be highlighted that the gradient in alumina crucibles is systematically larger than in quartz ones. Since alumina has a much higher thermal diffusivity ($1.2 \times 10^{-5} \text{ m}^2/\text{s}$) than quartz ($8.3 \times 10^{-7} \text{ m}^2/\text{s}$), the heat is extracted faster in the radial direction, *i.e.*, over a shorter distance, and thus the gradient in that case is higher.

A previous analysis [SO09a] of this furnace with bigger samples and crucibles (5/9 mm inner/outer diameter) showed that radial thermal gradient are on the order of 0.1 K/cm. The further decrease in sample diameter in the present case should thus make this contribution negligible. However it should be remembered that a very slight convexity of

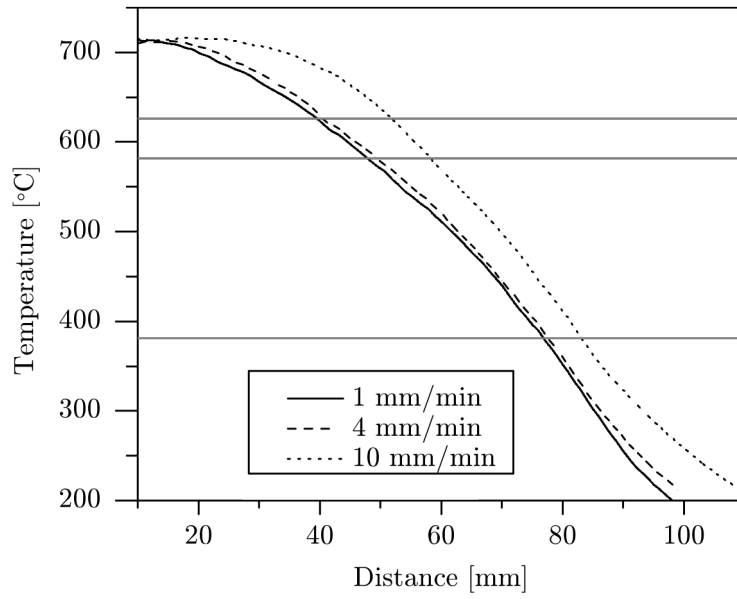


Figure 3.2: Al-20 wt.% Zn temperature profile during Bridgman solidification for three different pulling speeds. The horizontal lines represent from top to bottom the liquidus, solidus and eutectic temperatures.

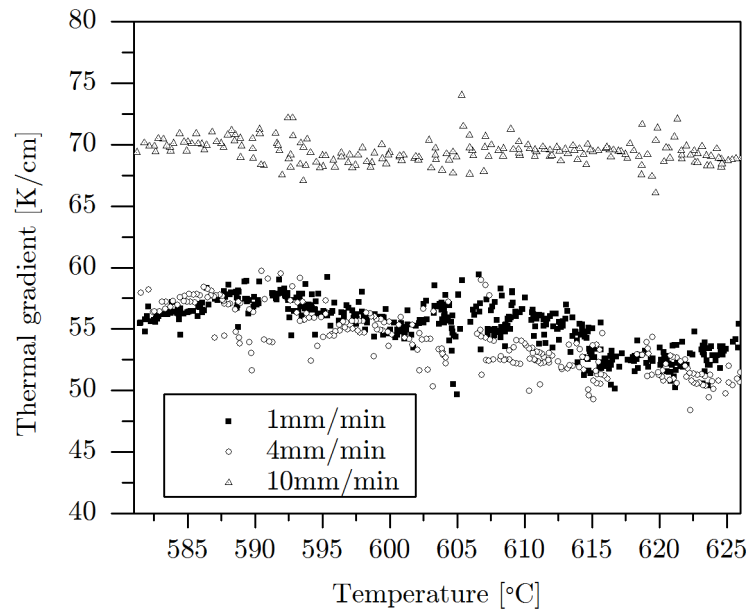


Figure 3.3: Thermal gradient measured from the liquidus to the solidus temperature in an Al-20 wt.% Zn alloy for three different pulling speeds.

Table 3.2: Thermal gradient for four different Al-Zn alloys at four different pulling velocities.

Alloy (wt.%)	Al-10Zn	Al-20Zn	Al-50Zn	Al-90Zn
Crucible	Al ₂ O ₃	SiO ₂	SiO ₂	SiO ₂
1 mm/min	97±4 K/cm	55±2 K/cm	54±5 K/cm	43±2 K/cm
4 mm/min	97±1 K/cm	54±2 K/cm	61±4 K/cm	55±3 K/cm
10 mm/min	96±3 K/cm	69±1 K/cm	70±4 K/cm	59±1 K/cm
20 mm/min	110±2 K/cm	-	-	77±2 K/cm

the isotherms can degenerate into a positive curvature of the solidification front due to macrosegregation of heavier solute elements [Dan09b]: positive segregation near the crucible wall and negative segregation near the center of the sample.

3.2.2 Quench

After a 100 mm travel towards the cold zone, the samples were quickly released and dropped (<1 s) in a water quench container below the furnace, allowing to freeze the growing structure and thus providing the whole solidification history in spatial form. Gonzales and Rappaz [Gon06] showed that the pulling velocity, in the range of their Bridgman and directional solidification experiments (*i.e.* 0.06–3 mm/s), did not influence the DOT. The four velocities in the present case were thus chosen to generate structures, fine enough to be representative in the sample volume and coarse enough to be easily distinguishable from the liquid after quenching. The range of cooling rate in the Bridgman furnace varied from -0.08 to -3 K/s, and thus the cooling rate of the quench (-400 to -600 K/s) offers a fair solid/liquid distinction even in the most unfavorable set of experimental conditions (high pulling velocity).

3.3 Droplet Experiment

3.3.1 Orientation Selection

In order to generate liquid droplets in a single crystal matrix by the techniques described by Napolitano *et al.* [Liu01, Nap02, Nap04], a precursor structure is needed. Through grain selection in columnar growth, the Bridgman experiment allows the development of a single grain structure or at least one with a low grain boundary density. This is required in addition to controlling the primary and secondary arm spacings, which dictate both the homogenization time to reach equilibrium and the final droplet spacing and size. The quality of the selection depending on the distance over which it proceeded, samples later used in the droplet experiments, were solidified until the end of the sample was reached (~ 200 mm travel) and only then quenched.

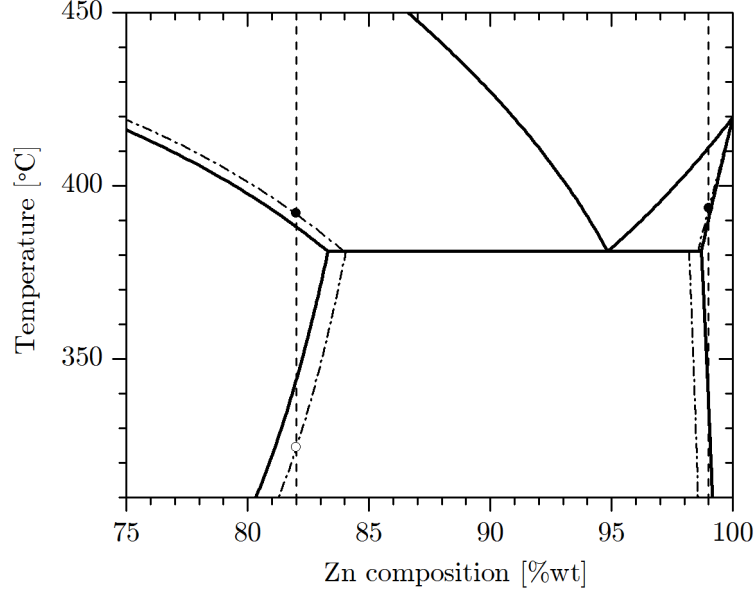


Figure 3.4: Partial view of the Al-Zn phase diagram showing the dual heat treatment steps. Solid state homogenization and equilibration temperatures are shown with open and filled symbols, respectively. The vertical lines represent the two nominal compositions used to produce equilibriums shapes. The dashed lines represent the iso-4% phase fraction lines.

3.3.2 Isothermal Annealing

The experimental setup for obtaining liquid droplets following the dual heat treatment presented in Section 2.2 was used for both Al-Zn and Zn-Al alloys (see Figure 3.4 for the composition). It was implemented in the same vertical tubular furnace as the one used for the Bridgman experiments. A hollow copper cylinder of inner/outer diameter 10/25 mm, was hung at mid height in the furnace by stainless steel wires. A 20 mm long samples cut from the “single-crystal” Bridgman rod was glued to a fine alumina capillary and hung at the center of the copper cylinder such as to avoid contact, which would lead to a hot spot or copper contamination. Figure 3.1 (b) shows details about this setup. The large thermal inertia of the copper mantel leads to very homogeneous heat treatment conditions (thermal gradient < 1 K/m and variation over time < 0.15 K), which is necessary to avoid TGZM (Section 2.2.1) and a fluctuation of the phase fraction. The furnace was then closed with ceramic caps and the temperature ramped for solid state homogenization. Another advantage of the copper cylinder is that it avoids overshooting the setpoint temperature. After the first holding time (up to 200 h), the temperature was then increased just above the solidus where 4 to 5% liquid fraction is expected (Figure 3.4). Finally after dwelling for a period of up to 400 h, the bottom cap was quickly remove and the capillary broken so that the specimen fell in a water quench tank just below.

In the case of Al-Zn, the highly saturated aluminum structure has a strong tendency to undergo a solid state decomposition upon cooling, making the determination of the matrix crystal orientation by electron backscattered diffraction (Section 3.4.3) difficult or even impossible at room temperature. Hence, an even more sever quench method was tried in some cases. Immediately after falling in the water, the sample was transferred to a liquid nitrogen (-196 °C) container, where it was kept until further processing. The samples were not mounted but clamped in a fitting and taken out of the nitrogen only for

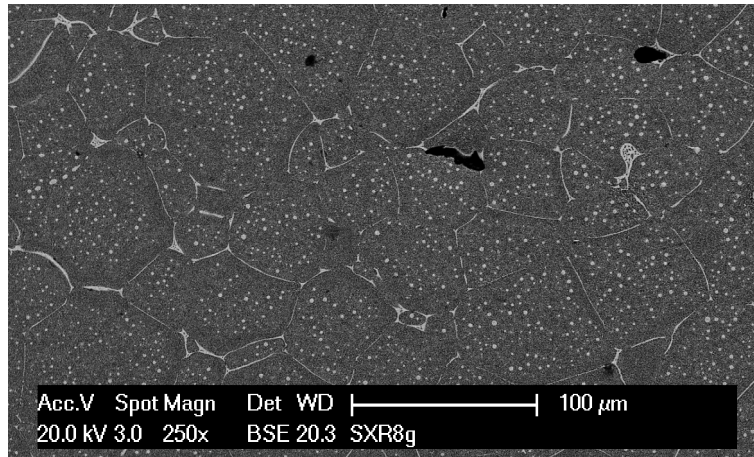


Figure 3.5: SEM micrograph of droplets before equilibration obtained by the gradient experiment for a coil power of 1 kW and 80 s.

the polishing and imaging. Even though the total dwell time at room temperature was kept below 30 min, the matrix still decomposed and orientation was no longer accessible.

3.3.3 Gradient Experiment

This section describes the procedure followed to produce very small and finely distributed droplets in Al-Zn by the alternative method presented in Section 2.2.2. Since former grain boundaries have a tendency to melt before the bulk, a structure with a very low grain boundary density is desired. To this end, a “single-crystal” Bridgman rod is again used as a precursor. It is to be noted that the alloy used for this experiment, Al-82 wt.% Zn, is very close to the solubility limit (83 wt.%) and thus the segregation during growth inevitably leads to a certain fraction of eutectic that self-quenches the dendrites below the eutectic temperature. A homogenization step is therefore performed in the single phase domain (360 °C for 60 hours) just below the eutectic temperature to avoid premature melting. Coarsening and coalescence decrease the grain boundaries density and dissolve the eutectic originating from the Bridgman solidification.

The gradient experiment installed in the Department of Metallic Materials of Prof. Rettenmayr at Friedrich Schiller University in Jena is shown in Figure 3.1 (c). The homogenized rod is mounted vertically with its bottom just above the last and topmost winding of an induction coil. The ideal excitation frequency is determined automatically by the coil controller during a frequency scanning. For this setup and alloy, it was determined as being 341 Hz. The induction coil was then switched on at a given power. The temperature profile in the sample was measured by an infrared camera and backed up by a pyrometer. As soon as the melting temperature was reached at the lowest, and thus hottest, spot on the rod, the power was switched off and the sample quenched in water. The power and accordingly the heating time were varied between 2 and 1 kW (during 15 and 80 s, respectively) to obtain the ideal microstructure with the longest zone presenting droplets without wetted grain boundaries. As Figure 3.5 shows, lower power and long heating time produced the best results.

Thus after identifying the region of interest, a transverse wire-cut yielded a disk-like sample (4 mm in diameter and thickness 1-2 mm) free or almost exempt of wetted

Table 3.3: Chemical etchant used for metallographic preparations [Pet01].

Alloy	Al-5 to 35 wt.% Zn	Al-50 to 90 wt.% Zn	Al-4 to 15 wt.% Cu
Solution	Tucker 50% diluted 1:4 with water	1 mL HNO ₃ 100 mL ethanol	Keller
Immersion time	1-2 s	2-10 s	12 s

grain boundaries but presenting a high density of droplets. The ~ 0.1 g specimen was then deposited on a preheated 600 g copper block residing inside a horizontal tubular furnace at the equilibration temperature (392 °C) just above the solidus, which allowed for the very rapid heat up needed to avoid a long dwell time in a single phase domain and the associated dissolution of the very fine droplets. The disk was coated with boron nitrid spray/ceramics glue beforehand to avoid oxidation and contamination. The heat treatment lasted 2 hours before the sample was dropped in a water quench tank, freezing the equilibrium shapes.

3.4 Characterization

The characterization techniques presented hereafter can be separated into two main categories: 2- (2D) and 3-dimensional (3D) analysis methods. 2D techniques such as optical and electronic metallography were predominately used to have a quick view of the sample and to determine regions of interest for 3D methods. The latter were then employed to access the detailed structures and morphologies, which are of interest in the present work.

3.4.1 Sample Preparation

After solidification, the samples were cut in the desired configuration with a diamond blade saw. The resulting sections were polished, first ground with SiC papers of decreasingly fine particles (*i.e.*, increasing grades, 500, 1000 and 2400), followed by a mirror polish with diamond emulsions with particles from 6 to 1 μ m on soft clothes. The subsequent steps then depended on the considered analysis technique, more specifically:

Optical imaging: the polished surface was then etched to reveal the structure. Etchants used for the various alloys are summarized in Table 3.3.

Electron microscopy: the samples were polished with diamond emulsions down to 1/4 μ m, leading to an ideally flat surface for chemical analysis and backscattered electron imaging.

EBSD: the surfaces were electrochemically etched to remove the thin deformed surface layer and give a good diffraction contrast for the backscattered electrons [Kat01]. An A2-Struers solution containing 72 ml of ethanol, 20 ml of 2-butoxyethanol and 8 ml of HClO₄ was used in a procedure of 4-10 s of polishing at 4 V and 2 s etching at 25 V. The polishing times were decreased with increasing zinc concentration.

3.4.2 Microscopy

Optical imaging was carried out on a Leica microscope connected to a 2080×1544 pixel camera. Composite image of samples larger than the field of view were created by a merge of overlapping single micrographs with the Panorama function of the software package Adobe Photoshop CS4TM.

All electron microscopy measurements were carried out at the Interdisciplinary Center for Electron Microscopy (CIME) of EPFL. A Philips FEI XLF30-FEG scanning electron microscope was employed for the imaging and chemical analyses. It was mainly used in Backscattered Electron (BSE) mode, which measures higher energy electrons after their scattering event within an interaction volume of 0.01 to 2 μm depth in the material. The resulting contrast is chemical and the gray scale intensity distribution is a function of the atomic number Z of the analyzed elements. The system also features an EDAX Si(Li) EDS (Energy-dispersive X-ray spectroscopy) detector, which was used to quantify the chemical composition of the samples with a typical spatial resolution of 1 μm and a precision of about 2%.

3.4.3 Electron Backscattered Diffraction

When dealing with the growth direction of complex morphologies, the determination of the crystal orientation is a crucial element. This information is gained by means of Electron Backscattered Diffraction (EBSD). This technique is based on the elastic interaction of BSE electrons with the crystallographic planes in the sample. Upon exiting the specimen, BSE electrons satisfying Bragg's law form cones that intersect a phosphor screen. The backscattering intensity, and thus the signal to noise ratio, is maximized by imposing a 70° tilt to the sample which is located 12-17 mm from the detector. The pattern formed by the diffracted beam consists of nearly parallel lines, called pseudo-Kikuchi lines [Ran00], corresponding to specific crystallographic planes which intersect on zone axes. A comparison of this pattern to a database then automatically identifies the crystal and its orientation. By scanning the surface of the specimen, a map of Euler angle triplets and phase associated with each pixel can be constructed.

The EBSD measurement were performed using a Philips XLF30-FEG SEM microscope equipped with a NordlysS II EBSD detector. The HKL Channel 5 software was used for the acquisition and treatment of orientation maps of the aluminum primary phase. Typical parameters for those mappings were an acceleration voltage of 20 to 25 kV, a working distance of 13 to 17 mm and a map step size of 2 to 4 μm . Due to the criticality of this measurement for the correct assessment of growth directions, a reference silicon wafer of known orientation was glued next to each specimen to serve as calibration. The precision of the system was estimated to be $\pm 2^\circ$ on the orientation measurement.

3.4.4 Serial Sectioning

First trials to access the three dimensional structures of the solidified samples were completed by means of a serial sectioning setup [Alk01], through a collaboration with Prof. Voorhees' research group at Northwestern University in Chicago. The combination of a micromiller and an optical microscope allowed for an automatic acquisition of regularly spaced micrographs. Sections of 1 to 20 μm thickness can be acquired at a rate of 20 frames per hour. A microtome diamond blade removes material and simultaneously polishes the surface, which is then etched and finally imaged before the cycle is repeated.

Despite its large field of view, its easy access and relative simplicity, several limits of this setup and advantages provided by other techniques decided us to not consider it further. First, the frame supporting the apparatus being also made of aluminum the choice of etchant was limited and did not allow to reveal the phases well without damaging the setup. Second, the imaging being optical, the resolution is limited to 1 μm , which in the case of equilibrium shapes or fine dendrites is too coarse. Moreover, the difference in lateral and vertical resolution led to voxel aspect ratios far too important for any smoothing of the shape to be efficient. Finally, the contrast in the images being only fair, segmentation was a tedious manual task.

3.4.5 X-ray Tomography

Considering the high degree of automation, excellent contrast and easy access provided by several research proposals, X-ray tomography was the method of choice for most 3D analyses of dendrites and seaweeds. The absorption variant of this technique relies on two basic principles, the Lambert-Beer law and the Radon transform [Kak87]. The Lambert-Beer law relates the absorption of light, in this case X-ray, to the properties of the materials it traveled through. The Radon transform is the mathematical formulation of a projection (the integral of a function over straight lines, here the integral of the absorption coefficient along the optical path), and its inverse transform establishes the possibility to reconstruct an object from all its projections [Rad17, Rad21]. The combination of these two principles allows to reconstruct the spatial distribution of the absorption coefficient μ within an object, from projections recorded at different angular positions. Since different phases and materials have different absorption coefficients, the 3D microstructure in a sample can be retrieved non-destructively. With synchrotron-based radiation, high throughput, excellent contrast and a resolution on the order of 1 μm or even below can be achieved even for metallic specimens.

The facility used in this work (proposals ID 20080240, 20080846, 20090118 and 20090795) is the TOMCAT (TOMographic Microscopy and Coherent rAdiology experimenTs) beamline at the Swiss Light Source (SLS) of the Paul-Scherrer Institut (Villigen, Switzerland). This high-throughput synchrotron-based tomographic microscopy beamline offers an energy range from 8 to 45 keV with a voxel size from 0.37 to 7.4 μm . More extensive technical details about the beamline have been published in several papers by Stampanoni *et al.* [Sta06, Mok10, Hin10, Mad11] and the following paragraph will only focus on the parameters relevant to this work.

After passing through a cylindrical sample, the transmitted X-rays hit a 25 μm thick LuAG:Ce scintillator which converts them to visible light recorded by a 2048 \times 2048 CCD camera via interchangeable (4 \times , 10 \times or 20 \times) objectives. The sample-scintillator distance is kept to a safe minimum (\sim 5 mm) to prevent deviation from absorption mode. The sample is rotated 180° on a stage at a constant angular velocity while typically 1000 to 1500 projections are acquired. An absorption contrast tomographic scan thus takes between 2 and 20 min. When a sample higher than the field of view needs to be scanned, the task is subdivided into slightly overlapping blocks through the vertical movement of the stage after completion of the rotation scan.

Once acquired, the projections are used to generate the sinograms (Radon transform of one tomographic slice) utilized for alignment. The reconstruction process itself uses filtered back projection [Fel84] or the faster regridding technique [Dow99, Mar10b] generating a 4 to 13 GB dataset consisting of 1024 to 2048 8-bit Tiff slices, with a contrast

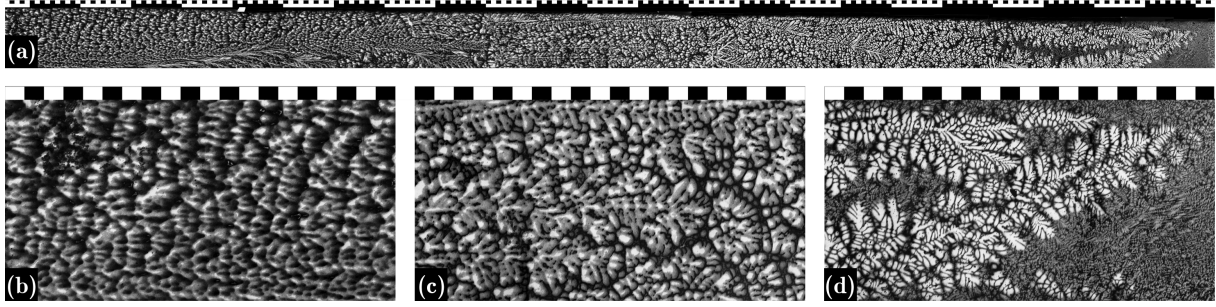


Figure 3.6: (a) Composite micrograph of the longitudinal section of a Al-50 wt.% Zn solidified at 4 mm/min. This 25 mm long section shows the effect of the quench and the evolution, smearing of the structure away from the tip, *i.e.*, the quenched interface. Thermal gradient is from left to right. Small and big divisions of the top scale represent 100 μm and 1 mm respectively. The primary solid phase is white and the quenched liquid dark gray. (b-d) Detail view of three regions of the sample, scale bar division represent 100 μm .

similar to those obtained in the BSE mode of SEM. Light elements appear darker than high Z number ones.

Sample Preparation and Acquisition

Since the analysis volume is still much smaller than the Bridgman sample dimension, a specific region has to be selected for the tomographic microscopy. For each specimen, a composite optical micrograph of a longitudinal cut (*e.g.* Figure 3.6) was used to precisely locate the tip of the quenched growth morphology. A stepped cylindrical column was then machined at that specific location. The bottom of the column was machined to 3 mm diameter to fit the mounting, the dimension of the region of interest was on the other hand dictated by tomographic constraints.

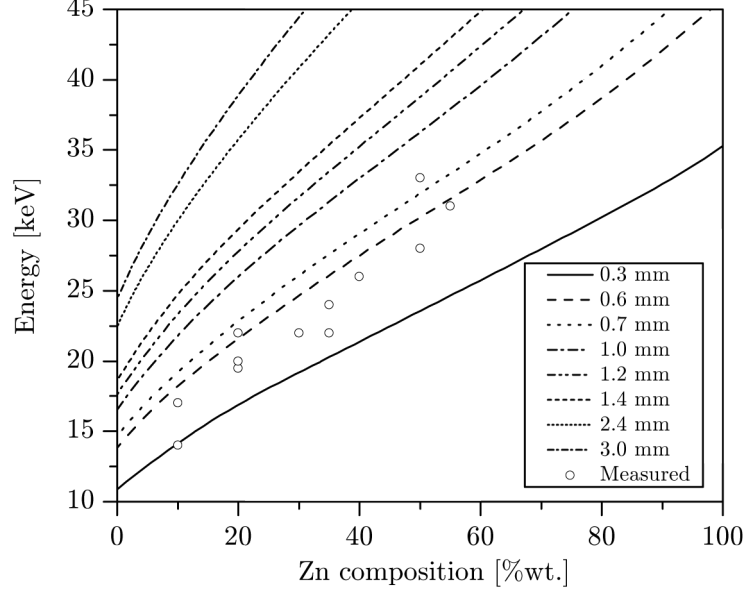
Two main considerations had to be taken into account in the selection of the sample diameter. First, for the specimen to be representative, its diameter should contain at least a few characteristic primary dendrite spacings (λ_1). Furthermore, for the fine morphological details to be resolved, the pixel size should be smaller than the secondary arm spacing λ_2 . It should be recalled that the resolution is at least twice the pixel size since two pixels are necessary to define an edge. These two reasons also imposed the choice for the Bridgman solidification conditions. Table 3.4 gives the field of view, *i.e.*, maximum sample diameter, and pixel sizes achievable with the beamline optics. The pixels on the CCD camera can be binned (combined two by two) leading to only half the pixel size in the final image, but a four times faster exposure (*i.e.*, throughput) for each projection since the signal to noise ratio is increased by the same factor.

Secondly, aluminum and zinc are very different X-ray absorbers, thus very different conditions had to be chosen in order to accommodate highly absorbent zinc-rich alloys as well as low alloyed samples. The X-ray penetration is dependent on their energy, the composition and thickness of the sample. Figure 3.7 summarizes these effects and gives the lowest limit for which 20% transmission is attained for different sample thicknesses as a function of the Zn composition. This transmission value is needed for good quality tomograms.

Although the apparatus limitation of 45 keV allows to scan 700 μm with up to 90 wt.% zinc, none of the sample with a composition superior to 35 wt.% was machined to a

Table 3.4: Field of view and pixel size for the different available objectives in the beamline configuration used for this work.

Objective	Field of view [μm]	Pixel size 2048×2048 [μm]	Bined pixel size [μm]
4×	3785	1.85	3.7
10×	1515	0.74	1.48
20×	757	0.37	0.74

**Figure 3.7:** X-ray energy required to have 20% transmission for different sample diameters and zinc composition, calculated by the Lambert-Beer law. The dots represent the measured energies for a serie of 600 μm column scans performed at the TOMCAT beamline.

diameter above 700 μm . Indeed, the optimum X-ray flux is around 20 keV. The higher and thus the further away from this value, the lower the flux and consequently the longer the exposure time. Excellent results were obtained with small samples at pulling speeds of 4 mm/min and above. As a direct consequence, above 50 wt.% Zn, there was no need in producing a sample at 1 mm/min since the structures were too coarse to be observed in a 700 μm column. As can also be seen in Appendix B, which provides a full list of samples and scan conditions, certain other combinations of composition and pulling velocity, which would have been redundant or of limited interest, were not analyzed.

Post-processing

Given the amount of samples scanned, a tremendous quantity of data was collected. A semi-automated procedure (a script using ImageMagick[®]) was developed to save disk space and ensure the ability to visualize the tomograms. Indeed, even a single-block sample of 13 GB is impossible to load into the RAM memory of the visualization station (max. 8 GB RAM). The post-processing strategy was to align multi-block tomograms, crop them to the minimum necessary and convert the Tiff files to the lossless compression PNG format. Up to 45% of disk space could be saved.

Although the full resolution is necessary for quantitative analysis of the data, it is not essential when it comes to identification of microstructural features. Hence, the datasets were duplicated and the resolution reduced by a factor of 2 to 4 until a slice did not measure more than 500×500 pixels. The third dimension was also reduced accordingly and stacks of multi-block tomograms merged. The shrunken tomograms thus never exceeded 1 GB, a size much easier to handle and process further.

Filtering and 2D visualization was performed with ImageJ, whereas the Avizo[®] software package was used for 3D visualizations. The dataset could then be searched for specific morphological features such as symmetry planes, which are clearly identifiable when sweeping through a sample from bottom to top or vice-versa.

Assessment of growth directions

The careful analysis of each microstructure allows the determination of particular planes or growth directions which should be associated with the corresponding crystallographic orientations. Therefore, after X-ray tomography, the reconstructed data stacks were searched for a location in the sample featuring widely developed secondary arms in a grain, reaching all the way up to the quenched solidification tip. A transverse cut was then realized with a diamond blade saw at that precise location in the column (dashed line on Figure 3.8 (c)) and the sample prepared for EBSD orientation mapping.

The SEM micrograph on which the EBSD orientation map is based (Figure 3.8 (a)) was used to retrieve the plane to which it corresponds best in the tomography dataset (Figure 3.8 (b)). As Figure 3.8 (c) shows very well, it is not always exactly perpendicular to the axis of the sample, but this deviation can be accounted for. The orientation map itself was then superimposed on the tomography section (Figure 3.8 (d)). To ensure the best possible alignment, the map, when possible, spans over the whole sample.

This superposition allows to calculate the relation (Euler angles) between the coordinate system of the tomography dataset $\langle xyz \rangle$ ¹ and the EBSD coordinate system. The misorientation, with respect to the EBSD coordinate system, of each grain and its $\langle hkl \rangle$ crystallographic directions of interest can thus be rotated from the coordinate system of the EBSD map to that of the tomography stack. All planes and directions identified in that stack by $\langle xyz \rangle$ directions can be associated with the $\langle hkl \rangle$ directions of the crystal (Figure 3.8 (e)).

It should be noted that all points on the pole figures are obtained in a statistical sense. The crystal orientation is taken as the average over all indexed points in a grain of the EBSD map. The dots representing trunks and secondary arms are an average over 3-5 and 10-20 elements, respectively. The dispersion of the measurements is smaller than the dot size used to represent them. Furthermore, the results show good repeatability between different experiments, *i.e.*, between different grains in one sample and between different samples produced under the same conditions.

3.4.6 Focused Ion Beam

Focused ion beam (FIB) is a relatively recent technique which, amongst other capabilities, enables the reconstruction of small 3D volumes with a nanometric resolution. In the present work, it was used to mill the specimen surface by Ga^+ ion bombardement and

¹with the thermal gradient \vec{G} along $\langle 00z \rangle$

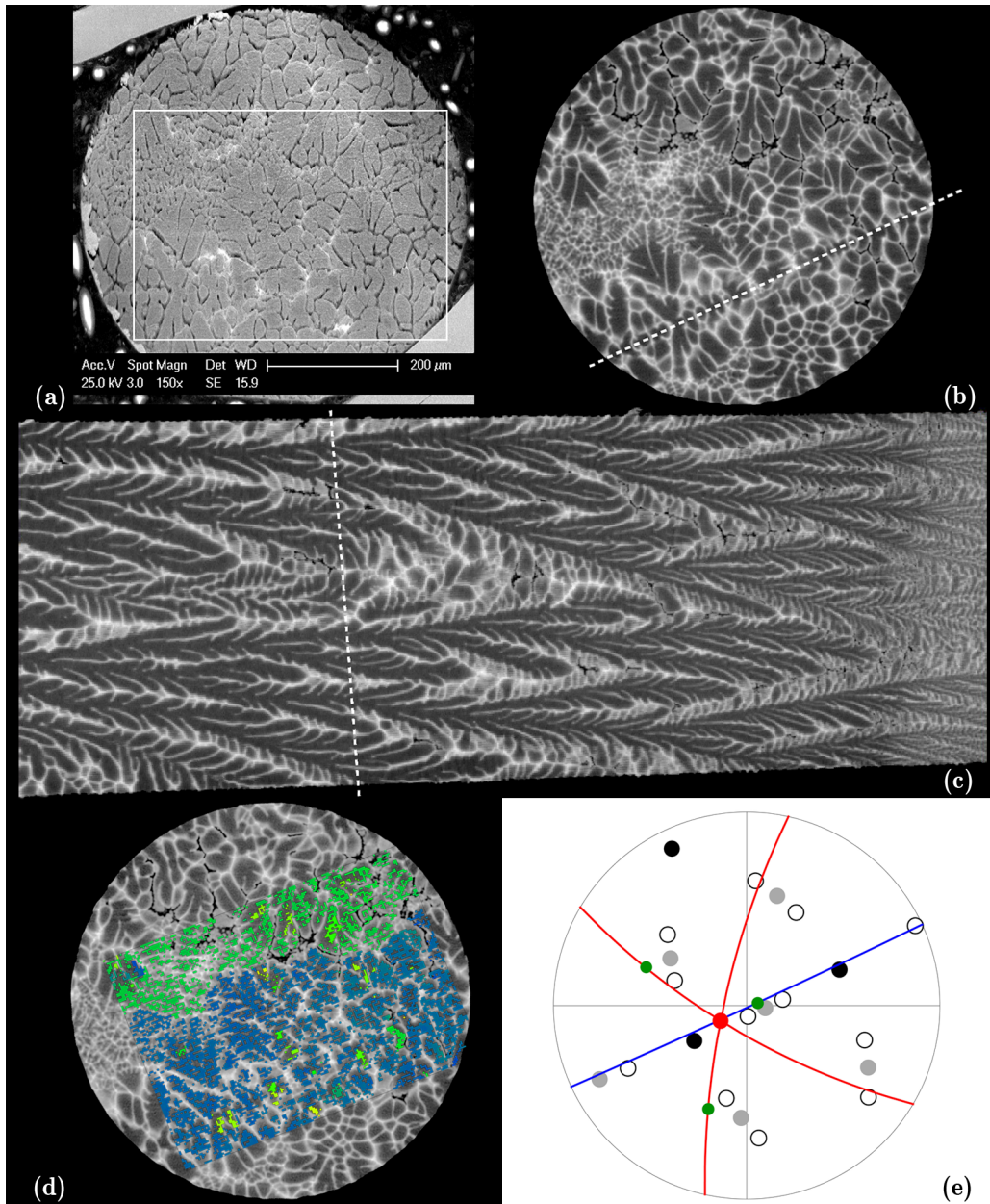


Figure 3.8: (a) SEM micrograph of the cut through a tomography sample, the white rectangle indicates the location of the EBSD map. Transverse (b) and longitudinal section (c) of a tomogram of the corresponding quenched Al-50 wt.% Zn sample solidified at 4 mm/min, showing the contrast between the different morphological features. The primary solid phase is dark gray, the thin zinc-rich segregation layer around it is white, the solidification pores are black and the quenched liquid is in light gray, actually a mixture of white and dark gray. In the longitudinal section, the thermal gradient is from left to right and the quenched interface can be seen to the right of the image. The dashed lines depict the location of the longitudinal and transverse sections respectively. (d) Same section as (b) with the superimposed EBSD orientation map showing two grains, in green and blue. More details about the EBSD map will be given in Figure 6.7. (e) Typical pole figure in the tomography stack coordinate system. The blue and red lines correspond to planes of interest in the tomography dataset. The red and green dots represent the directions of primary trunks and secondary arms respectively, measured in the 3D reconstruction. The crystallographic orientations obtained from the EBSD map for the corresponding grain are shown by black ($\langle 100 \rangle$), grey ($\langle 110 \rangle$) and open ($\langle 320 \rangle$) circles.

EXPERIMENTS

to serial section a $20 \times 20 \times 20 \mu\text{m}^3$ volume to obtain the morphology of an Al-82 wt.% Zn equilibrium shape droplets produced by the gradient experiment.

Anisotropy parameter fitting

Once the equilibrium shape was acquired, its mass center was determined and a mapping of the radius as function of angular position realized. The orientation of the surrounding crystal was then associated to the equilibrium shape. A method based on the ξ -vector formalism and the interfacial energy anisotropy development has been implemented to precisely calculate the ε_i parameters. This method is very similar to the one used to determine the mesh anisotropy for the phase field calculations (see Section 4.3.1). The theoretical expression for the radius of an equilibrium shape along specific crystallographic directions being measured, the ε_i can be directly calculated from the ratio between these radii. These equations will be treated in more details in Section 4.3.1.

Chapter 4

Phase-field modeling

The phase-field modeling in this work has been performed with two different codes based on the two equivalent formulations presented in Section 2.3.2. This chapter will detail these two codes and show the important aspects of modeling dendritic growth for low anisotropies and low undercooling. The mesh anisotropy plays a critical role in the predicting capability of such phase-field model and this aspect will be treated in particular for the simulation of equilibrium and growth structures.

4.1 Codes Description

4.1.1 Finite Difference Code

The phase-field model developed over the last years by J.-L. Desbiolles at LSMX is the 3D extension of the code commercially available in the Calcosoft®-PHF module. This code uses an explicit finite difference (FD) model designed to run on distributed memory, massively parallel machines. On the latter, the fixed orthogonal grid mesh is split into sub-domains of equal size, where the phase-field equations are solved in an Eulerian frame, on separate CPUs. In order to enable the spatial derivatives to be computed everywhere, the outer layer of nodes of a sub-domain is transmitted to the neighboring CPUs, where they are stored as phantom nodes. The exchanges between the processors are ensured through the Message Passing Interface (MPI) [Sni98].

The discretization of the Laplacian is a user available option in the code. A Laplacian using only the first neighbors is the default standard. Since grid anisotropy was of concern, a more isotropic Laplacian using the first, second and third neighbors was implemented [Pat06] and is the only one used hereafter. For all calculations with this code, the ratio between cell size Δx and interface thickness δ was fixed to 0.88^1 since this value showed good convergence and accurate description of the interface.

All calculations done with this code have been performed on the large CALLISTO cluster of EPFL. It is constituted of 128 blades, consisting each of two quad-core Intel Harpertown 3.0 GHz processors with 32 Gbytes memory each. Typically, 64 processors were used for 3D calculations of a $60 \times 60 \times 80 \mu\text{m}^3$ overall domain volume (3.6×10^7 cells). The corresponding mesh size was $0.2 \mu\text{m}$ and the time step that satisfies the Fourier condition for both the solute and the phase was 4×10^{-6} s. CPU time was about 5 hours ($\times 64$ processors) to solve 0.5 s of dendrite growth.

¹which corresponds to $\Delta x/W_0=0.625$ or to about 6 nodes across the diffuse solid-liquid interface which is about $4 W_0$

4.1.2 Finite Elements Code

Since in phase-field the length scales of the grid spacing ($\Delta x \approx W_0$ to describe the interface) and the simulation domain ($L_{x,y,z} \gg D_\ell/v$ to avoid interaction between the solute field and the boundaries) are widely different, a lot of efforts have been put in developing phase-field models with adaptive meshing [Pro98, Kim99, Pro99a, Jeo01, Jeo03, Bur04, Pro05, Ath06, Nar07]. Prof. Dantzig provided the source code [Ath06] to be used in this work. The model for dilute alloys is based on the one-sided (vanishing solid diffusivity) phase-field formulation by Echebarria *et al.* [Ech04] for directional solidification, with a fixed temperature approximation (*e.g.* imposed temperature or imposed thermal gradient). The phase-field equation is solved explicitly, whereas the solute equation is solved implicitly.

The equations are solved on an adaptive finite element mesh, using hexahedral elements, stored in an octree data structure. Local error estimators are used to refine or coarsen the mesh where needed, allowing the tracking of the interface as well as the resolution of gradients in the solute fields. Details about the mesh refinement techniques in 2D [Pro99a] and 3D [Jeo01] can be found in the original papers.

Considering that in directional solidification, initial transients can be very long before the interface reaches steady state, a Lagrangian frame (translating at the pulling speed usually equal to the growth speed) has been implemented to allow smaller simulation boxes for directional solidification.

Given the growth velocities concerned here, zero or very low interface kinetics assumption is desired. As shown by Echebarria *et al.* [Ech04], totally suppressing the kinetics is not possible due to the discontinuity in the concentration field at the interface in a one-sided model. But to make sure the kinetic coefficient is negligible at the interface, the phase-field relaxation time τ was made temperature dependent in this region (first term in (2.55) and (2.60)).

The model is also provided with fluid flow computation capabilities, though this feature was not used here.

Table 4.1 summarizes the differences between the two codes detailed above. One should recall that, as mentioned in Section 2.3.2, although the implementation and the formulation in the codes are different, they should lead to equivalent results, at least from a qualitative, if not fully quantitative, point of view.

Table 4.1: Summary of the comparison between the finite difference (FD) and finite elements (FE) codes for dilute alloy solidification.

Code	FD	FE
Grid	Regular	Adaptive
Processor	Parallel	Single
Frame	Eulerian	Eulerian and Lagrangian
Model type	Two-sided	One-sided
Physical parametrization	Dimensional	Non-dimensional

Both codes have been modified and implemented with the possibility to rotate the crystal with respect to the grid by a combination of Euler angles. Furthermore, the expression of the orientation-dependent anisotropy parameter $\eta(\vec{n})$ and its derivatives

were implemented with Equations (2.12) and (2.14). They can be used independently to impose the anisotropy of the crystal (rotating with it) and/or to correct the grid anisotropy (fixed with respect to the axis).

4.1.3 Data analysis

The phase-field results of both codes are generated in VTK² compatible file formats. The regular grid fields are stored in image files (.vti) while adaptive grid results are stored in unstructured files (.vtu). The interface position is extracted from the $\phi = 0.5$ and $\psi = 0$ isosurfaces, respectively. The dendrite tip position is then given by the intersection of the isosurface with the desired direction on the grid. The interface velocities are calculated by a first-order finite difference backward scheme on the interface positions.

A salient feature of the regular grid is that the mean curvature of the interface can easily be calculated by the divergence of the normal to the interface

$$H = -\frac{1}{2}\nabla \cdot \vec{n} \quad (4.1)$$

An algorithm based on this relation and VTK routines developed by Chapuis [Cha10] at LSMX was used for this purpose. The mean curvature is mapped on the isosurface and can thus be accessed at any given point.

Visualization of the dendritic structures is performed with ParaView, the open-source software package based on VTK.

4.2 Simulation parametrization

The FE model uses non-dimensional variables and parameters. This section will show how their values have been selected.

The alloy that has been chosen for the phase-field modeling is an Al-10 wt.% Zn. It matches the dilute alloy assumption and presents a short freezing range, hence a rapid development of the structure upon cooling.

The properties listed in Table 4.2 were used for the simulations. The diffusion coefficients were purposely lowered by a factor approximately 2 in order to allow for bigger time stepping, imposed by the Fourier number ($Fo = \frac{D_t \Delta t}{\Delta x^2} = 0.12$) in the explicit scheme of the FD model. Thus, a typical time step was $\Delta t = 1 \times 10^{-6}$ s for a grid spacing $\Delta x = 0.1 \mu\text{m}$.

In the case of the FE model, several constraints have to be met. Echebarria *et al.* [Ech04] showed that mesh converged results can be obtained with W_0/d_0 as large as 50. We recall that W_0 is the interface thickness parameter³ and d_0 the chemical capillary length. With the properties above, the assumption that $c_\ell^0 = c_\infty/k_0 = c_0/k_0$, (2.35) gives:

$$d_0 = 5.05 \times 10^{-9} \text{ m} \approx 5 \times 10^{-9} \text{ m}$$

Futhermore, the smallest expected tip radius is around 1×10^{-6} m and using the rule that it should be at least ten times the interface width, we have:

$$R_{\text{tip}}/W_0 = 10 \quad W_0 = 1 \times 10^{-7} \text{ m}$$

²Visualization Toolkit, an open-source, software system for 3D computer graphics, image processing and visualization

³the diffuse interface actually spreads over approximately $6W_0$

Table 4.2: Material properties chosen for the phase-field simulation and value found in literature for the composition and temperature considered.

Property	Value in simulation	Literature
c_0	0.1	-
m_ℓ	-170 K	-170 K [Mey86]
k_0	0.45	0.45 [Mey86]
T_M	660 °C	660 °C [Mey86]
D_ℓ	$1.2 \times 10^{-9} \text{ m}^2/\text{s}$	$2.75 \times 10^{-9} \text{ m}^2/\text{s}$ [Du03]
D_s	$1.2 \times 10^{-12} \text{ m}^2/\text{s}$	$2.7 \times 10^{-12} \text{ m}^2/\text{s}$ [Du03]
$\Gamma_{s\ell}$	$1.05 \times 10^{-7} \text{ Km}$	$1.05 \times 10^{-7} \text{ Km}$ [Mor07, Val10]
ρL_f	$1 \times 10^9 \text{ J/m}^3$	$1.07 \times 10^9 \text{ J/m}^3$ [Val10]
ρc_P	$3 \times 10^6 \text{ J/m}^3\text{K}$	$2.93 \times 10^6 \text{ J/m}^3\text{K}$ [Smi83]

and thus $W_0/d_0 = 20$. With Equation (2.58), we obtain $\tilde{D}_\ell = 5.5$ and therefore $\tau_0 = 4.6 \times 10^{-5} \text{ s}$. All other physical values like the thermal length, the pulling velocity and the simulation box size are then adimensionnalized with these values of W_0 and τ_0 . Also, the non-dimensional liquidus slope is given by:

$$\tilde{m}_\ell = \frac{|m_\ell|c_\ell^0}{L_f/c_P} = 0.11$$

Lastly, since one model is controlled by the imposed undercooling ($\Delta T \approx m_\ell(c_0 - c_\ell^*)$) and the other by the supersaturation defined as $\Omega = (c_0 - c_\ell^*)/c_\ell^*(k_0 - 1)$, we can give the two following relationships:

$$\Delta T = m_\ell c_0 \left(1 - \frac{1}{1 - (1 - k_0)\Omega} \right) \quad \Omega = \frac{\Delta T}{(\Delta T - m_\ell c_0)(1 - k_0)} \quad (4.2)$$

Table 4.3 gives the two parameters for the corresponding values seen in this work.

Table 4.3: Approximate relation between undercooling and supersaturation for the alloy presented in Table 4.2.

ΔT [K]	0.5	1	2	3.25	3.36	4.79	6.44
Ω	0.052	0.101	0.191	0.292	0.3	0.4	0.5

4.3 Mesh Anisotropy Assessment and Correction

The mesh anisotropy was assessed in two different ways. The first method, called static hereafter, originally proposed by Karma and Rappel [Kar98], consists of equilibrating a solid seed until the velocity of the interface is null, measuring the radii in the different crystallographic directions and comparing them to the $\vec{\xi}$ -plot.

The second method is to grow dendrites of various directions with respect to the grid with a fixed imposed crystal anisotropy, to compare their velocity and then to adjust the grid anisotropy correction until the velocities are identical along any direction. Figure 4.1 shows a schematic representation of simulation configurations used in these two methods.

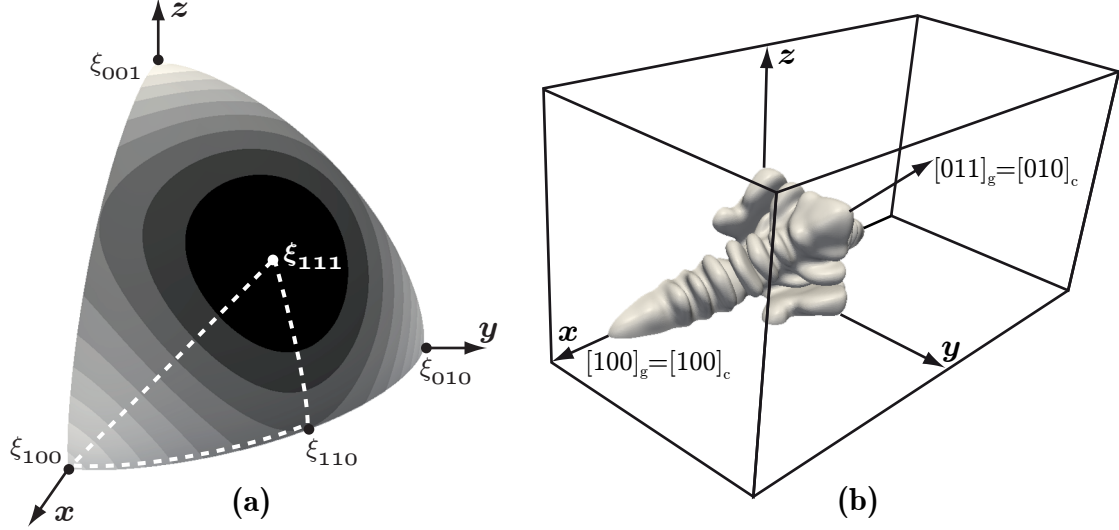


Figure 4.1: Schematic representation of the simulation configurations used to evaluate static (a) and dynamic (b) mesh anisotropy. (a) Eighth of an equilibrium shape in one octant of the reference frame. The radii or the norm of $\vec{\xi}$, shown here in a gray scale, are measured along the principal crystallographic axes. The dashed line shows the smallest symmetry unit of the cubic crystal. As will be seen later all the information about the characteristic radii or curvatures is contained in this spherical triangle and can be mapped on the whole sphere/equilibrium shape by symmetry. (b) The velocity of the dendrite tips growing in different directions with respect to the grid are measured.

4.3.1 Static

The theoretical radii of an equilibrium shape in the 3 directions $\langle 100 \rangle$, $\langle 110 \rangle$ and $\langle 111 \rangle$ (up to a scaling factor) are given by the norm of the $\vec{\xi}$ -vector, *i.e.*, by injecting the corresponding equation for $\gamma_{sl}(\vec{n})$ in Equation (2.20). If the simple fourfold formulation (2.14) is used

$$\xi_{100} \propto (1 + \varepsilon_4) \quad \xi_{110} \propto (1 - \varepsilon_4) \quad \xi_{111} \propto \left(1 - \frac{5\varepsilon_4}{3}\right) \quad (4.3)$$

If Fehlnner and Vosko's formulation, $(1 + \varepsilon_1 \mathcal{K}_1 + \varepsilon_2 \mathcal{K}_2)$, is used

$$\xi_{100} \propto \left(1 + \frac{2\varepsilon_1}{5} + \frac{4\varepsilon_2}{7}\right) \quad \xi_{110} \propto \left(1 - \frac{\varepsilon_1}{10} - \frac{13\varepsilon_2}{14}\right) \quad \xi_{111} \propto \left(1 - \frac{4\varepsilon_1}{15} + \frac{64\varepsilon_2}{63}\right) \quad (4.4)$$

To make the method independent of the radius of the seed that is chosen, it is convenient to calculate the ratio between the different directions. We define

$$\rho_a = \frac{\xi_{111}}{\xi_{100}} \quad \rho_b = \frac{\xi_{110}}{\xi_{100}} \quad (4.5)$$

Thus for a formulation with one anisotropy parameter, one radius ratio is sufficient to deduce this parameter. If we combine (4.3) and (4.5), there are two possibilities to calculate the effective ε_4

$$\varepsilon_{4\text{eff}a} = \frac{8}{5 + 3\rho_a} - 1 \quad \varepsilon_{4\text{eff}b} = \frac{1 - \rho_b}{1 + \rho_b} \quad (4.6)$$

Since a $\vec{\xi}$ -plot with a positive value of ε_4 has its maximum along $\langle 100 \rangle$ and its minimum along $\langle 111 \rangle$, $\varepsilon_{4\text{eff}a}$ will have the highest precision.

If the other formulation is taken up to the first order only, $(1 + \varepsilon_1 K_1)$, we obtain

$$\varepsilon_{1\text{eff}a} = \frac{15(1 - \rho_a)}{2(2 + 3\rho_a)} \quad \varepsilon_{1\text{eff}b} = \frac{10(1 - \rho_b)}{1 + 4\rho_b} \quad (4.7)$$

Equivalently, if we take only the sixfold term $(1 + \varepsilon_2 K_2)$, a positive value of ε_2 generates maxima along $\langle 111 \rangle$ and minima along $\langle 110 \rangle$. Thus, to have the highest precision, we define a third radius ratio

$$\rho_c = \frac{\xi_{111}}{\xi_{110}} \quad (4.8)$$

Accordingly, the different $\varepsilon_{2\text{eff}}$ are given by

$$\varepsilon_{2\text{eff}a} = \frac{63(1 - \rho_a)}{4(9\rho_a - 16)} \quad \varepsilon_{2\text{eff}b} = \frac{14(1 - \rho_b)}{13 + 8\rho_b} \quad \varepsilon_{2\text{eff}c} = \frac{126(\rho_c - 1)}{128 + 117\rho_c} \quad (4.9)$$

Finally, when considering both terms in this anisotropy expansion, we have

$$\varepsilon_{1\text{eff}ab} = \frac{35(35 - 27\rho_a - 8\rho_b)}{22(10 + 9\rho_a + 16\rho_b)} \quad \varepsilon_{2\text{eff}ab} = \frac{105(1 + 3\rho_a - 4\rho_b)}{22(10 + 9\rho_a + 16\rho_b)} \quad (4.10)$$

All these expressions are given and used in order to estimate the error that is to be expected from the measurements. Each individual $\varepsilon_{i\text{eff}}$ has its own error coming from the measurement of the radii ξ_i . The later is determined from the initial condition of the simulations. The measurement of the radius of the originally perfectly spherical seed in three different directions ($\langle 100 \rangle$, $\langle 110 \rangle$ and $\langle 111 \rangle$) gives the precision of the interpolation of the interface. The last common digit of three radii is taken as the error on the radius. A standard error calculation method is then used to determine the errors on the $\varepsilon_{i\text{eff}}$ calculated with the different formulas above. The largest calculated error for each $\varepsilon_{i\text{eff}}$ is finally reported in Figure 4.3 and Figure 4.5.

As opposed to the technique used by Karma and Rappel [Kar98] where the undercooling is adjusted, we chose to fix the undercooling and let the phase fraction evolve until equilibrium is reached. To minimize the CPU time needed to reach this state, the initial phase fraction (*i.e.*, seed radius) is set as close as possible to the target value. Furthermore, the limiting diffusion coefficient in the solid, D_s , is set to the value of D_ℓ to accelerate the procedure since only the equilibrium state and not the evolution is of interest.

Figure 4.2 shows the evolution of the phase fraction with time for two slightly different initial seed sizes. The equilibration is driven by two phenomena, the precise adjustment to the undercooling, and the minimization of the interfacial energy including anisotropy. The former is seen at the beginning of the curves whereas the latter provokes minute changes which cannot be seen with the selected scale. The time necessary to reach equilibrium depends on the initial seed size, typically 0.6 s for seeds with 10 μm radius. The equilibrium was considered to be reached when the rate of phase fraction change fell below $1 \times 10^{-5} \text{ s}^{-1}$.

In order to verify the sensitivity of the effective anisotropy on the size of the seed (comparable to the radius of a dendrite tip later on), the latter was varied at fixed grid spacing. The results for $\Delta x = 0.1 \mu\text{m}$ are shown in Figure 4.3. Three sets of equilibrium shapes were calculated, imposing $\varepsilon_4 = 4\%$ and measuring $\varepsilon_{4\text{eff}a}$, or in the Fehlnner-Vosko

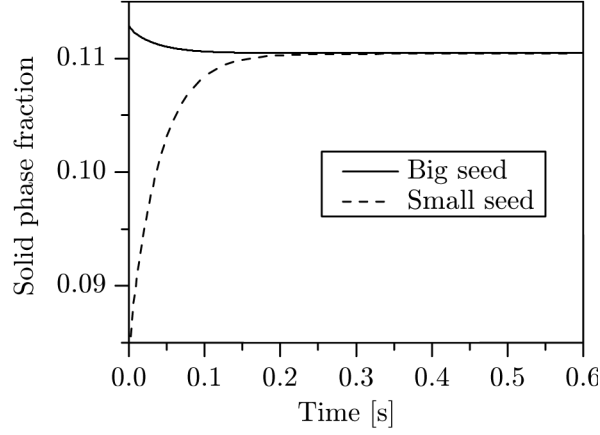


Figure 4.2: Phase fraction evolution toward equilibrium, with two different initial seed sizes. The big seed had an initial radius of $10\text{ }\mu\text{m}$ in a simulation domain $16.8 \times 16.8 \times 16.8\text{ }\mu\text{m}^3$. The small seed started with an initial radius of $9\text{ }\mu\text{m}$ in the same box.

formulation, imposing $\varepsilon_1 = 4\%$ and $\varepsilon_2 = -2\%$ and measuring $\varepsilon_{1\text{eff}a}$) and $\varepsilon_{2\text{eff}c}$ respectively. These results show that grid anisotropy (discrepancy between ε_i and $\varepsilon_{i\text{eff}}$) is constant for a wide range of equilibrium radii, but the relation breaks down below $R_E/\Delta x = 20$. This means that above this value, the effect of the grid can be accounted for and corrected, whilst below, this is more difficult. Almost identical results have been obtained with $\Delta x = 0.15, 0.2$ and $0.4\text{ }\mu\text{m}$.

In practice, the consequence is that the radius of the tip of a dendrite must be described by at least 20 grid spacings. For $\Delta x = 0.1\text{ }\mu\text{m}$, the smallest R_{tip} allowable is thus $2\text{ }\mu\text{m}$, and $4\text{ }\mu\text{m}$ for $\Delta x = 0.2\text{ }\mu\text{m}$. Figure 4.4 shows that this limits the undercooling or tip velocity that can accurately be modeled by the values given in Table 4.4.

Table 4.4: Limit values of solidification parameters for which the grid anisotropy can be corrected accurately.

Δx [μm]	R_{tip} [μm]	v_{max} [$\mu\text{m/s}$]	ΔT_{max} [K]
0.1	2	135	2.45
0.2	4	33	1.4

Since for computational efficiency the highest growth speed or undercooling are desirable, we determined the value of the correction that should be applied to account for the grid at $R_E/\Delta x = 20$. Values of $\varepsilon_{i\text{eff}}$ for the range of anisotropy to be used have been calculated by varying the imposed ε_i with this ratio. Only one parameter was varied at the time. Figure 4.5 shows that the measured values are lying so close to the ideal case (gray lines) that the grid anisotropy can barely be measured and is on the order of some hundredth of a percent. Note though that the errors on the measurement are of the same order of magnitude. Thus, the grid anisotropy can apparently be considered negligible as long as the limits shown in Table 4.4 are considered.

The computation complexity, and thus time, in the FE model scales with the number of elements/nodes, *i.e.*, is in direct relation to the surface area of interface. This means the more complex or extended (in the case of a big radius equilibrium shape) the interface, the slower the calculations. Furthermore, since this is a one-sided model, equilibration of a seed should be active (adjusting the undercooling), as suggested by Karma and

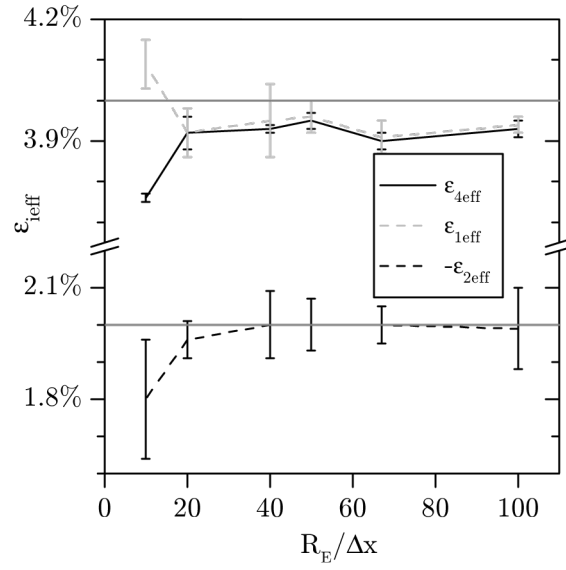


Figure 4.3: Effective anisotropies ε_{ieff} as a function of the radius of the equilibrium shape for $\Delta x = 0.1 \mu\text{m}$. The imposed values are $\varepsilon_4 = 4\%$, $\varepsilon_1 = 4\%$ and $\varepsilon_2 = -2\%$ and represented by the horizontal gray lines.

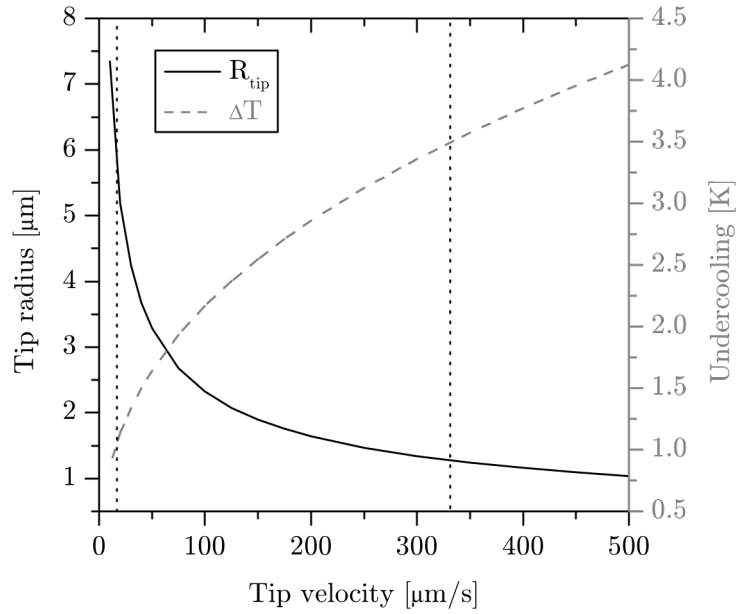


Figure 4.4: Relation between dendrite tip radius, growth speed and undercooling calculated with (2.30) and (2.33) for the alloy presented in Table 4.2 (Al-10 wt.% Zn). The vertical dotted lines represent the range of velocities of the Bridgman experiments.

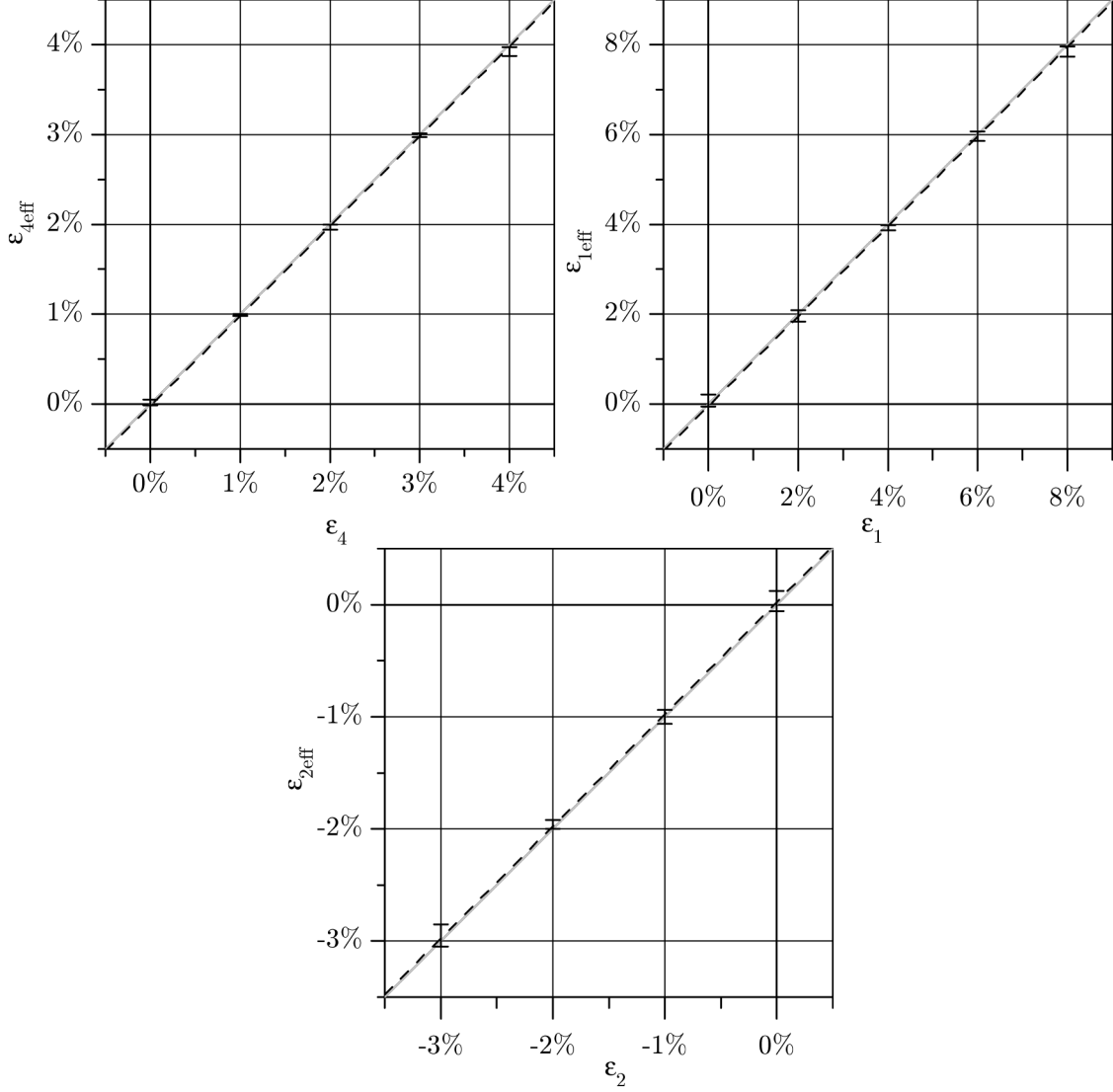


Figure 4.5: The effective anisotropies $\varepsilon_{i\text{eff}}$ as function of the imposed anisotropy ε_i for the static case for $R_E/\Delta x = 20$. The gray lines show the ideal case without grid anisotropy. The dashed lines correspond to the least square fit (with an imposed slope 1, condition for a grid anisotropy independent of the imposed ε_i) of the phase-field measurements. The intercept with the vertical axis, gives the value of the grid anisotropy $\varepsilon_{i\text{cor}}$. The obtained values are $\varepsilon_{4\text{cor}} = -0.022\%$, $\varepsilon_{1\text{cor}} = -0.048\%$ and $\varepsilon_{2\text{cor}} = +0.023\%$ respectively.

Rappel [Kar98]. However, such a procedure is not offered in the FE code and was not thought worth implementing since the method for the dynamic determination of grid anisotropy presented hereafter is not penalizing, from a computation time point of view.

4.3.2 Dynamic

The limits found for the FD model are very constraining in terms of growth speed and undercooling that can be selected, and thus require significant computational resources. Thus, the method consisting of growing dendrites in different orientation with respect to the grid was scarcely applied to this code. Thanks to the symmetry of the cubic crystal, only one octant was calculated and by rotating the crystal by 45° around the z -axis, only one simulation is necessary to obtain data for two directions. Further, to simplify the procedure, we reduced the number of parameters by choosing the expression for the grid anisotropy correction featuring only the ε_4 term.

We took as an example an equiaxed dendrite complying to the limits stated above, growing at $\Delta T = 1$ K for 0.5 s in a box $60 \times 60 \times 80 \mu\text{m}^3$ with $\Delta x = 0.2 \mu\text{m}$, $\varepsilon_4 = 1\%$ and an initial seed size $R_0 = 1 \mu\text{m}$. Although the initial transient is very long at that undercooling, the velocity tends towards a speed of $v_{\text{tip}} \approx 22 \mu\text{m/s}$ with a tip radius of $R_{\text{tip}} = 4.4 \mu\text{m}$. Without grid anisotropy correction, the velocities of the tips growing along the $[001]_g$ and $[110]_g$ directions of the grid differ by 2% only. Figure 4.6 shows that the best fit for a null relative velocity difference of the tips corresponds to $\varepsilon_{4\text{cor}} = -0.2\%$. This value is one order of magnitude higher than the one found in the previous section.

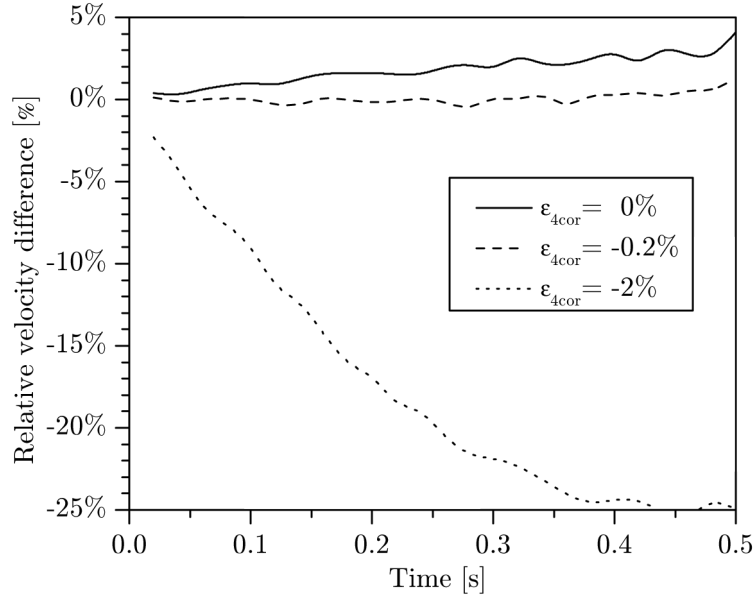


Figure 4.6: Relative velocity differences of two tips growing along the $[001]_g$ and $[110]_g$ directions of the grid, for different values of grid anisotropy correction. $\Delta x = 0.2 \mu\text{m}$, $\varepsilon_4 = 1\%$, and $\Delta T = 1$ K.

A scan through different undercoolings with all other parameters remaining the same as above, leads to the results of Table 4.5 for a zero relative velocity between $[001]_g$ and $[110]_g$. As can be seen, at such a low imposed anisotropy, the correction $\varepsilon_{4\text{cor}}$ rapidly surpasses ε_4 . Thus, the meaningfulness of results obtained under those conditions is doubtful. Simulations with an undercooling as low as 1 K are not efficient from a computational

time point of view, since first, the structure evolves only very slowly, secondly the initial transient is very long, and thirdly very big calculation domains are necessary to avoid boundary interactions of the wide solute profile generated by low growth speeds.

Table 4.5: Solidification parameters and grid anisotropy correction for different undercoolings with $\Delta x = 0.2 \mu\text{m}$ and $\varepsilon_4 = 1\%$. The error on tip velocity comes from the fluctuation that can be seen in Figure 4.6. This is due to the scheme used to compute the velocity from the interface positions. The error on the radius is given by the standard deviation of the radii measured during steady state growth of the tip.

ΔT [K]	v_{tip} [$\mu\text{m/s}$]	R_{tip} [μm]	$\varepsilon_{4\text{cor}}$ [%]
1	22 ± 2	4.4 ± 0.2	-0.2
1.5	49 ± 3	3.3 ± 0.2	-0.56
2	74 ± 2	2.78 ± 0.07	-0.8
2.5	105 ± 3	2.7 ± 0.1	-1.2

Care needs also to be taken when high anisotropies are used since they sharpen the tip and might thus break the limits exposed above. The maximum allowable velocity and undercooling should then be corrected by using an anisotropy adapted value of σ^* in Equation (2.30). Table 4.6 shows this very well. By performing the same scan as above but with $\varepsilon_4 = 4\%$, one can notice that for the same undercoolings, the tip velocities are doubled and the tip radii divided by three approximately. Furthermore, at low undercooling, the correction necessary to compensate for the grid is lower compared to the previous case ($\varepsilon_4 = 1\%$). A strong crystal anisotropy thus masks the effect of the mesh. But as can be seen from the last line of Table 4.6, the correction rapidly increases to the point where even the shape of the tip is modified. In fact the tip radius did not decrease even if the velocity increased. This is understandable since the effective anisotropy is only half of the original value with this correction and $R_{\text{tip}}/\Delta x$ becomes very small.

Table 4.6: Solidification parameter and grid anisotropy correction for different undercoolings with $\Delta x = 0.2 \mu\text{m}$ and $\varepsilon_4 = 4\%$.

ΔT [K]	v_{tip} [$\mu\text{m/s}$]	R_{tip} [μm]	$\varepsilon_{4\text{cor}}$ [%]
0.5	12 ± 1	1.58 ± 0.09	0
1	49 ± 4	1.2 ± 0.1	0
2	163 ± 1	0.93 ± 0.05	-0.2
3.25	250 ± 2	1.25 ± 0.02	-1.9

By changing the grid spacing to $\Delta x = 0.1 \mu\text{m}$, the allowable tip velocity increases by a factor 4 and thus the time at which the tips start to interact with the boundaries is reduced by the same factor. The interaction will even be delayed since the distance needed ahead of the tip, the diffusion layer, is shorter. However, in 3D, the number of nodes necessary to represent the same volume is multiplied by $2 \times 2 \times 2 = 8$ and another factor of 4 is lost in the time step through the Fourier condition. Consequently, the computation time increased in total by a factor $\frac{8 \times 4}{4} = 8$. The time to allow a low anisotropy structure to develop therefore becomes unreasonable. Two cases with a high anisotropy enabled by the small grid spacing are summarized in Table 4.7. It shows that the undercooling, where a

correction is necessary to obtain a zero relative velocity difference along $[001]_g$ and $[110]_g$, has shifted towards higher values of ΔT . This effect can be attributed to the finer mesh.

Table 4.7: Solidification parameter and grid anisotropy correction for two undercoolings with $\Delta x = 0.1 \mu\text{m}$ and $\varepsilon_4 = 4\%$.

ΔT [K]	v_{tip} [$\mu\text{m/s}$]	R_{tip} [μm]	$\varepsilon_{4\text{cor}}$ [%]
2	253 ± 1	0.55 ± 0.05	0
3.25	625 ± 2	0.49 ± 0.02	-0.2

The velocity profiles for such a case at $\Delta T = 2 \text{ K}$ and $\varepsilon_4 = 4\%$, shown in Figure 4.7 indicates that after a short initial transient the relative velocity of the tips differs by less than 1% until 0.1 s of the simulation. At that point in time, due to the domain configuration, the $[110]_g$ tip starts to interact with the boundary, solute piles up and the tip slows down. Shortly after the same happens to the $[001]_g$ tip.

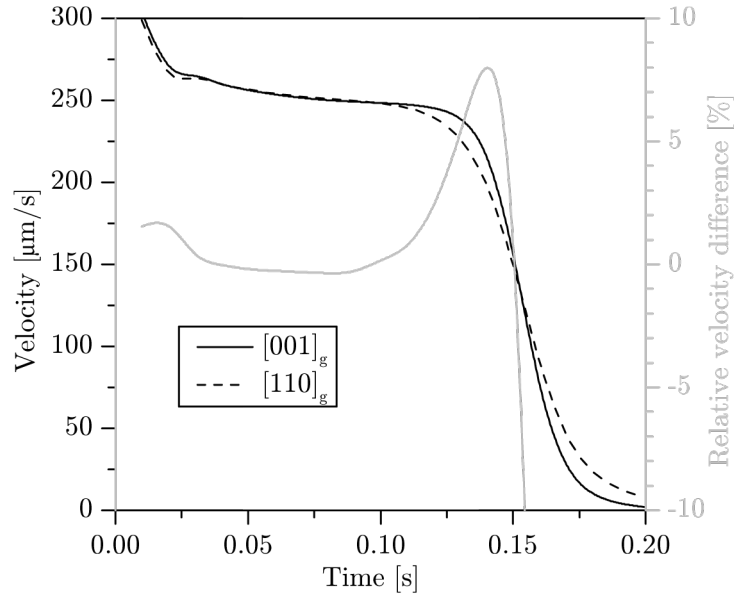


Figure 4.7: Velocity profile of two dendrite tips growing in $[001]_g$ and $[110]_g$ respectively. The solidification parameters were $\varepsilon_4 = 4\%$, $\Delta T = 2 \text{ K}$ and $R_0 = 1 \mu\text{m}$. The initial transient, the short steady-state and the effect of the interaction of the solute field with the domain boundaries are clearly visible. In the steady-state part of growth, the tip velocities are identical without any need of correction.

Finally, if we plot the obtained $\varepsilon_{4\text{cor}}$ as a function of the measured tip radii normalized by the grid spacing, Figure 4.8 shows that for a given imposed anisotropy, there is a critical radius below which correction for the grid is not possible anymore. Far before that, the correction can get as high as the imposed value of the anisotropy and substantially influence the tip radius. This is clearly shown by the data point with the strongest correction (last line of Table 4.6) where the radius is artificially increased by the correction counteracting the imposed anisotropy.

Growth along the $[111]_g$ direction has also been tried with the $\varepsilon_{4\text{cor}}$ giving the best correction between $[001]_g$ and $[110]_g$, and velocity discrepancies between the three directions were less than 1%.

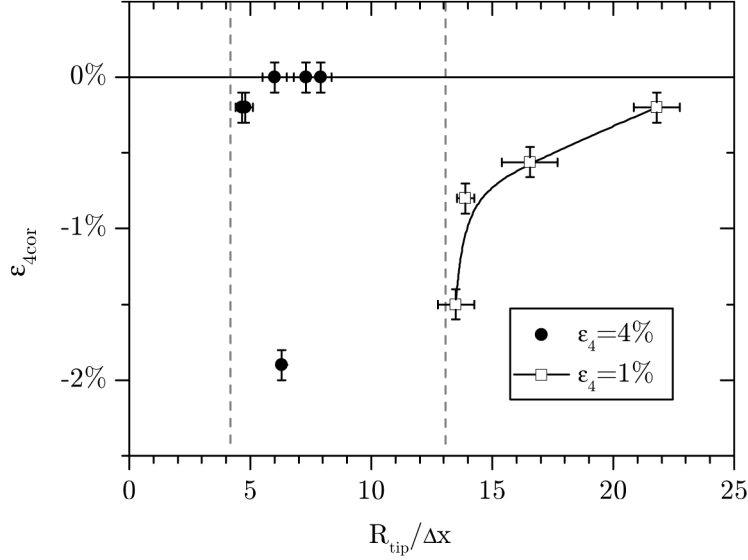


Figure 4.8: Grid anisotropy correction applied to obtain a zero relative velocity difference of the tips growing along $[001]_g$ and $[110]_g$, as a function of the measured tip radius normalized by the grid spacing, for two different imposed anisotropies. The gray dashed lines show the limits below which a correction can no more be applied.

The correction for grid anisotropy has the consequence that growth speeds and more so tip radii are not quantitatively predictive. Nevertheless, it ensures that no growth direction is favored, which is a key feature for the observation of a dendrite orientation transition.

Still, given the complex way grid anisotropy has to be taken care of, the FD code is prone to a lot of artifacts in the low anisotropy range that have to be dealt with for Al-Zn alloys. Moreover, the strong constraints on allowable growth velocities (undercooling) and thus the substantial computation times involved, make this model hard to use for a scan of the $(\varepsilon_1, \varepsilon_2)$ anisotropy parameter space, even on a massively parallel cluster. This is also one of the reasons the FE model was considered.

As for the FD model, grid anisotropy was assessed for the FE model. Since the latter is non dimensional, the parametrization is different from above and the reader is directed toward the next section for more details. The growth conditions for equiaxed dendrites are imposed through the supersaturation Ω . The higher Ω , the faster the structure evolves. Here, the crystal anisotropy was imposed by the $(1 + \varepsilon_1 K_1 + \varepsilon_2 K_2)$ formulation of γ_{sl} , but the mesh was still corrected with only $\varepsilon_{4\text{cor}}$. Mesh anisotropy was measured for $\Delta x/W_0 = 1$, $\varepsilon_1 = 4\%$ and for three different supersaturations. Figure 4.9 shows the results and Table 4.8 summarizes the optimum correction factors that were found.

Table 4.8: Grid anisotropy correction used to obtain a zero relative velocity difference of the tips growing along $[001]_g$ and $[110]_g$ for three different supersaturations, with $\Delta x/W_0 = 1$, $\varepsilon_1 = 4\%$.

Ω	0.5	0.4	0.3
$\varepsilon_{4\text{cor}}$ [%]	-3.35	-2.75	-2.63

If we remember that $\varepsilon_4 = 4\varepsilon_1$, these corrections are very important since their effect is 2 to 3 times stronger than the crystalline anisotropy. Since the anisotropy correction

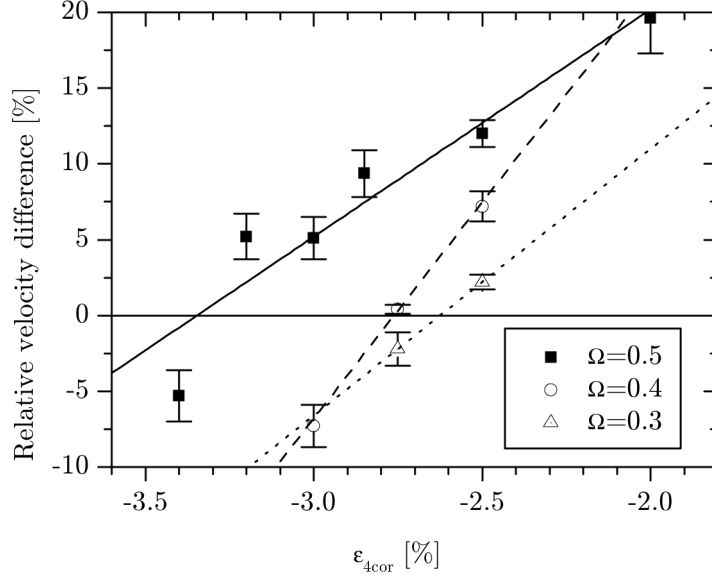


Figure 4.9: Relative velocity difference of the tips growing in $[001]_g$ and $[110]_g$ as function of the grid anisotropy correction for three different supersaturations. $\Delta x/W_0$ was 1 and the imposed crystal anisotropy was $\varepsilon_1 = 4\%$.

was shown to be tip radius dependent in the FD model, the corrections of Table 4.8 were tested with conditions for $\langle 110 \rangle$ dendrite growth to occur ($\varepsilon_1 = 0\%$, $\varepsilon_2 = -2\%$). Such dendrites are not only branching differently but have a tip with a broken rotational symmetry and thus two very different principal curvature radii. Up to a supersaturation of 0.4, the tip velocities along three different directions differed by less than 4%. Thus as mentioned before, with all these considerations, the model is not quantitatively predicting the tip speed and radius, but should nevertheless be able to describe the DOT. Above $\Omega = 0.4$, the correction becomes so strong that the dendrites have a tendency to tip split. Moreover, at such high supersaturation, the tips become so sharp that the grid probably describes their shapes too poorly. No tool was available to precisely measure the effective tip radius, but, it was estimated to be $R_{\text{tip}}/\Delta x = 10$. If the anisotropy cannot be corrected at such high supersaturation, these conditions are clearly not bareable to predict the DOT and should be avoided.

Although the corrections for the FE model are stronger than for the FD model, they still allow to make qualitative predictions in a regime were $R_{\text{tip}}/\Delta x \approx 15$, and thus allow higher growth velocities and much shorter computation times, thanks to the adaptive grid.

Chapter 5

Equilibrium Shapes and Interfacial Energy Anisotropy Measurement

Dendrites emerge and develop from solid seeds which are related to the crystal equilibrium shape and thus to the interfacial energy anisotropy. Over the years, several criteria for the prediction of dendrite orientation have been proposed without being able to describe all situations. The $\vec{\xi}$ -vector formalism greatly simplifies the analysis of the relation between γ -plot, $\vec{\xi}$ -plot, stiffness and curvature. The first part of this chapter will focus on the latest theoretical findings on these relations and the second part will focus on the measurement of the anisotropy parameters in highly alloyed Al-Zn, as well as on the Zn-Al side of the phase diagram.

5.1 Analytical Calculation of the Equilibrium Shapes

The $\vec{\xi}$ -vector formalism and the other tools presented in Section 2.1.4 and following, allow to analytically calculate the radii of an equilibrium shape and its curvatures for any anisotropy parameters. A Mathematica® module was written to compute the $\vec{\xi}$ -plot, the first and second principal curvatures as well as the mean curvature in the spherical triangle representing the smallest symmetry unit of the cubic crystal. Figure 5.1 shows the results obtained for a set of anisotropy parameters. These curvature calculations are used in the next sections to evaluate several criteria which are thought to predict a dendrite orientation transition with a variation of the anisotropy parameters.

5.1.1 Phase-Field Equilibrium Shapes

Modeling equilibrium shapes with phase-field does not make a lot of sense, except when mesh anisotropy needs to be estimated. Indeed, the $\vec{\xi}$ -vector formalism presented in Section 2.1.4, gives the analytical shape for any given anisotropy formulation and set of anisotropy parameters, which is straightforward and much faster than a full numerical simulation. The only area where this could be of interest, is when considering the interaction between several droplets equilibrating in close proximity to each other, which is generally the case in experiments. Indeed, during equilibration and thus coarsening, small droplets have a tendency to disappear in favor of the largest and the flux of solute generated by this phenomenon could slightly perturb the shape of the droplets. An effect which could be captured by phase-field, but which was not investigated in this work and is suggested as a perspective.

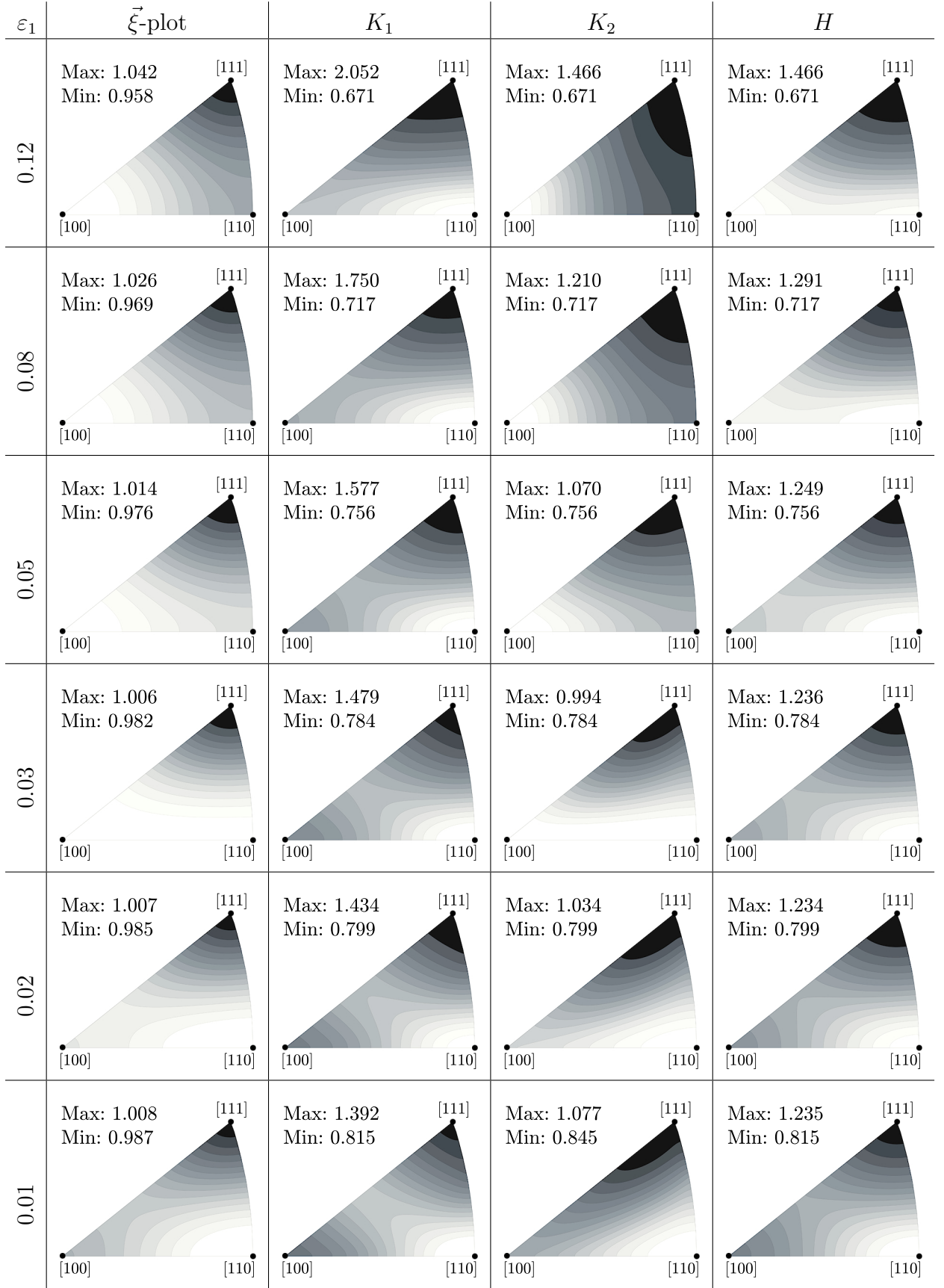


Figure 5.1: $\vec{\xi}$ -plot isovalues, first and second principal curvature and mean curvature maps computed for different values of ε_1 at fixed $\varepsilon_2 = -0.01$. The scales range from maximum (white) to minimum (black) in 15 gradations. All calculations are performed with an equilibrium shape radius of 1 (for an isotropic case) and presented in the smallest symmetry unit of the cubic system. The latter can be seen in Figure 4.1.

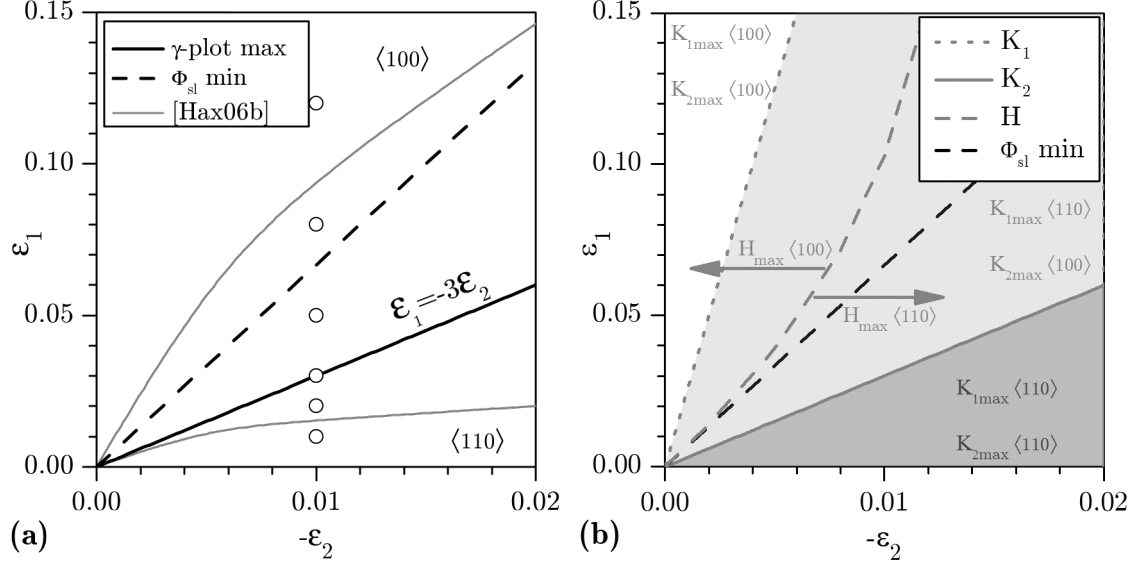


Figure 5.2: Anisotropy parameters space showing the different criteria that are or were thought to predict a dendrite orientation transition. (a) Criteria based on maximum of the γ -plot (continuous line) and minimum of the stiffness (dashed line). The two boundaries found by Haxhimali *et al.* [Hax06b] using phase-field calculations for the transition between $\langle 100 \rangle$, hyperbranched and $\langle 110 \rangle$ growth are also reported (the two extreme curves). The empty circles are the cases shown in Figure 5.1. (b) Criteria based on the actual local curvatures.

5.1.2 Dendrite Orientation Criterion

Originally, the dendrites were said to grow along the maximum of the γ -plot, which, for low anisotropy, also corresponds to the maximum of the ξ -plot, *i.e.*, the most prominent protrusion of the initial seed. However, such a criterion, used with Fehlner and Vosko's anisotropy development (2.12), lead to an abrupt transition between $\langle 100 \rangle$ and $\langle 110 \rangle$ at $\varepsilon_1 = -3\varepsilon_2$. This is due to the change in sign of the term multiplying Q in the γ_{sl} equation. This criterion is reported in Figure 5.2 (a) by a solid line. Above this line, the maximum radius of the equilibrium shape is along $\langle 100 \rangle$, and below it is along $\langle 110 \rangle$. Figure 5.1, shows the ξ -plot, the two principal curvatures and the mean curvatures obtained for the $(\varepsilon_1, \varepsilon_2)$ pairs highlighted in Figure 5.2 (a) to illustrate these different situations. Exactly on this line, the $\{001\}$ planes correspond to maximum of the γ -plot and ξ -plot and the case is degenerate. This criterion clearly lacks all the intermediate growth directions observed in experiments and phase-field simulations.

Later on, the already addressed minimum of the stiffness was suggested as a criterion. If the trace of the stiffness tensor¹ is considered, Haxihmali *et al.* [Hax06b] established that its minimum changes orientation around $\varepsilon_1 = -20\varepsilon_2/3$. Figure 5.2 (a) shows this criterion as a dashed line and the behavior is the same as for the maximum of the γ -plot, but with a different slope.

These stiffness minima usually correspond to the most “highly curved” regions of the solid-liquid interface of the equilibrium shape crystal, *i.e.*, where the mean curvature, H , is maximum, but not always. Indeed, Herring's relations (Equation (2.25)) cannot be

¹also called, Φ_{sl} , the generalized stiffness (2.26)

simplified as:

$$\begin{aligned} \frac{\Delta\mu}{V^m} = cst = K_1 \left[\gamma_{sl}(\vec{n}) + \frac{\partial^2 \gamma_{sl}(\vec{n})}{\partial n_1^2} \right] + K_2 \left[\gamma_{sl}(\vec{n}) + \frac{\partial^2 \gamma_{sl}(\vec{n})}{\partial n_2^2} \right] \\ \neq \underbrace{[K_1 + K_2]}_{2H} \underbrace{\left[\gamma_{sl}(\vec{n}) + \frac{1}{2} \left(\frac{\partial^2 \gamma_{sl}(\vec{n})}{\partial n_1^2} + \frac{\partial^2 \gamma_{sl}(\vec{n})}{\partial n_2^2} \right) \right]}_{\Phi_{sl}} \end{aligned} \quad (5.1)$$

This factorization is only valid along the considered growth direction when the two radii of curvature are equal. With the tools developed in Section 2.1.5, the calculation of the true principal curvatures of the equilibrium shape is possible. Figure 5.2 (b) shows the degeneracy lines of the two principal curvatures, K_1 and K_2 , and the mean curvature H . Above the upper dotted line (white zone), the two principal curvatures are maximum along $\langle 100 \rangle$, whereas below the lower continuous line (dark grey zone), they are both maximum along $\langle 110 \rangle$. Along each of these lines, one of the two curvatures is constant (or degenerate) in any of the $\{001\}$ planes, but the other is not. In between these two lines (light grey zone), one of the curvatures is maximum along $\langle 100 \rangle$ while the other is maximum along the $\langle 110 \rangle$. The stiffness criteria, which again calculates the transition between $\langle 100 \rangle$ and $\langle 110 \rangle$ by assuming the two radii of curvature to be equal in Herring's relation, is shown as in Figure 5.2 (a) by a heavy dashed line in the grey zone. However, if one now calculates in the $\{001\}$ planes the exact mean curvature H at any position, it is maximum along $\langle 100 \rangle$ on the left of the light dashed curve and becomes maximum along $\langle 110 \rangle$ on the right (see Figure 5.2 (b)). Please note that this transition curve is no longer linear and has a vertical asymptote for a value $\varepsilon_2 = -0.013$: Below this value ($|\varepsilon_2| > 0.013$), H is maximum along $\langle 110 \rangle$ for any value of ε_1 , providing it does not produce faceted dendrites. On the other hand, the mean curvature is degenerate along the dashed line in these $\{100\}$ planes because its maxima are equal along $\langle 100 \rangle$ and $\langle 110 \rangle$ and H takes a minimum value in between. The arrows on both side of the H -degeneracy line in Figure 5.2 (b) show along which direction the maximum mean curvature lays.

Interestingly the region where hyperbranched structures were found by Haxihmali *et al.* [Hax06b], correspond to the large light grey region where $K_{1\max}$ and $K_{2\max}$ point along different directions. Furthermore, it can be seen that the equivalence of the stiffness minimum and the mean curvature maximum criteria is only valid in a very limited region at very low anisotropy.

Obviously, a criterion considering the most highly curved region of the interface, H_{\max} , also leads to an abrupt transition between the two directions $\langle 100 \rangle$ and $\langle 110 \rangle$, or to no transition at all if $|\varepsilon_2|$ is too high.

Taking the fix value of $\varepsilon_2 = -0.02$ used by Haxihmali *et al.* [Hax06b] in their DOT as an example, Figure 5.3 shows the iso-curvature² plots for K_1 , K_2 , H and K the Gaussian curvature, as a function of the misorientation angle with respect to the $\langle 100 \rangle$ direction and of ε_1 . As mentioned above, this case is special since the position of H_{\max} does not make an orientation transition with increasing ε_1 . And as can be seen from the resemblance between Figure 5.3 (a) and (c), the general aspect and the values of K_1 and H are very close. In fact, the first principal curvature is so strong that it clearly dominates the second principal curvature in their contribution to the mean curvature.

Figure 5.4 shows the DOT observed at $\varepsilon_2 = -0.02$ (Figure 2.6 (b)) by Haxihmali *et al.* [Hax06b] in phase-field the simulations, superimposed to the first principal curva-

²in the (100) plane

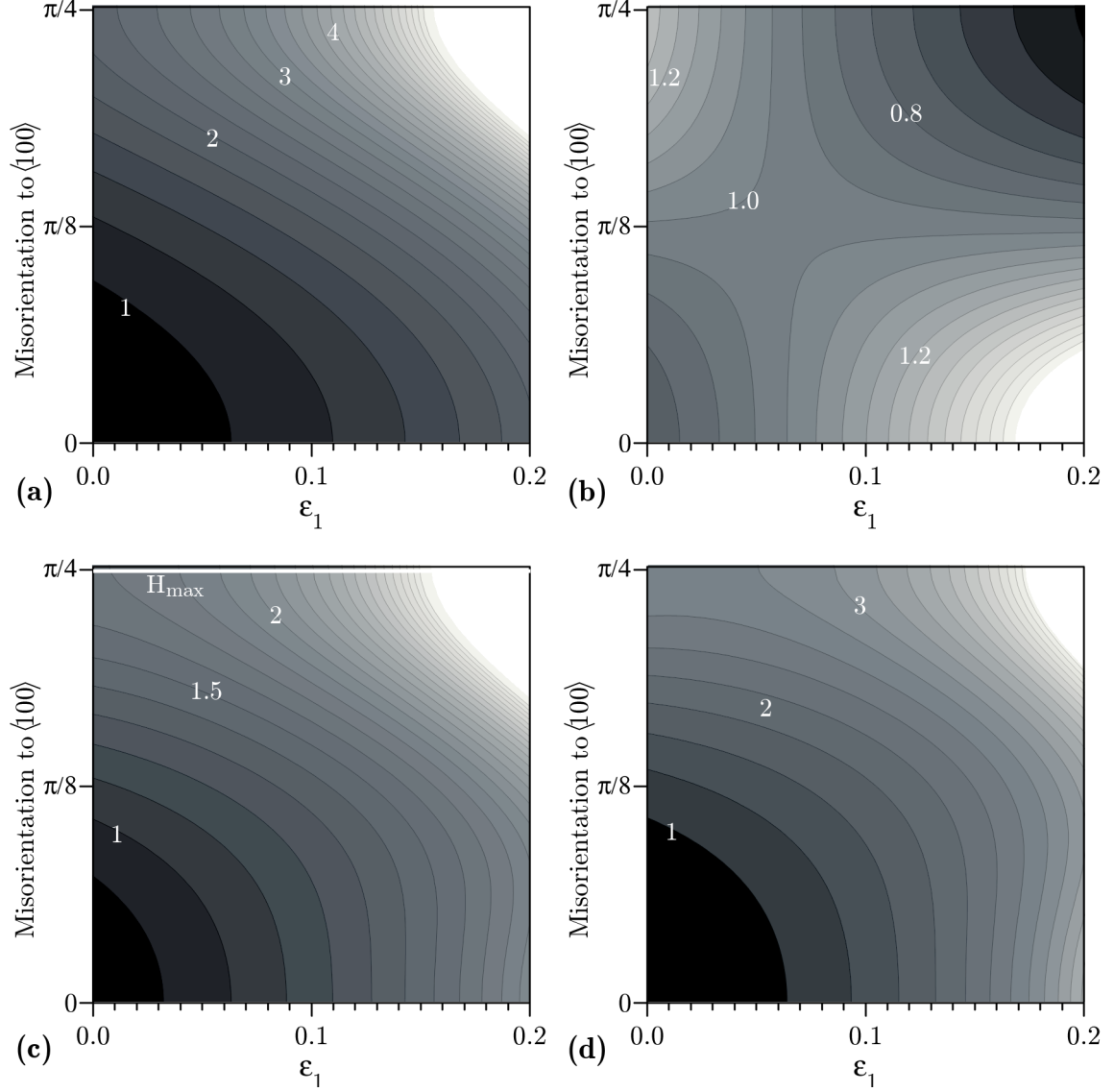


Figure 5.3: Isocurvature maps as function of ε_1 and the misorientation angle with respect to $\langle 100 \rangle$ in a (001) plane for a fixed value of $\varepsilon_2 = -0.02$. (a) First principal curvature K_1 , (b) second principal curvature K_2 , (c) mean curvature H and (d) Gaussian curvature K . The white numbers show the iso-curvature values. The curvatures have been scaled with $1/R_0$, where R_0 is the radius in the isotropic situation. The white line at the top of (c) shows that for this value of ε_2 , H_{max} does not change orientation with increasing ε_1 .

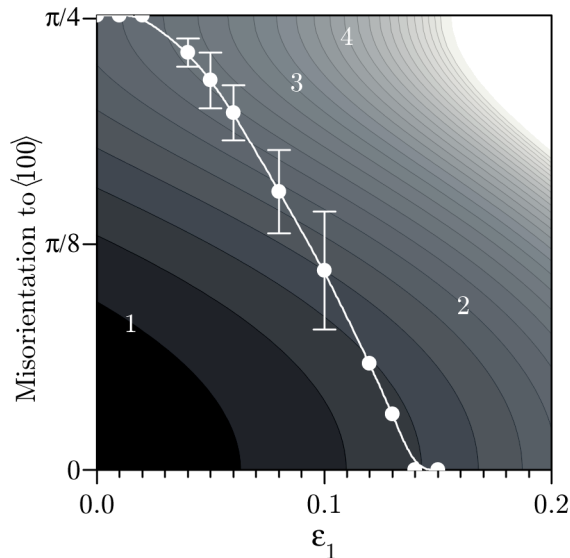


Figure 5.4: First principal curvature map for $\varepsilon_2 = -0.02$ with the superimposed DOT observed by Haxhimali *et al.* [Hax06b] in phase-field simulations.

ture map. Although the DOT does not follow a first curvature isovalue, the trend can nevertheless be seen.

Of course this analysis is even more interesting in the region where the maximum mean curvature can change direction based on the H_{\max} criterion in Figure 5.2 (b), *i.e.*, where ε_1 has an influence or when $|\varepsilon_2| < 0.013$. To be able to compare the results with the phase-field calculations of this work, the same type of iso-curvature maps have been calculated for $\varepsilon_2 = -0.01$ and are shown in Figure 5.5. This case corresponds to equiaxed phase-field calculations performed in the line scan LS3 which will be presented in Figure 6.11.

It will be shown in Chapter 6 that for $\varepsilon_2 = -0.01$, $\langle 100 \rangle$ dendrites are obtained if $\varepsilon_1 \geq 0.12$ and $\langle 110 \rangle$ if $\varepsilon_1 < 0.02$. From Figure 5.6 (a), a transition with this range could be obtained with a curvature value of $K_1 \approx 1.4^3$. Note the close resemblance between the shape of the latter and the DOT observed experimentally by Gonzales *et al.* [Gon06]. The hypothesis that the increase in zinc content decreases the value of ε_1 at a fixed ε_2 thus seems reinforced.

To complete this mapping of the anisotropy parameter space in terms of curvature, Figures 5.6 (c) and (d) show the K_1 maps for $\varepsilon_2 = -0.005$ and $\varepsilon_2 = -0.015$. An extrapolation from the limits for $\langle 100 \rangle$ and $\langle 110 \rangle$ growth found in this work by phase-field is shown in Figure 5.7. For the two cases $\varepsilon_2 = -0.005$ and $\varepsilon_2 = -0.015$, these limits, *i.e.*, transition ranges, are predicted by $K_1 \approx 1.2$ and $K_1 \approx 1.7$ respectively.

Since the H_{\max} criterion does not dictate a continuous orientation transition but certain values of K_1 seem to do, a careful⁴ analogy could be made if we recall the fundamentals of dendritic growth. In the selection of the tip radius and velocity, it was also found that the dendrite does not grow at the extremum but at some radius and velocity that satisfy the operating state given by the stability parameter, *i.e.*, some sort of optimum. Thus, the selected orientation could obey a similar optimum curvature criteria.

However, the reasons for the respective choice of curvatures leading to the correct transition range for the different value of ε_2 , are not understood yet and are therefore

³curvatures have been scaled with R_0 , where R_0 is the radius in the isotropic situation, taken as 1.

⁴not suggesting that the physics behind it is similar, but merely the concept.

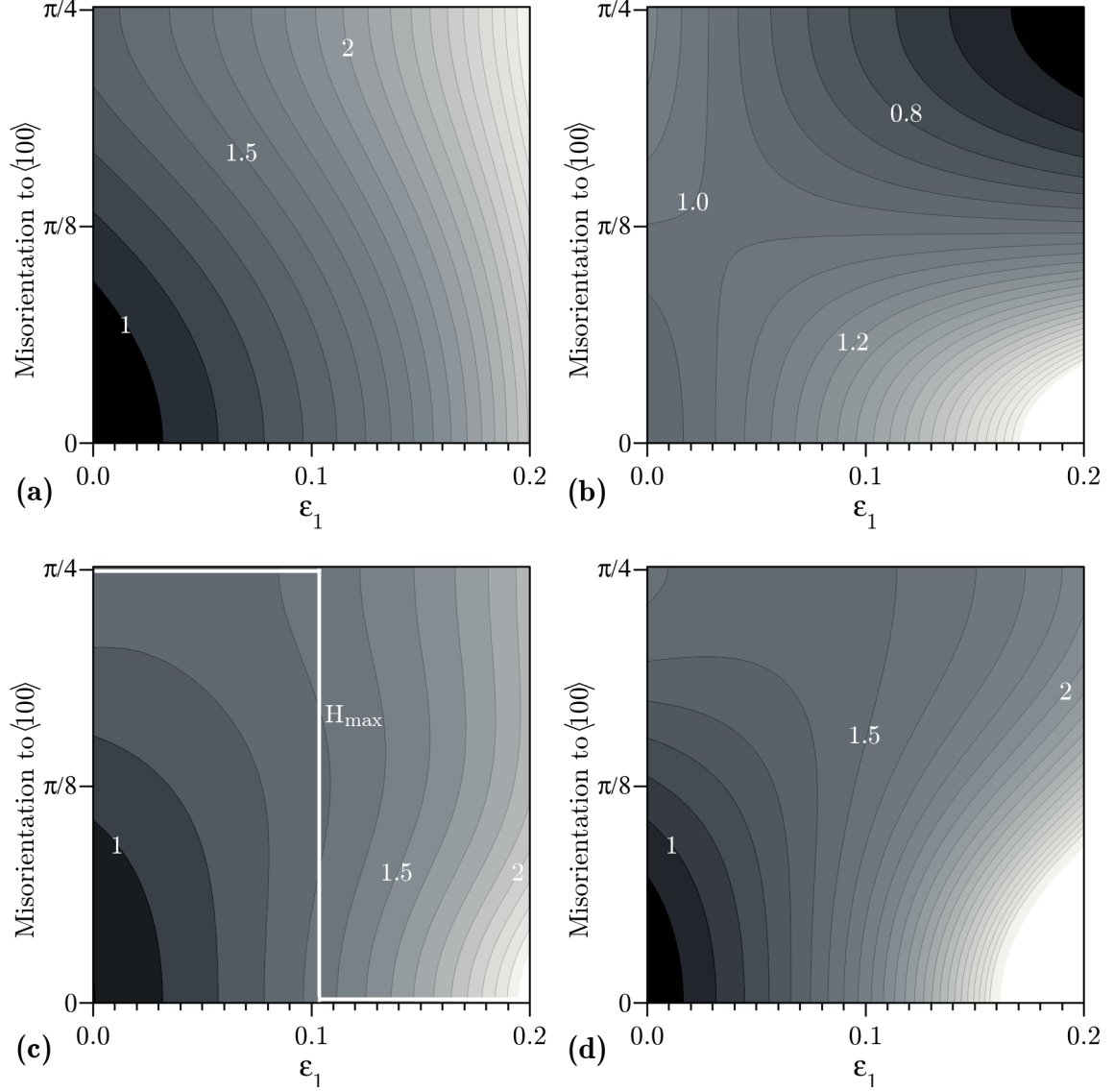


Figure 5.5: Isocurvature maps as a function of ϵ_1 and the misorientation angle with respect to $\langle 100 \rangle$ in a (001) plane for a fixed value of $\epsilon_2 = -0.01$. (a) First principal curvature K_1 , (b) second principal curvature K_2 , (c) mean curvature H and (d) Gaussian curvature K . The white line in (c) shows the abrupt change from $\langle 110 \rangle$ to $\langle 100 \rangle$ (at $\epsilon_1 = 0.1027$) based on the H_{\max} criterion of Figure 5.2 (b).

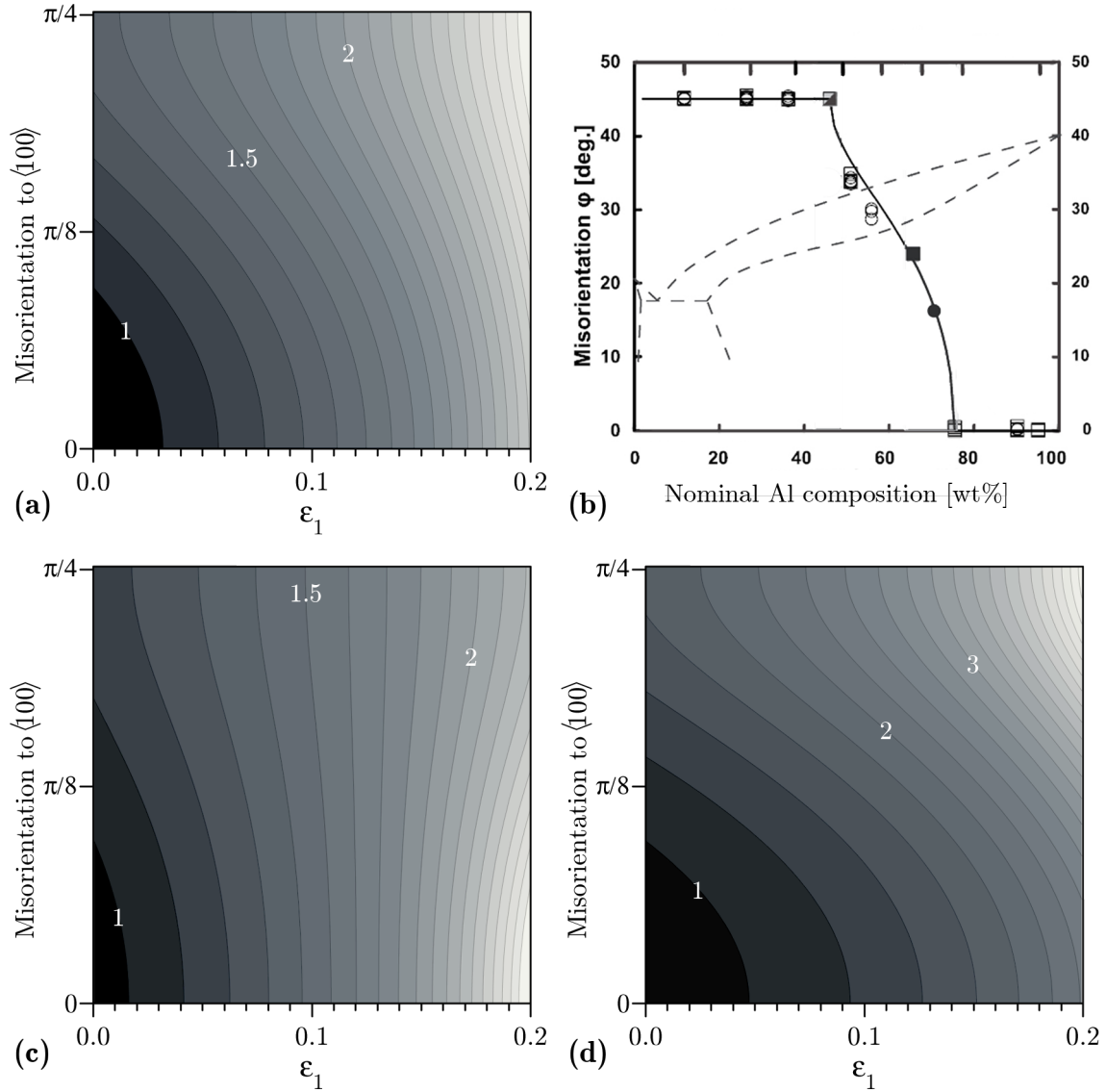


Figure 5.6: First principal curvature maps for $\epsilon_2 = -0.01$ (a) $\epsilon_2 = -0.005$ (c) and $\epsilon_2 = -0.015$ (d). The dotted lines represent the iso-curvature that would satisfactorily predict the orientation transitions observed by phase-field (Figure 5.7). (b) The DOT observed by Gonzales *et al.* [Gon06], mirrored horizontally for an easier comparison (*i.e.*, horizontal scale showing the Al composition).

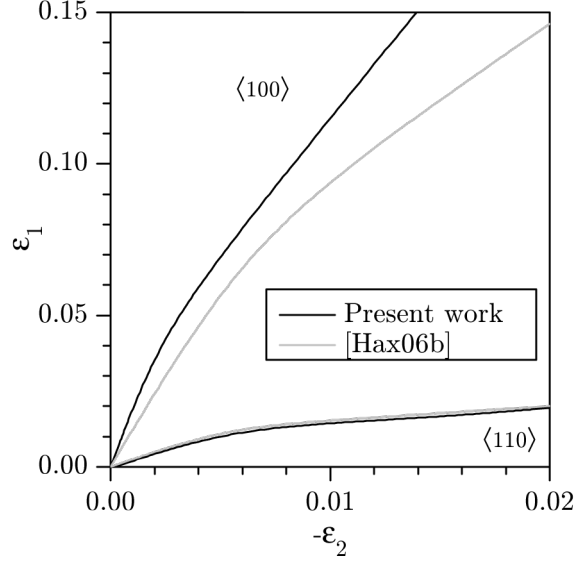


Figure 5.7: Transition limits between $\langle 100 \rangle$ and hyperbranched structures and between the latter and $\langle 110 \rangle$, observed by phase-field in Haxhimali *et al.* [Hax06b] and in this work. The lower limit is almost identical in both cases whereas the limits between $\langle 100 \rangle$ and hyperbranched structures is different.

totally empirical. A possible link is that the selection parameter, $\sigma^* \propto 1/R_{\text{tip}}^2 \approx K_1^2$ and Haxhimali [Hax06a] showed the relation between σ^* and the anisotropy parameters ε_1 and ε_2 for a stable $\langle 100 \rangle$ dendrite (Figure 2.4). Thus the critical⁵ value of σ^* , could give the selected first principal radius and therefore its orientation from a corresponding curvature map. More phase-field simulations showing the $\langle 100 \rangle$ and $\langle 110 \rangle$ tip splitting limits in the anisotropy parameter space are however needed to ascertain that such a criterion could be valid.

⁵when the combination $(\varepsilon_1, \varepsilon_2)$ predicts an instability of the $\langle 100 \rangle$ tip

5.2 Measurement of the Equilibrium Shapes

5.2.1 High Zinc Concentration Aluminum Phase Equilibrium Shape

The equilibrium shape and anisotropy parameters of low alloyed aluminum have already been determined by Napolitano *et al.* [Liu01, Nap02, Nap04] and this section will focus on the measurement of highly alloyed Al-Zn. The goal is to measure the anisotropy parameters leading to $\langle 110 \rangle$ dendritic growth.

Dual Isothermal Annealing Method

An Al-82 wt.% Zn specimen was produced with the dual step isothermal annealing procedure exposed in Section 3.3. After the first solid state hold for 200 h at 327 °C, the obtained particle density evolved from roughly $1/\lambda_1^2\lambda_2 = 500 \text{ mm}^{-3}$ to approximately 60 mm^{-3} (λ_1 and λ_2 are the primary and secondary dendrite arm spacings after Bridgman solidification). Such a long hold was necessary to ensure that connected interdendritic channels, which would drain above the solidus temperature, were no longer present. Particles were then between 5 and 80 μm in radius with a distribution biased towards larger sizes.

After the second step at 392 °C for 410 h, the droplet density dropped to $\sim 20 \text{ mm}^{-3}$ with radii between 10 and 100 μm , with again a tendency to form preferentially bigger particles. Although the precision of the radii measurement on a large droplet is increased for a given resolving power, such droplets are disadvantaged on several other factors: longer equilibration time due to a lower particle density and thus longer diffusion time; reduced curvature effect and larger influence of any thermal gradient. This phenomenon is illustrated by Figure 5.8, which shows the higher degree of sphericity of the smaller droplet for otherwise identical conditions.

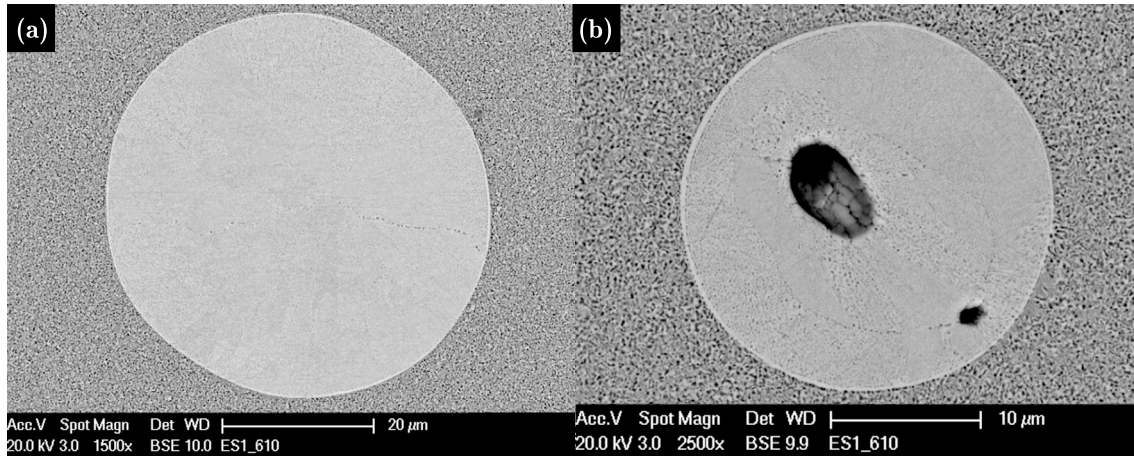


Figure 5.8: Equilibrium shapes in an Al-82 wt.% Zn sample, dual heat treated for a total of 610 h. Note that the scales between (a) and (b) are different, the droplet radii being 25 and 12 μm , respectively.

Tomography columns with diameters up to 600 μm and 4 mm in length (*i.e.* a total analysis volume of 1.1 mm^3) were machined in this sample. As a rapid calculation with the droplet density shows, the probability to find one full, right-sized droplet within this sample is very low. In fact, with the smallest pixel size achievable, 0.37 μm , to resolve

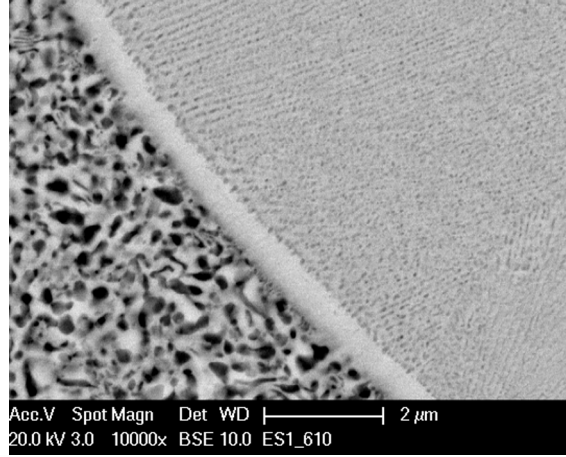


Figure 5.9: Interface region of the droplet in Figure 5.8 (b), showing the fine annulus and the two different structures in the former solid and quenched liquid phases of the sample. The monotectoid decomposition of the solid is on the left whereas eutectic lamellae can be seen to the right.

1% anisotropy, the droplet radius should be at least $74\mu\text{m}$. Within the five samples that were prepared, no satisfactory droplet in terms of size and equilibration could be found during the tomography experiments. Thus, to continue the analysis, FIB was chosen as a technique with a higher resolving power on limited size objects.

Before this next technique is addressed, standard SEM imaging and tomography already allowed certain conclusions to be deduced. Measurements are performed on quenched droplets, and the distortion of the droplet shape caused by the quenching process is considered to be negligible for two reasons. First, the volume change associated with solidification of the droplets is largely accommodated by the formation of fine cracks or voids in the interior of the droplet. Such cracks were already clearly observed in quenched droplets in an Al-Cu alloy [Liu01]. In the present case, cracks were not observed, but voids were identified both in sections (Figure 5.8 (b)) as well as in tomography stacks. Second, the volume “deficit” within the droplet accumulates gradually, as solidification proceeds from the outer shell inward. Thus, the cracks and voids that form to accommodate the solidification shrinkage primarily form near the center of the droplet, and the measured interface shape is not measurably affected.

Further, an enlargement of the interface region (Figure 5.9) shows a fine ($\sim 0.5\mu\text{m}$ wide) annulus between the monotectoid decomposition ($\alpha \rightarrow \alpha' + \beta$) on the outside (former single crystal aluminum) and the eutectic pattern on the inside (former liquid) of the droplet. The smoother surface and the finer resolution provided by the FIB sectioning allowed to see more details, as shown in Figure 5.10. The channeling contrast (sensitive to the crystal orientation) shows the grain boundaries of the crystals formed during the monotectoid reaction at the outer rim of the annulus. At the inner edge of this corona, *i.e.*, at the interface with the fine eutectic structure, the crystal seems to be continuous. The exact formation mechanism of this annulus is yet not totally clear, however certain hypotheses may be put forward. The corona could originate from the inward growth of the primary solid phase upon quenching, between the annealing temperature and the eutectic temperature, point at which the growth of the primary phase during quenching would be stopped by the eutectic transformation. Given the cooling rate and the very low temperature gap to reach 100% of solid fraction, no direction should have time to

build up a growth advantage, especially with the very smooth curvature of the spherical droplet. It thus seems reasonable to assume that the inner edge of the annulus is homothetic to the actual former solid-liquid boundary. Still, the reason for the corona not to decompose below the monotectoid temperature remains to be explained. In a way similar to the precipitate-free zone (PFZ) forming for example near grain boundaries in solid state transformations [Por01], it may be assumed that in the present case, it is energetically favorable for the system to form zinc between the eutectic and the monotectoid temperatures on already existing zinc precipitates, *i.e.*, on the zinc present in the eutectic structure, rather than nucleating new zinc precipitates in this zone. These hypotheses could, for now, not be tested further, but the growth of such a corona in the solid state, after the entire former matrix has decomposed, seems unlikely. Thus, although the inner edge of the corona is a discontinuous boundary, we think it is reasonable to consider it as the remainder of the original solid-liquid interface present during isothermal holding. In any case this interface is much smoother than the outer edge of the annulus and thus the only one available for the analysis we propose. Furthermore, this fine shell is apparently the only part of the sample which keeps the original crystal orientation of the zinc-rich aluminum matrix. Yet, accessing this information in such a small feature is hardly possible with EBSD and TEM measurement would be necessary. This latter technique would also be required to assess the precise chemical compositions of all the features in and around the corona and thus to help elucidate its formation.

Gradient Experiment Method

The use of the higher resolution FIB technique, on the other hand, constrained the maximum allowable size for the droplet to a radius of 5 μm . The gradient experiment gave access to such small sizes since it generates an even distribution of droplets between 0.1 and 1 μm and a density up to $2 \times 10^6 \text{ mm}^{-3}$ in small regions of interest. Consequently, the equilibration times were much shorter, a good sphericity of the droplets was attained after 2 h and treatments up to 16 h only decreased the droplets density. Indeed, the gradient experiment brings the drawback that it creates wet grain boundaries, which have to be accounted for in the phase fraction calculation for the equilibrium temperature and which absorb droplets close to them through coarsening due to their lower curvature. After two hours already, the droplets are found in colonies far from the wet grain boundaries (Figure 5.11 (a)).

Ideally, an isolated droplet at the center of a grain should be analyzed to minimize its shape perturbation by other droplets and by grain boundaries. However, from a practical point of view, finding such an equilibrium shape is not feasible. Indeed, to section an entire droplet by FIB it has to be very close to the surface. This is possible by using a high acceleration voltage which increases the electronic interaction volume below the sample surface in the microscope. Still, the obtained contrast is low and needs a slow scan time per image at high magnification. Applying such a method to a sample of several square millimeters cannot be considered. Even so, in droplet colonies, where the presence of buried droplets is suspected, this technique was proven fruitful as shown in Figure 5.11 (b). As opposed to a droplet which is cut by this section, the blurriness of the circular shape indicates that this droplet is below the surface.

Once such droplets are identified, positioning marks are dug around the desired location and a trench is excavated a few microns away to expose the imaging (also serial sectioning) face perpendicular to the sample surface (Figure 5.12). This face is then

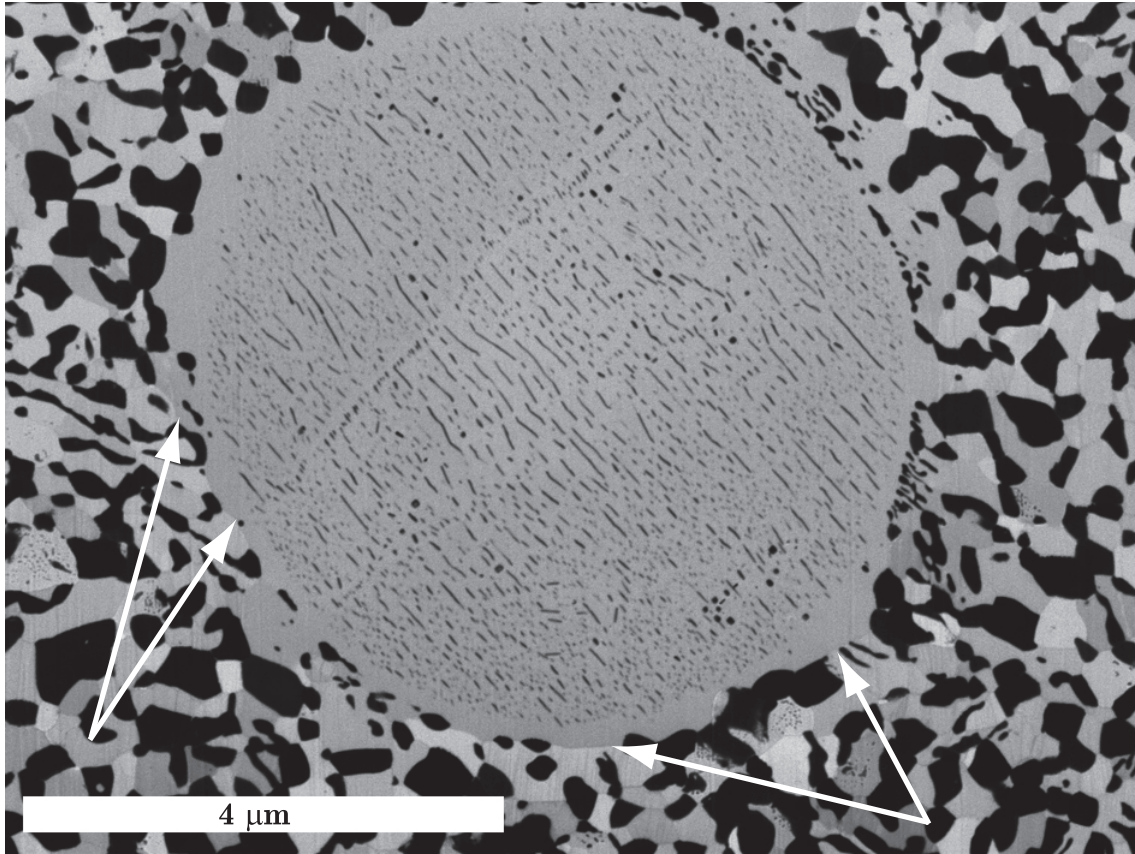


Figure 5.10: FIB slice of a droplet showing the detailed structure in and around the equilibrium shape. The image is a superposition of two micrographs recorded by the BSE and the in-lens detectors. The resulting image thus shows both the chemical contrast and the channeling contrast revealing the grain boundaries between the annulus and the grains formed by the monotectoid reaction (indicated by arrows). In the chemical contrast, the signal is proportional to the atomic number of the elements, the darkest features are thus Al-rich and the lighter ones Zn-rich.

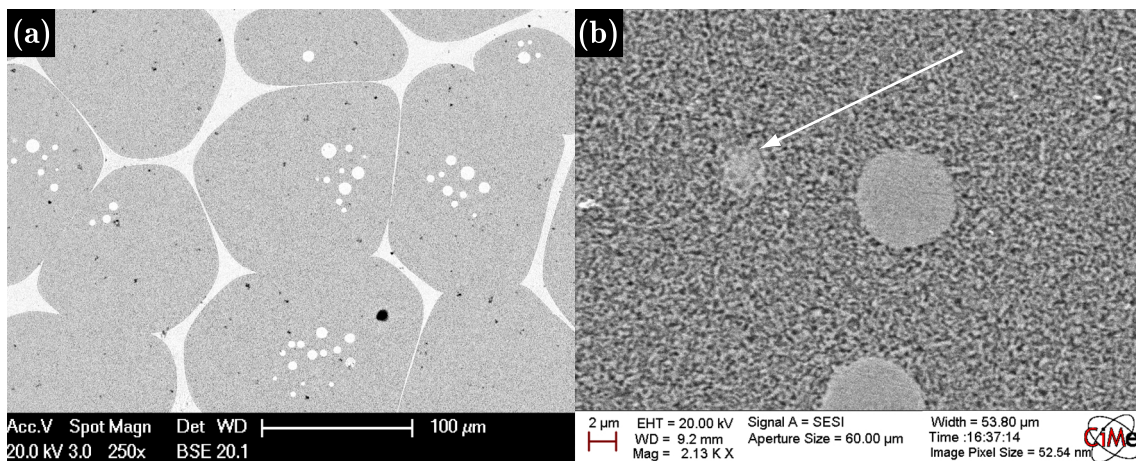


Figure 5.11: (a) Droplet colonies at the center of grains after 2 h heat treatment 5 °C above the liquidus. (b) High acceleration voltage SEM image showing part of a droplet colony and signs of an equilibrium shape below the surface.

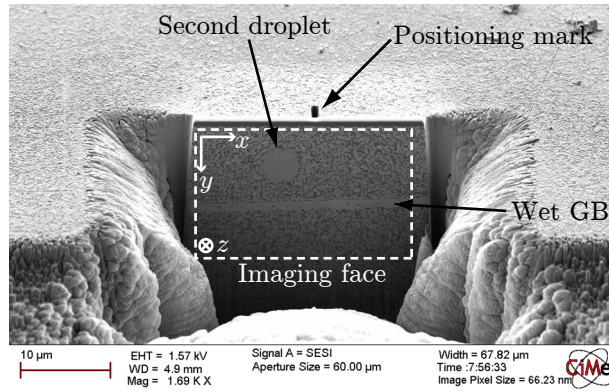


Figure 5.12: Trench milled by FIB showing the serial sectioning face on which the image stack is registered. A positioning mark can be seen at the surface of the sample in the middle of the face. Also visible are a wet grain boundary and a second droplet that appeared at the end of the milling sequence.

ablated in 20 nm thick steps to successively reveal the 3D shape of the droplet. The final reconstructed volume⁶ ($10 \times 10 \times 10 \mu\text{m}^3$) is a stack of images with a voxel size of $10 \times 10 \times 20 \text{ nm}^3$.

Figure 5.13 shows the result of the FIB serial sectioning, in a sequence of regularly spaced images of the droplet. Note that at the maximum diameter, the outer rim of the annulus reaches the surface, which is why the droplet could be identified in Figure 5.11 (b). Although the crystallographic orientation could not yet be determined precisely, care was taken to prepare the sample in such a way that the sectioning face corresponds to a cross section of the Bridgman solidification rods used as a precursor structure for subsequent steps. Orientation selection being strong at high zinc content, the z -axis of the image stack should thus lay within a few degrees to the $\langle 110 \rangle$ direction.

The analysis volume needs to be post-processed to extract the exact solid-liquid interface of the equilibrium shape. As mentioned before, the latter is given by the discontinuous exterior limit of the eutectic lamellae (see Figure 5.10). Since this is a very difficult problem, no automatic procedure yielded satisfactory results and the droplet was segmented manually. The resulting surface, colored by the relative distance to the droplet center of mass is shown in Figure 5.14. Since at least one orientation is known from the precursor structure, convexities of the equilibrium shape allow to identify the symmetries of the droplet as shown in Figure 5.15.

Determination of the Anisotropy Parameters

Knowing the approximate crystallographic orientation of the droplet, the radii ξ_{100} , ξ_{110} and ξ_{111} , were average over the 6, 12 and 8 corresponding directions that could respectively be measured. Their ratios ρ_a and ρ_b (4.5) were determined to be 1.006 and 1.048 respectively. Using Equation (4.10) and the procedure exposed in Section 4.3.1, the following set of anisotropy parameters was found, $\varepsilon_1 = -0.025 \pm 0.023$ and $\varepsilon_2 = -0.024 \pm 0.014$. Although the error is large, according to Figure 2.3 this combination of ε_1 and ε_2 produces structures with a strong $\langle 110 \rangle$ character, which is indeed what is observed in highly alloyed Al-Zn sample. More precise measurements could be achieved with an averaging over several, similarly oriented, droplets and by an exact determination of the crystal

⁶different from the total extracted volume of approximately $20 \times 20 \times 20 \mu\text{m}^3$

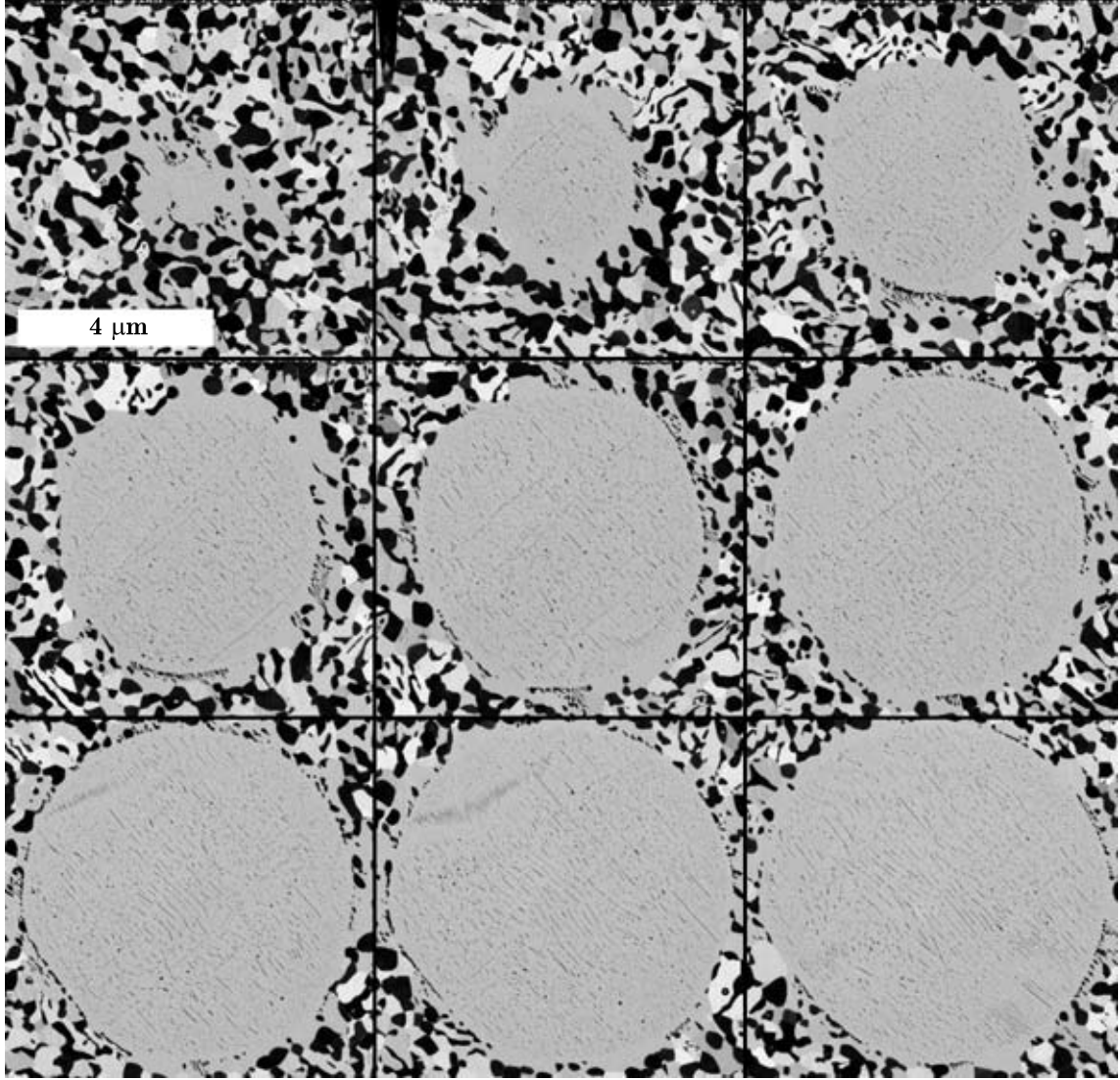


Figure 5.13: Sequence of FIB slices, 40 μm apart in depth, going from the edge of the droplet (top left) to the maximum diameter (bottom right).

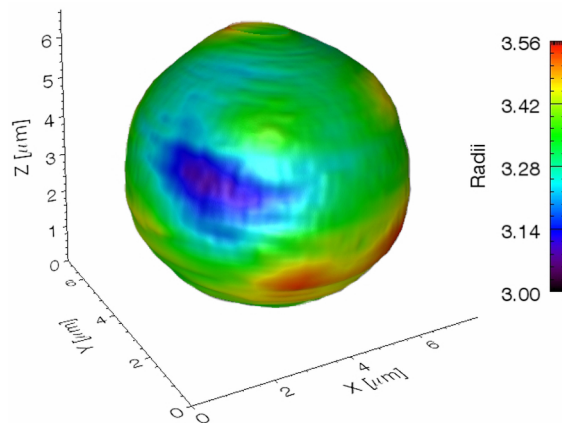


Figure 5.14: Solid-liquid interface of an Al-82 wt.% Zn equilibrium shape droplet. The color scheme represents the relative distance to the center of mass of the droplet. Images courtesy of Dr. J.L. Fife.

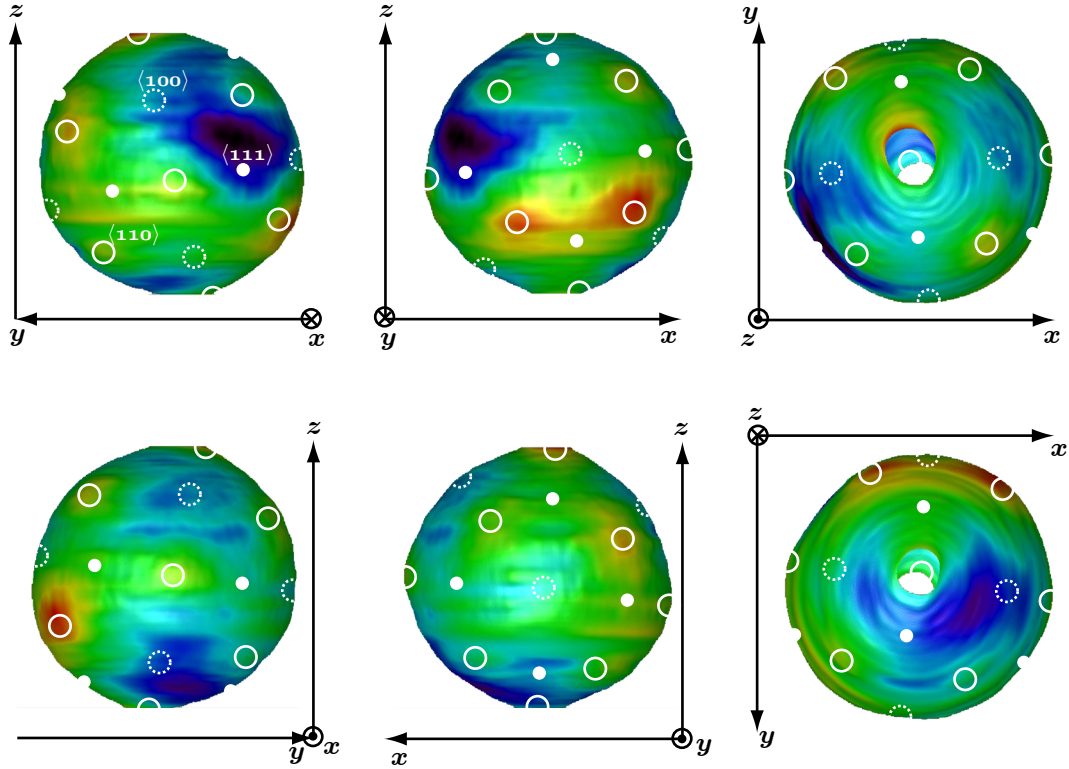


Figure 5.15: Projections of the droplet of Figure 5.14 along six different directions allowing to identify the convexities and to associate them with the appropriate crystallographic directions. $\langle 111 \rangle$, $\langle 110 \rangle$ and $\langle 100 \rangle$ directions are represented by filled, empty and dashed white circles respectively. Images courtesy of Dr. J.L. Fife.

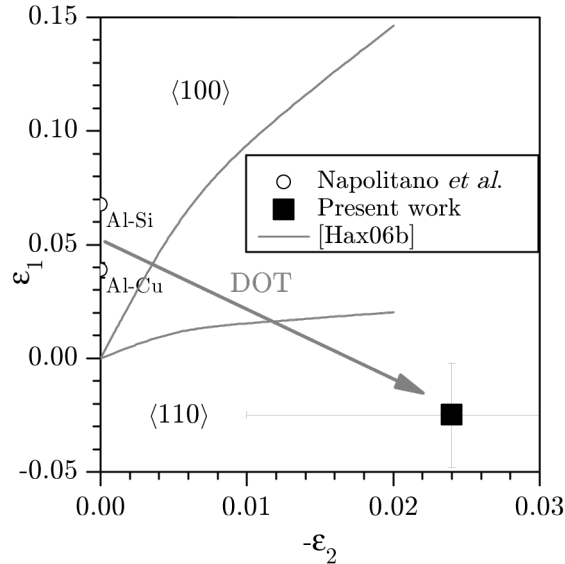


Figure 5.16: Anisotropy parameters space showing the values obtained experimentally for dilute alloys by Napolitano *et al.* [Liu01, Nap02] and for Al-82 wt.% Zn in this work. The arrow suggests the simplest path that the dendrite orientation transition could take in this parameter space.

orientation of the thin annulus around the droplet by TEM diffraction. Yet, this finding already shows a possible path for the DOT in the anisotropy parameters space (see Figure 5.16). From the values obtained by Napolitano *et al.* [Liu01, Nap02] in dilute alloys ($\varepsilon_1 \approx 0.05, \varepsilon_2 = 0.0$) to the point found here, the DOT crosses the hyperbranched domain in a region where the magnitude of the anisotropy is very low, a situation favorable to the appearance of seaweeds as the next chapter will show.

5.2.2 Zinc Phase Equilibrium Shape

Even though measuring the equilibrium shape on the hypoeutectic side of the Al-Zn system was very difficult, one measurement was also performed in the hypereutectic part of the phase diagram with the goal to determine the zinc equilibrium shape. Zinc presents the advantage to be much more anisotropic, leading to much shorter equilibration times and thus a larger density of small droplets (Figure 5.17 (a)). In this case an Zn-1 wt.% Al alloy was equilibrated at 396.7 °C for 72 h. Figure 5.17 (b) shows that due to the strong anisotropy, the equilibrium shape is lenticular and squeezed along the $\langle 0001 \rangle$ direction.

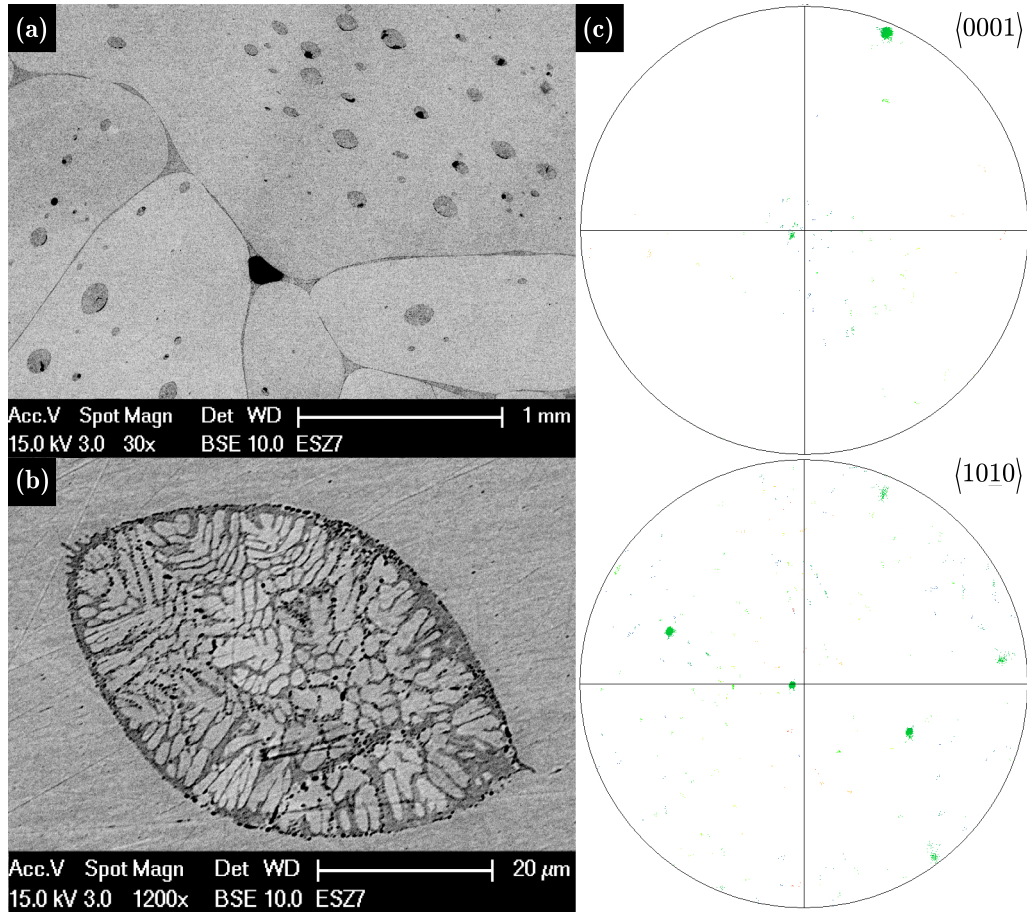


Figure 5.17: (a) Zn-1 wt.% Al sample equilibrated for 72 h at 396.7 °C, showing differently oriented grains containing well-aligned quenched equilibrium shapes. (b) Detailed view of one quenched droplet of the upper right grain in (a). (c) $\langle 0001 \rangle$ and $\langle 10\bar{1}0 \rangle$ pole figures of the matrix around the lens in (b), showing that the lens is squeezed along the $\langle 0001 \rangle$ direction.

Due to the high density of the alloy, only a very small (300 μm) tomography sample could be scanned at high energy on the synchrotron line of SLS. Furthermore, the composition difference between the matrix and the quenched liquid is only a few percent, leading

to a fairly low contrast. Nevertheless, the aspect ratio of the lenses could be confirmed to be 1.6, a value also found by manual serial sectioning. Passerone *et al.* [Pas82] found similar values in Zn-Sn, Zn-In, Zn-Pb and Zn-Bi alloys. They extrapolated an aspect ratio of 1.3 for pure zinc at its melting point. A decrease in temperature, as well as the adsorption of alloying elements at the interface to a higher extent, usually increase the anisotropy and ultimately produce facets [Cha08]. The aspect ratio of the equilibrium shapes in Zn-In and Zn-Sn was shown to increase from 1.3 at the melting point of zinc (419.58 °C) to 2 at 170 °C [Pas80a, Pas80b]. This trend thus confirms that a higher equilibration temperature lowers the aspect ratio. Finally, Miller and Chadwich [Mil69a] found an aspect ratio of 2.1 for a Zn-1.4 wt%Al alloy equilibrated at 385 °C. The value obtained in this work thus shows good agreement with previous findings and was already used for the simulation of growth and nucleation of zinc in galvanized coatings [Mar10a].

Earlier investigations [Mil69b] further showed no sign of 6-fold anisotropy within the $\{0001\}$ plane, while zinc dendrite still have an unambiguous tendency to grow along $\langle 10\bar{1}0 \rangle$ [Rhe08]. This aspect was thus also investigated. The result of a cut in the basal plane of the same sample as above is shown in Figure 5.18. Since this was not the main interest of this work, only optical imaging was used to examine individual equilibrium shapes⁷. Serial sectioning allowed to capture the maximum diameter disc (*i.e.* the basal plane) of 14 droplets and as they were all embedded in a single grain, their shape could be averaged to minimize measurement errors. The relative variation of the diameter between the $\langle 10\bar{1}0 \rangle$ and $\langle 1\bar{2}10 \rangle$ directions (determined by EBSD, Figure 5.18 (c)) was found to be $-2.2 \pm 2\%$. Firstly, the error is of the same order of magnitude as the measurement and must be attributed to the insufficient contrast at the interface generated by the chemical etching. Secondly, the result still presents a negative contribution which would predict a maximum of the ξ -plot along $\langle 1\bar{2}10 \rangle$ whereas the opposite should be the case given the observed growth directions.

Nonetheless, Figure 5.17 (b) shows two additional informations. First, as for the hypoeutectic case, the contrast at the interface is not marked with a thin layer delineating the solid liquid interface. Second, evidences of epitaxial inward growth at the edge of the lens (upper left corner in Figure 5.17 (b)) show that the quench is not quite efficient enough to preserve the original solid liquid interface at that critical location⁸. Consequently, $\langle 10\bar{1}0 \rangle$ being the fastest growth directions, these dendrites growing inward during quench perturb the original equilibrium shape. In-situ high temperature tomography would avoid this quenching artifact and could give more precise measurements if the resolution allows it. Thus, the basal in-plane anisotropy of zinc alloys remains for now inaccessible through experiments or too low to be measured.

⁷Note that in the tomography scans, in addition to the poor contrast, the ratio between the pixel size of 0.37 μm and the diameter of the observed droplets 10-30 μm was not sufficient to address this question.

⁸The acute angle provides a growth advantage that the quench is unable to suppress.

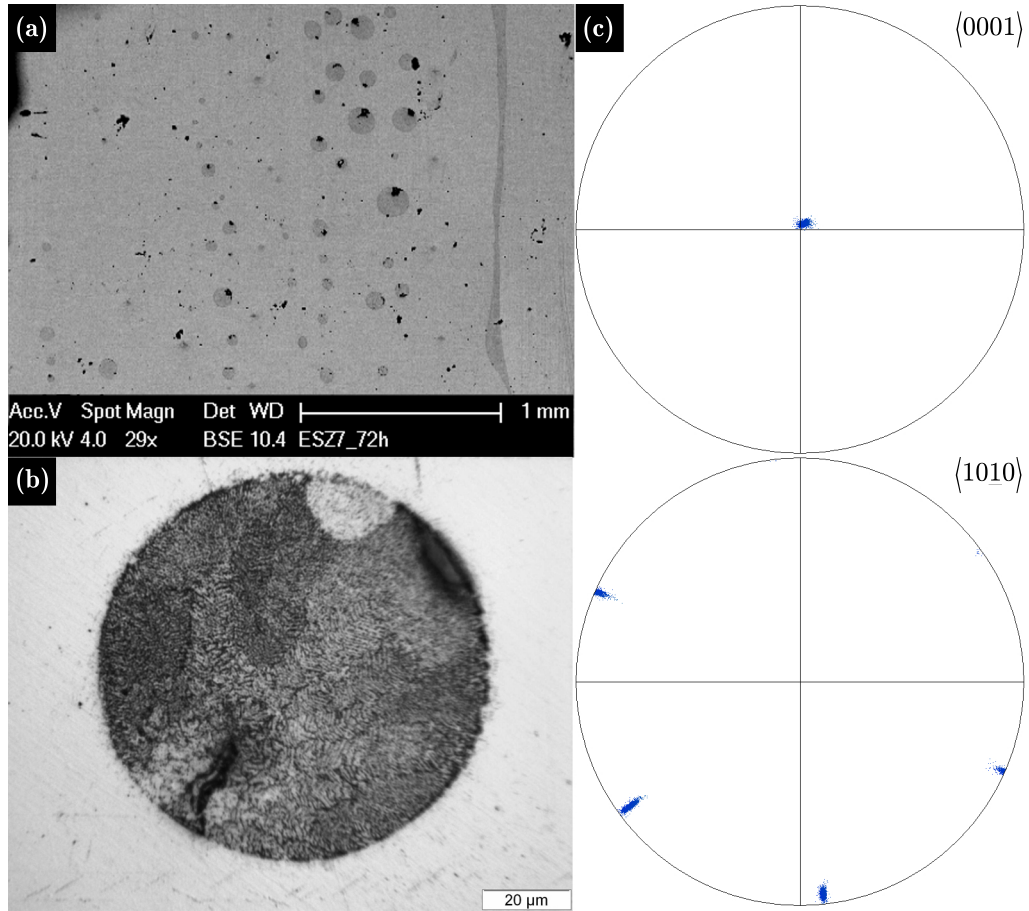


Figure 5.18: Same sample as in Figure 5.17 (a) cut in the basal plane of the upper right grain. (a) Overview of the circular shapes of the droplets. (b) Detailed optical microscopy image of a single droplet showing no visible evidence of basal in-plane anisotropy. (c) $\langle 0001 \rangle$ pole figure confirming the basal orientation of the cut and $\langle 10\bar{1}0 \rangle$ pole figure showing the directions where a maximum disk radius is expected.

Chapter 6

Growth Morphologies and Directions

In the previous chapters, the origin of the dendrite orientation transition, *i.e.*, the solid-liquid interfacial energy anisotropy, was treated in details. This chapter will focus on the observation and analysis of the resulting microstructures and morphologies. Progress made in the observation method will be addressed first, characterization of experimental results thereafter and comparison between real and modeled morphologies last.

A number of complex observations will be described in this chapter, and a short summary of the findings presented hereafter is given now to help guide the reader. X-ray tomography of quenched Bridgman samples enables the clear identification of microstructural features not observable before with other techniques. In Al-Zn alloys with compositions either below 25 wt.% Zn or above 55 wt.% Zn, the tomography observations agree with the DOT analysis presented by Gonzales and Rappaz [Gon06]. At intermediate compositions, between 25% and 55% Zn, the additional information gained by the improved analysis technique reveals microstructures much more intricate than expected from the previous study by those authors. Indeed, high multiplicity $\langle 320 \rangle$ dendrites, having 24 growth directions rather than the usual 6 $\langle 100 \rangle$ or 12 $\langle 110 \rangle$ growth directions, were not observed. Rather than one high multiplicity trunk growing in a steady direction, we found that the microstructure is composed of trunks alternating in growth directions around the orientation given by the $\langle 320 \rangle$ texture.

Finally, we present phase-field simulations of equiaxed and directional solidification that illustrate the competition between $\langle 100 \rangle$ and $\langle 110 \rangle$ growth characteristics which are thought to be responsible for the alternating growth mechanism. They will also give a clearer insight into the selection mechanism, and show that the measurement of an overall texture can be deceptive for the prediction of dendrite growth directions when such an alternating growth mechanism is present.

6.1 Improvement in the Analysis Method

The major difficulties in the interpretation of complex microstructures such as $\langle 320 \rangle$ dendrites or seaweeds in opaque metallic alloys come from the drawbacks of the analysis method itself. Until recently with the advent of X-ray tomography and further with *in situ* radiography [Mat99, Mat05] and tomography [Lud05, Sal06], samples were examined with post-mortem 2D sections and this presents several problems. Applied to the present case, those are:

- Metallographic sections, even if prepared in the desired crystallographic orientation,

might actually not be at a desired depth in the sample, for example in the middle of a primary trunk.

- The issue is that even if a trunk seems continuous, coalescence merges secondary arms together making them indistinguishable from primary trunks.
- Furthermore, arms are not always attached to the trunk in a section and could falsely be thought to run in or very close to the section. Especially with high multiplicity dendrites such as $\langle 320 \rangle$, very small variations in angle make big differences in the interpretation. This and the previous point make any interpretation of secondary arms orientation ambiguous, since they might actually not lie in the plane under consideration.
- Primary solid is delicate to reveal by etching because of coarsening, backdiffusion, and solid state transformation (in the present case, spinodal decomposition). This problem is even more acute at low solute concentration in system with a large solubility in the primary phase. Solid fraction evolves very rapidly near the liquidus, but temperature remains high and backdiffusion is important, thus smearing the solid-liquid interface.
- A section taken far from the solidification front misses information about the dendrite tip shape and the very beginning of its evolution, where the most dramatic changes in the microstructure occur.

Figure 6.1 shows that the good phase separation generated by the quench in the Bridgman solidification procedure solves the problem of contrast in both tomography and metallographic observations (see Figure 3.6). The fact that this method avoids most of the backdiffusion, at least in the upper part of the dendritic growth, greatly simplifies both etching procedures and interpretation of the observed morphologies. As coarsening and coalescence is avoided through the limited stay at high temperature, an unambiguous distinction of microstructural components such as grains, trunks and arms can be made.

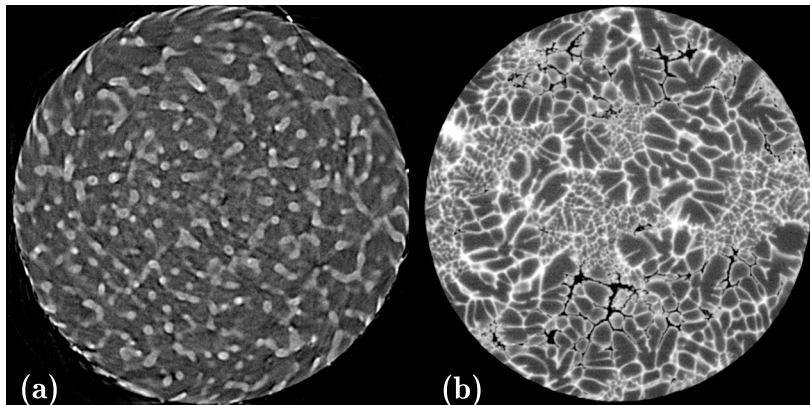


Figure 6.1: Transverse section of two 600 μm diameter Al-55 wt.% Zn tomography samples grown at 4 mm/min. (a) without and (b) with quench, respectively. The clockward spiral shaped corona at the very edge of sample (a) originates from the machining of the column. This artifact was eliminated in subsequent samples by more careful machining, and is totally avoided in (b).

The method used in this work greatly enhances the quality and quantity of information that can be extracted from quenched Bridgman type experiments. It gives access to the

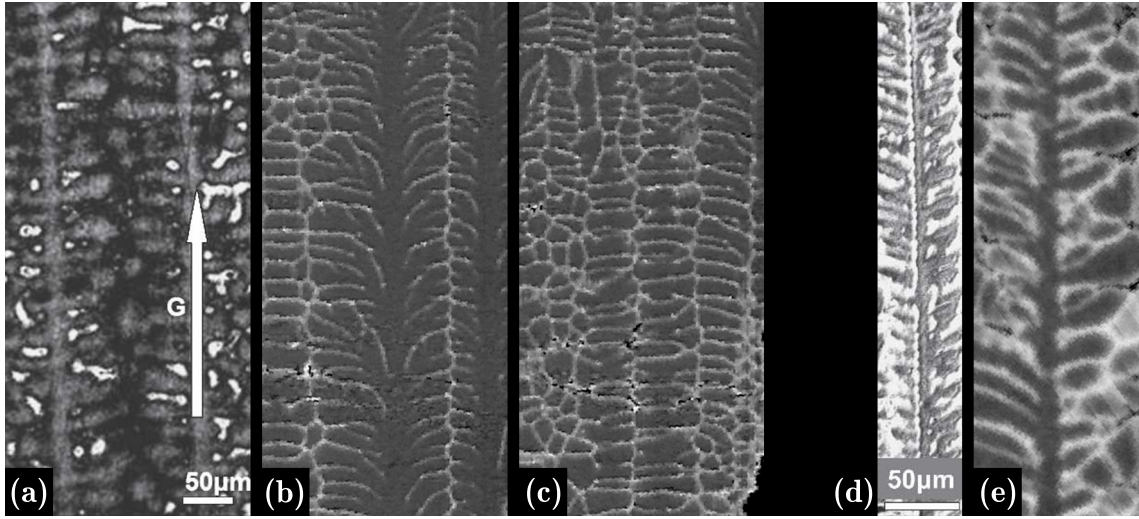


Figure 6.2: Bridgman solidified Al-10 wt.% Zn (a,b,c) and Al-50 wt.% Zn (d,e) samples. (a) Metallographic section in a (100) plane with secondary arms seen at 90° from the trunk [Gon06]. (b) (100) section cutting a trunk in an X-ray tomography dataset from a quenched sample exhibiting a much more precise view of the secondary arms. (c) Section parallel to (b) but separated by $85\mu\text{m}$, showing distinct secondary arms perpendicular to the primary growth direction. (d) Reported $\langle 320 \rangle$ dendrites [Gon06] showing a trunk and very irregular secondary arms. (e) Cut on the X-ray tomography stack with an orientation identical to (d) through a trunk in a (001) plane showing arms that actually grow out of plane. Note that the magnification is identical (a), (b) and (c), and (d) and (e), respectively, but does not exactly match between (a,b,c) and (d,e).

morphology of the dendrite or seaweed tips and the contrast between phases is sufficient even when the liquid and solid concentrations are very close, *i.e.*, at low solute concentrations (see Figure 6.2). Finally, access to the complete 3D morphology is obtained, thus allowing one to select precisely the observation plane and to identify the morphological features. Two examples of the improvement in interpretation are shown in Figure 6.2. In dilute Al-10 wt.% Zn, the secondary arms were believed to grow at an angle of 90° with respect to the trunk (Figure 6.2 (a) [Gon06]). However, Figure 6.2 (b) reveals that when cutting exactly through the trunk, the situation is different and secondary arms grow with a smaller angle with respect to the trunk. A second section (Figure 6.2 (c)), slightly shifted but parallel to the previous one reveals secondary arms at 90° , similar to those seen after solidification in Figure 6.2 (a). In the case of the high multiplicity $\langle 320 \rangle$ dendrite morphology reported by Gonzales and Rappaz [Gon06] (Figure 6.2 (d)), the comparison with the tomography data of Figure 6.2(e) shows that the irregularity in the secondary arms comes from out-of-plane growth suggesting an even more complex growth mechanism than previously expected. This subject will be covered in more details in the next section.

These salient features allowed the reexamination of the DOT in Al-Zn, which is presented hereafter.

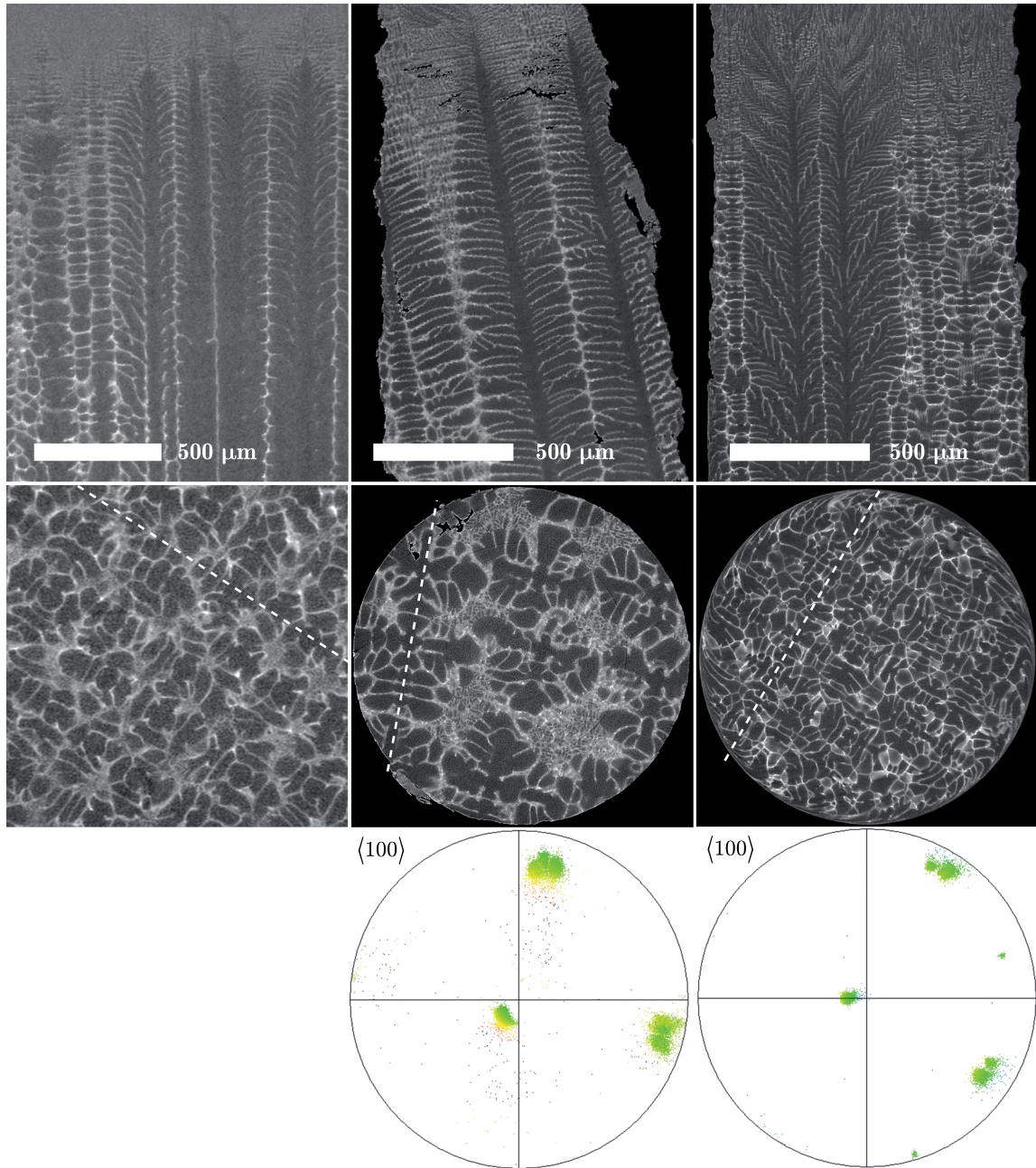


Figure 6.3: Longitudinal (top) and transverse (center) cuts through the X-ray tomography stack and pole figure (bottom) associated with the transverse cut when it was available. Al-5 wt.% Zn (left), Al-10 wt.% Zn (middle) and Al-20 wt.% Zn, solidified at 4, 4 and 10 mm/min respectively. The trace of the longitudinal section is shown by a dashed white line on the transverse cut. Note that whereas the length scale is the same for longitudinal and transverse sections of each alloy, the magnification varies slightly from one alloy to another.

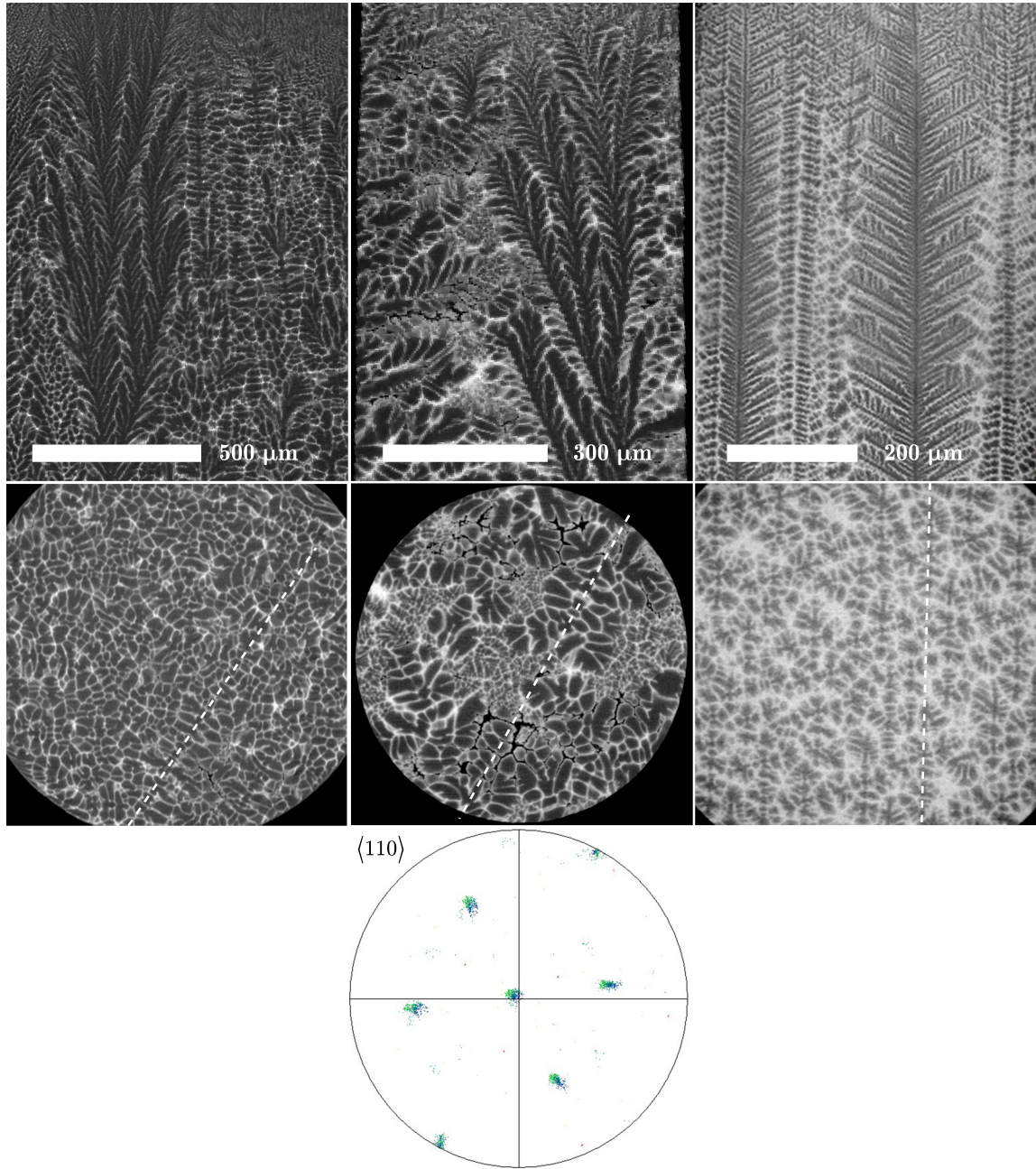


Figure 6.4: Longitudinal (top) and transverse (center) cuts through the X-ray tomography stack and pole figure (bottom) associated with the transverse cut when it was available. Al-35 wt.% Zn (left), Al-55 wt.% Zn (middle) and Al-82 wt.% Zn, solidified at 10, 4 and 10 mm/min, respectively. The trace of the longitudinal section is shown by a dashed white line on the transverse cut. Note that whereas the length scale is the same for longitudinal and transverse sections of each alloy, the magnification varies from one alloy to another. EBSD was performed on an Al-35 wt.% Zn sample solidified at lower velocity and showed a texture matching the results by Gonzales and Rappaz [Gon06], however the structure was too coarse and the sample too small to show a characteristic microstructure and a faster growth sample is therefore presented here. The primary and secondary arms growth directions in Al-82 wt.% Zn and higher alloy concentrations were unambiguous enough that no EBSD measurements were necessary. Furthermore, the results by Gonzales and Rappaz for those compositions were already clearly assessing the $\langle 110 \rangle$ growth direction of dendrite trunks and arms.

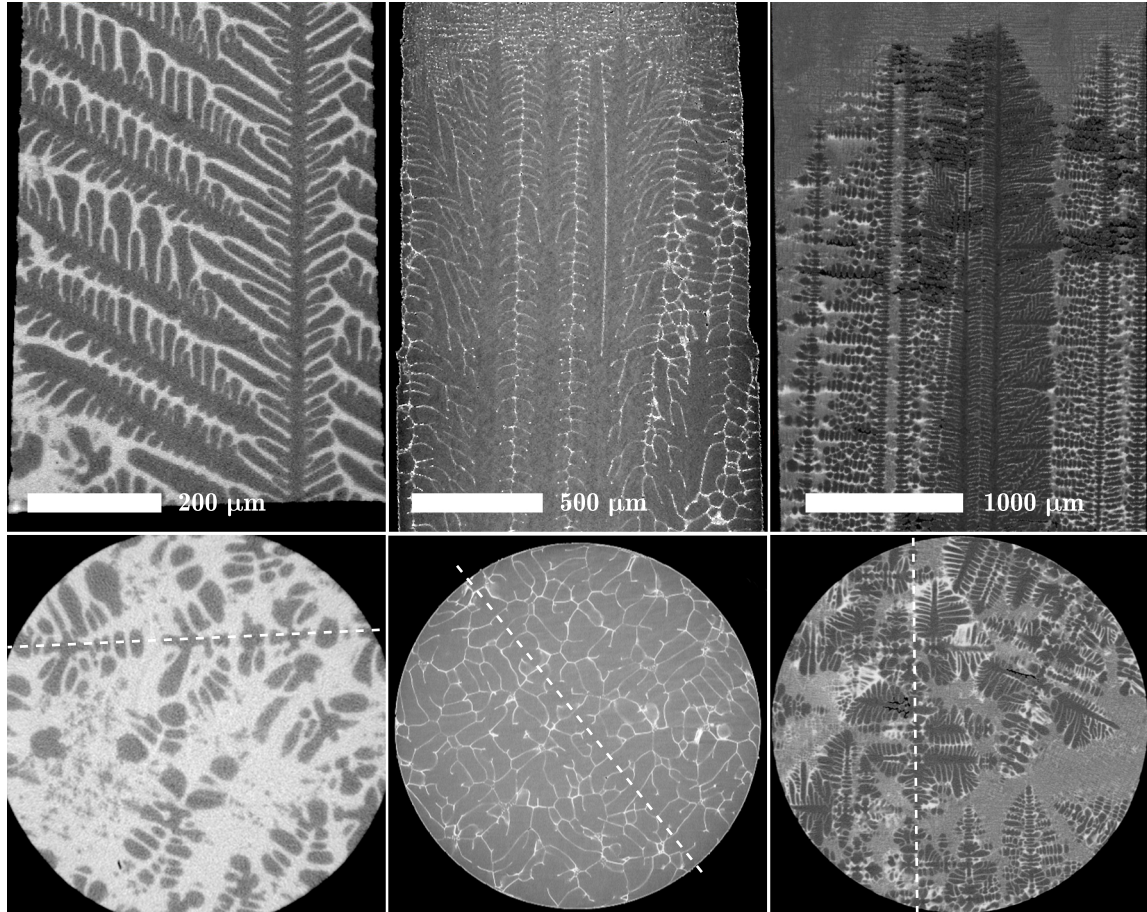


Figure 6.5: Longitudinal (top) and transverse (bottom) cuts through the X-ray tomography stack. Al-90 wt.% Zn (left), Al-4 wt.% Cu (middle) and Al-15 wt.% Cu, all solidified at 4 mm/min. The trace of the longitudinal section is shown by a dashed white line on the transverse cut. Note that whereas the length scale is the same for longitudinal and transverse sections of each alloy, the magnification varies slightly from one alloy to another. The Al-90 wt.% Zn sample does not show the tip of the dendrite because at such high zinc concentration, a sample only 600 μm in diameter does not necessarily contain a trunk. In this case the trunk is close to the edge of the sample, but with a small angle with respect to the axis of the column. Thus, the trunk is out of the sample at the height of its tip and a section deeper in the mushy zone is shown.

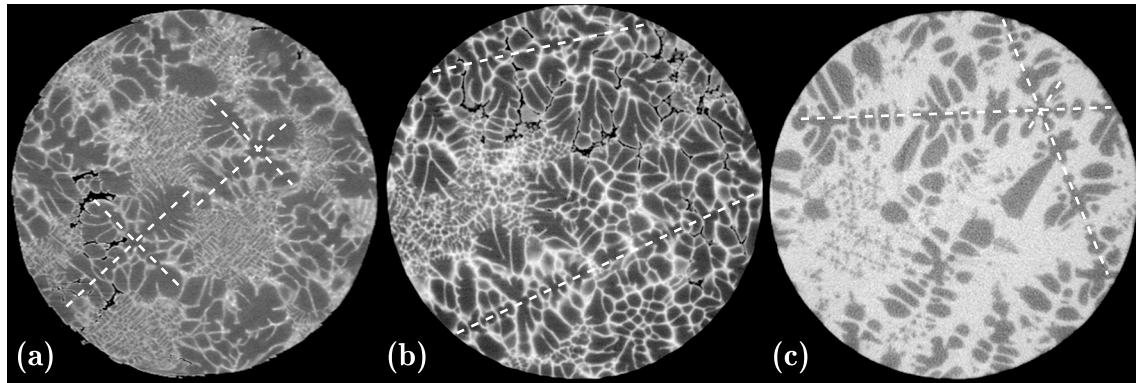


Figure 6.6: X-ray tomography transverse sections of (a) Al-10 wt.% Zn (\varnothing 1200 μm), (b) Al-50 wt.% Zn (\varnothing 600 μm) and (c) Al-90 wt.% Zn (\varnothing 600 μm), all grown at 4 mm/min. The dotted lines show the symmetry planes in which the secondary arms lay. The magnifications are given by the diameters of the sections since they each represent the whole sample.

6.2 Microstructural Study of Bridgman Solidified Al-Zn and Al-Cu Alloys

X-ray tomography was performed on Al-Zn alloys from 5 to 90 wt.% zinc and Al-4 and 15 wt.% Cu. Figures 6.3, 6.4 and 6.5 show longitudinal and transverse sections through the tomography stack of samples of various compositions. As the sizes of the tomography columns and microstructures vary from case to case due to X-ray absorption constraints, the magnifications are not exactly the same across the samples. Instead, they were selected to be representative of the typical microstructure observed for each composition. Al-50 wt.% Zn was deliberately omitted from Figure 6.4 since it will be extensively analyzed later on.

First of all, EBSD measurements showed an identical angular dependence of the dendrite behavior or seaweed texture as in the DOT for the whole range of Al-Zn alloys, and thereby confirm the results already obtained by Gonzales and Rappaz [Gon06, Gon08]. However, as the last section foretold, the secondary dendrite arms in low alloyed Al and the trunk and arm directions in the intermediate composition range where seaweeds are observed cannot be deduced from the DOT misorientation curve of Gonzales and Rappaz (Figure 2.5).

6.2.1 Symmetries

Three types of microstructures have been observed in Al-Zn alloys and are illustrated in Figure 6.6. Between 5 and 20 wt.% Zn, trunks with $\langle 100 \rangle$ orientation and secondary arms growing in $\{100\}$ planes are observed. In transverse sections those typically appear as crosses with a 90° angle (Figure 6.6 (a)). At zinc concentrations higher than 55 wt.% , dendrites (both trunks and arms) grow, without surprise, along well defined $\langle 110 \rangle$ directions. Indeed, in the former studies, the transformation at the eutectic temperature (381°C) provided some sort of a self-quench, making the structure to clearly appear in Figure 6.6 (c). This cut shows very well the growth advantage, and thus the larger lateral extension, that $\langle 110 \rangle$ arms at 60° from the trunk have over the shorter $\langle 110 \rangle$ arms that grow at 90° . In the range of 25 to 55 wt.% zinc, those symmetries break down and an apparently random structure is observed. Nonetheless, a careful look at a scan through

the X-ray tomography stack allows one to identify individual symmetry planes in each grain, such as the ones presented in Figure 6.6 (b).

An EBSD analysis showed that in all intermediate compositions investigated here, this symmetry plane is a $\langle 100 \rangle$ plane, as shown in the example of Figure 6.7. With respect to the previous studies by Gonzales *et al.* and previous chapters herein, this finding makes sense since the DOT operates in a $\langle 100 \rangle$ plane.

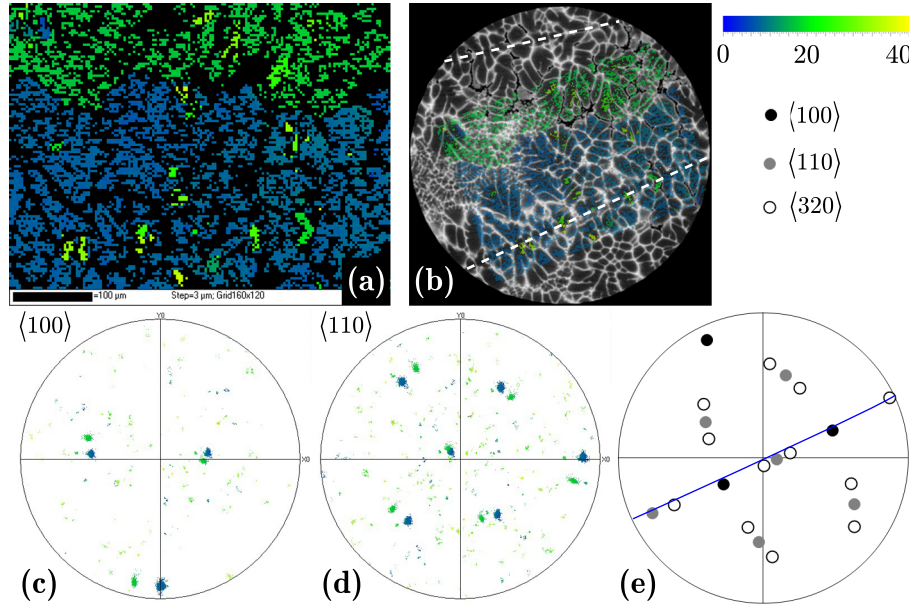


Figure 6.7: (a) EBSD map from the transverse section in Figure 6.6 (b) (Al-50 wt.% Zn). The size is 480 by 360 μm with a step of 3 μm . The color scale is the angle between $\langle 110 \rangle$ and the horizontal axis of the map. (b) Superposition of the EBSD map on the X-ray tomography transverse section. (c) and (d) are the $\langle 100 \rangle$ and $\langle 110 \rangle$ pole figures obtained from the map, respectively, showing a slight misorientation between the two grains with respect to the horizontal axis, but a common $\langle 110 \rangle$ direction perpendicular to the plane. (e) Pole figure rotated in the coordinate system of the tomography dataset, with indication of 3 directions: black circles $\langle 100 \rangle$, grey circles $\langle 110 \rangle$ and open circles $\langle 320 \rangle$. The crystallographic direction closest to the center of the pole figure, *i.e.*, the z -axis of the sample and the direction of the thermal gradient, is $\langle 320 \rangle$, hence the texture observed in Al-50 wt.% Zn by Gonzales and Rappaz [Gon06]. The pole figure also identifies that the symmetry plane of the “blue” grain in (b), shown with a white dashed line, is a $\langle 001 \rangle$ plane (shown with a blue line in the stereographic projection).

6.2.2 Primary Trunk Orientation

Low and high alloyed Al-Zn alloys exhibit primary dendrite trunks which clearly grow in well defined $\langle 100 \rangle$ and $\langle 110 \rangle$ directions, respectively. At intermediate compositions, the situation is more complex since none of these alloys produce a typical dendritic structure, and thus no trunk in the classical sense is present. Figure 6.8 shows longitudinal cuts in the symmetry (100) plane of three such alloys, which all exhibit a seaweed-type behavior. Instead of well established trunks, the growth seems to occur in an alternating tip splitting mechanism with very short arms. The structure is not random however, since certain orientations seems to be preferred in the alternating splitting process. Even if the morphology differs significantly from that of a typical dendrite, one can still identify certain features using the names used in the more commonly observed structures. We will call a feature a “trunk” if it is aligned within about 20° of the thermal gradient, and extends over a distance large enough to be clearly identifiable by a number of sidebranches. Although this definition is imprecise, the trunks in Figure 6.8 are nevertheless clear. Any smaller feature which emerges from such a trunk will be called arm.

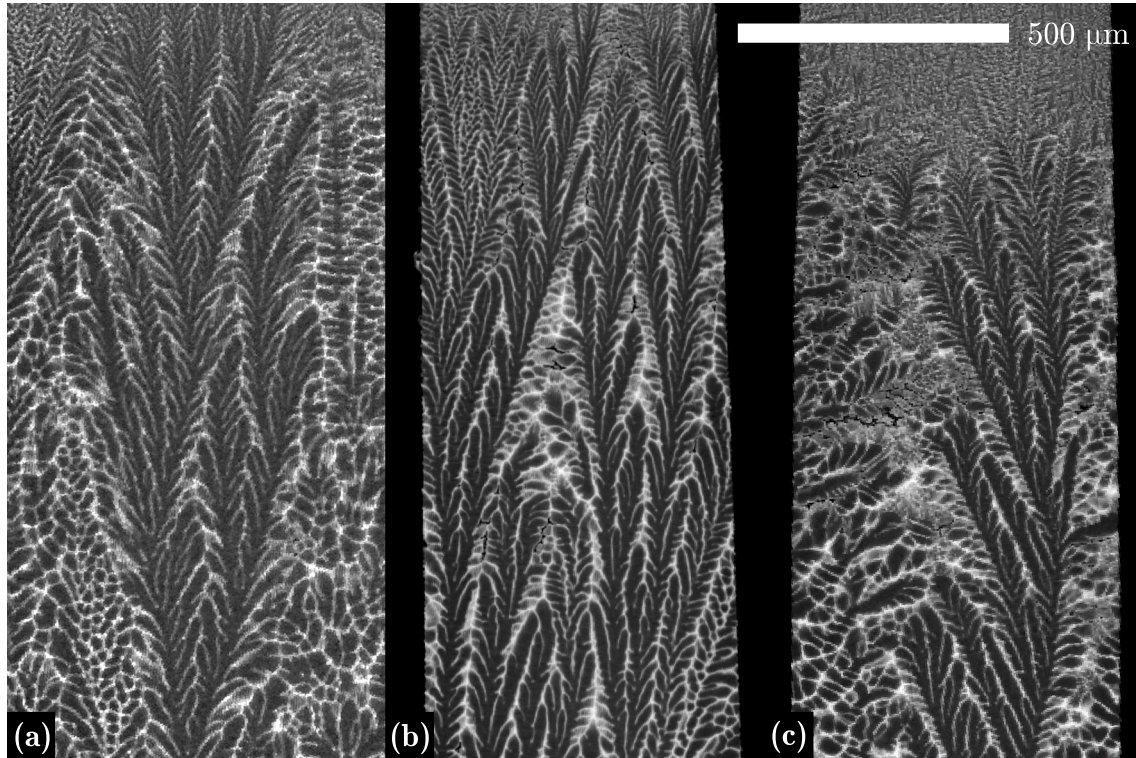


Figure 6.8: Longitudinal cuts of the X-ray tomography stack in the (100) symmetry plane of (a) Al-35 wt.% Zn, (b) Al-50 wt.% Zn and (c) Al-55 wt.% Zn.

For a meaningful assertion about those trunks to be made, a minimum number of them showing similar characteristics should be present in a cut. The sample showing (100) symmetry plane with the largest number of trunks (Al-50 wt.% Zn, Figure 6.6 (b)), was selected and examined in more detail. As shown by the solid and dashed white lines in Figure 6.9 (a), two types of trunks were observed. Those oriented close to the vertical (dashed lines, *e.g.*, B), *i.e.*, the thermal gradient direction, show secondary arms on both sides in the (100) plane, whereas those further inclined (solid lines, *e.g.*, A1) exhibit arms on only one side in that plane. Note that since the secondary arms are so short and rarely straight, their direction, even taken as the average of the angle with the trunk found at

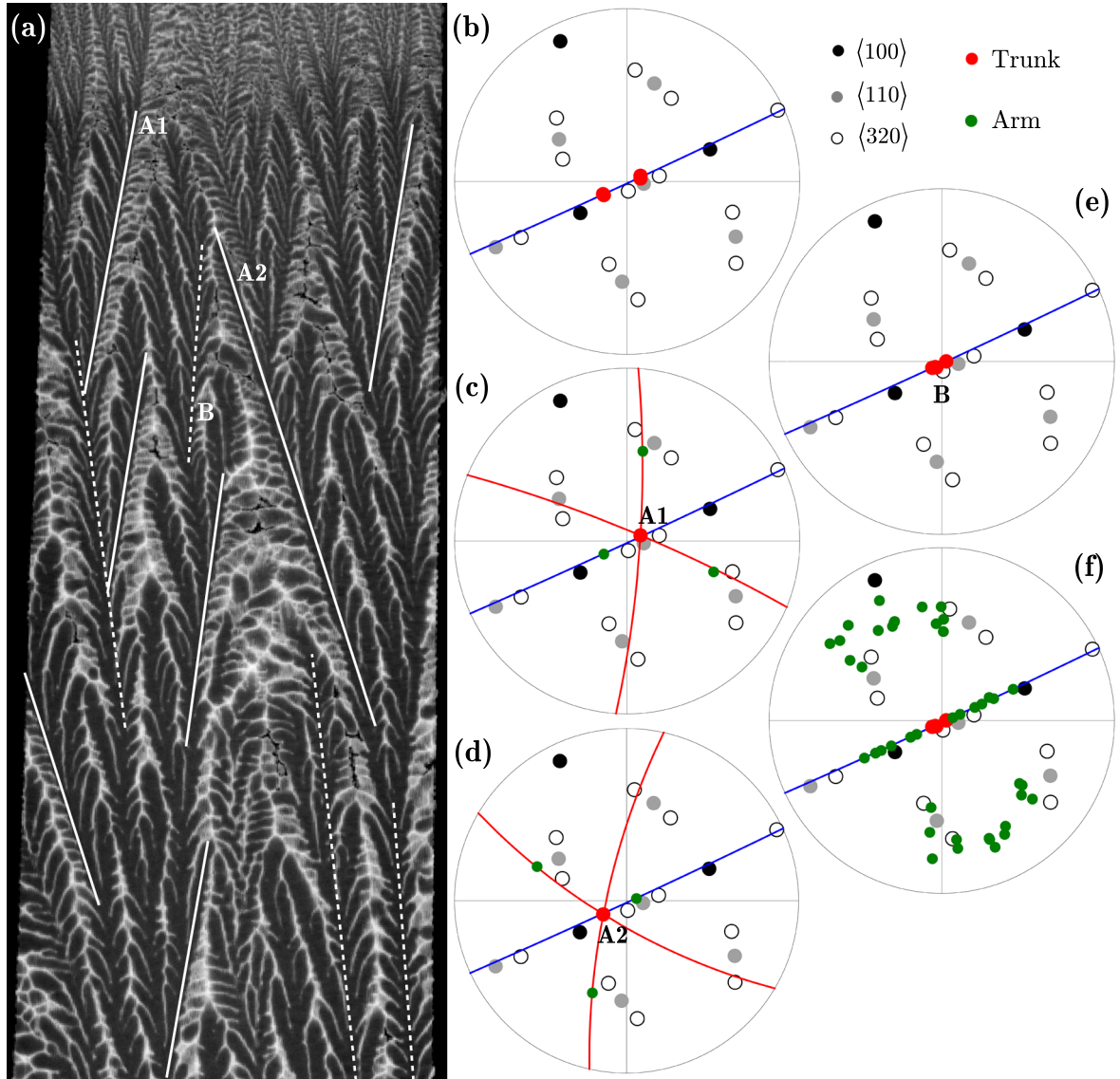


Figure 6.9: (a) $\langle 100 \rangle$ symmetry plane in Al-50 wt.% Zn, showing two types of trunks. Trunks with secondary arms on only one side in the $\langle 100 \rangle$ plane, highlighted by solid white lines, and trunks with arms on both sides identified by dashed white lines. (b)-(f) are the pole figures obtained from the EBSD map in Figure 6.7 with the $\langle 320 \rangle$ direction being the closest to the vertical, *i.e.*, the thermal gradient direction. The planes and directions found in the X-ray tomography stack are superimposed on the pole figures. The $\langle 100 \rangle$ symmetry plane is represented in blue, red and green dots represent trunks and arms, respectively. (b) shows the orientation of the A-type trunks. The configuration of the trunk, secondary arms and (red) planes in which the latter lay are shown in (c) and (d) for trunk A1 and A2, respectively. (e) shows the orientation of the B-type trunks, close to the $\langle 320 \rangle$ direction. (f) shows the directions of the secondary arms associated to the B-type trunks.

their root, is subject to large errors. However, the different characteristics observed for type A and B trunks remain valid. Figure 6.9 (e) shows that the latter grow within a few degrees from the $\langle 320 \rangle$ direction whilst the former are much more regularly oriented in two directions at $\sim 14^\circ$ with respect to $\langle 320 \rangle$ (Figure 6.9 (b)).

Once examined out of this plane, the secondary arms emerging from type A trunks are found in two other planes outlined by the two red plane traces in the corresponding stereographic projections. Figure 6.9 (c) and (d) illustrate this configuration for the trunks A1 and A2. The orientation of these arms in the out-of-plane sections is so ill-defined that it is not possible to identify them with a crystallographic direction with any precision. The in-plane secondary arms orientation on the other hand, correspond to the direction of the trunks laying on the other side of the $\langle 320 \rangle$ direction, *i.e.*, the in-plane arms of trunk A1 points in the same direction as the trunk A2 and vice-versa. This probably explains why over long distances, a zigzag of the trunks is observed. As such a trunk encounters a perturbation (*e.g.*, the solute field from an other trunk or thermal fluctuations), it might switch sides and take the alternate direction.

The observation of B type trunks shows a very different configuration. The scatter of the directions in Figure 6.9 (f) shows that their secondary arms do not seem to have a preferred growth direction. The potential resulting growth disadvantage could very well explain their short lateral extension compared to the type A configuration.

As the segmentation of such complex and intricate structures cannot be automated, the isolation of one single trunk is hardly accessible and does for now impede a deeper stereological analysis. Furthermore, this is a static post-mortem observation of a highly dynamic process and *in situ* investigations could certainly improve the understanding of this growth morphology.

These observations in Al-50 wt.% Zn show that the measurement of the texture of such a sample can be deceptive. Indeed, although the mean growth direction, *i.e.*, the texture is $\langle 320 \rangle$, by far not all actual growth directions correspond to this orientation as evidenced by A type trunks. A detailed analysis combining X-ray tomography of quenched sample and EBSD measurement, like the one presented here, should be performed on more intermediate, seaweed generating, compositions. Such an analysis would provide more information about the relation between alternating growth direction and the overall textured growth.

6.2.3 Secondary Arm Bending

The case of seaweeds, but also the low zinc content alloys, showed that secondary arms have a tendency to bend away from the trunk during growth. This observation is counter-intuitive because normally in most alloys, such as succinonitrile-acetone, the arms tend to turn towards the thermal gradient as they grow away from the trunk or they remain orthogonal to the trunks when the anisotropy is large, such as for Ni-base superalloys. To rule out the possibility that this could be due to a kinetic effect, Figures 6.10 (a) to (c) show that the situation does not change with growth velocities.

One possible explanation is that the anisotropy and composition being strongly linked, as seen for the trunks, the arms would bend as a result of the composition increase with the depth in the mushy zone. If the anisotropy and composition are linked, then this also changes the composition of the solid formed on the arm and hence the anisotropy. This could explain the evolving preferred growth direction observed. No additional simulations have yet been performed to examine this hypothesis, since a model coupling concentration

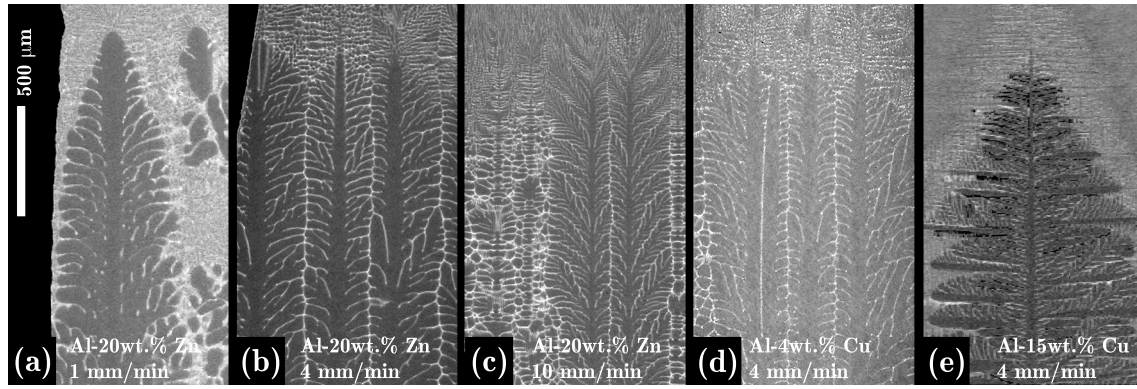


Figure 6.10: Tomography sections ($\langle 100 \rangle$ plane) through dendrite trunks of 5 specimens. (b) Sample courtesy of G. Kurtuldu [Kur11].

and anisotropy would be necessary. It should be noted that in some Al alloys solidified under high thermal gradient, even the primary trunks were observed to bend by Henry *et al.* [Hen98b], which could be another manifestation of the same phenomenon. However, given the DOT of the trunks, this explanation does not stand since the phenomenon should be the opposite of what is observed (Figure 6.3) for low solute Al-Zn alloys, with arms bending from $\langle 100 \rangle$ at low zinc content to $\langle 110 \rangle$ when the zinc content increases.

From an experimental point of view, this phenomenon is hard to quantify precisely in low alloyed Al-Zn, because the solid fraction evolves rapidly with temperature, leading to short secondary arms, the growth direction of which is difficult to determine. Moreover, secondary arms not only bend, but also have a tendency to split, appearing like a palm-tree, a behavior which is typical for the seaweeds encountered in intermediate compositions.

For an Al-20 wt.% Zn, nominal composition, the hypothesis given above implies that the composition of the primary phase in the secondary dendrite arms ($k_0 c_\ell$) would have to increase by about 5 wt.% to enter the region where seaweeds are formed. Indeed, the top scale in Figure 2.5 shows that a transition from 10% solute in the primary solid phase to a 15% seaweed forming concentration, represents a change in the liquid concentration from ~ 20 wt.% to ~ 30 wt.% (bottom scale), an enrichment that seems possible by microsegregation behind the dendrite tip. Pushing this conjecture even further, a secondary arm should thus start growing along $\langle 100 \rangle$ and ultimately grow at 45° from the trunk, *i.e.*, along $\langle 110 \rangle$. Experimentally, this is definitely not observed as shown in Figure 6.10 (a)-(c) where the tendency is actually just the opposite.

However, one should also remember that the shape of a secondary arm is given not only by its growth direction, but also by the asymmetry in growth as solidification progresses. Indeed, the solute and temperature profiles seen by an arm differ between the upwind and downwind directions with respect to the growth direction, especially in columnar growth. The solute concentration in the liquid above the arm is usually lower than below it due to the rejection of denser solute in the mushy zone. Moreover, the thermal gradient ahead of the arm is positive whereas it is negative behind it, leading to asymmetric growth. A post mortem analysis like the present one does not allow one to clearly separate these phenomena. *In situ* measurements would be necessary to clarify the mechanisms.

For the purpose of comparison, Al-Cu alloys were also analyzed (Figure 6.10 (d) and (e)). Astonishingly, even when the weak anisotropy of aluminum is reinforced by another fcc element, the secondary dendrite arms of Al-4 wt.% Cu show the same type of behavior

as in low solute content Al-Zn alloys. A fourfold symmetry around a $\langle 100 \rangle$ trunk with secondary arms growing in $\{100\}$ planes is observed and arms have angles with respect to the trunk between 45° and 70° at their root, then bend and split further away from the trunk. In a higher copper content alloy of 15 wt.% , secondary arms grow perpendicular to the trunk, as would be expected for a cubic solute element such as copper which reinforces the weak anisotropy of Al. However, at the very root of the arms, the take-off angle is still slightly smaller than 90° . Thus, even though the situation is clearer since the higher copper content¹ gives more time for the secondary arms to grow, there is still no model that satisfactorily explains these observations.

It appears that aluminum has an inherent character to form $\langle 100 \rangle$ trunks with off-crystallographic axis secondary arms, and only a sufficient addition of solute element allows them to stabilize them in a given direction, $\langle 100 \rangle$ for copper and $\langle 110 \rangle$ for zinc, the latter with an associate change of the primary trunk direction.

Finally, another possible explanation for these observations could be that at low anisotropy, secondary arms start to emerge close to the dendrite tip. For example, in low anisotropy succinonitrile (SCN), secondary arms emerge about $2R_{tip}$ behind the tip whereas that distance is approximately $7R_{tip}$ in pivalic acid (PVA) which has an anisotropy one order of magnitude higher than SCN [Gli89]. At low anisotropy, the arms thus emerge where the iso-concentration lines form a large angle with respect to the primary trunk direction. Since growth is fastest along the highest solute gradient, arms might thus start to grow perpendicular to the iso-concentrations and continue to do so as long as the contribution from this gradient is dominant. Further away from the tip and deeper in the mushy zone, the anisotropy contribution takes over and the arms bend. The interdendritic liquid surrounding the secondary arms in an Al-20 wt.% Zn alloy reaches the composition range where seaweed structures are observed for primary growth, and indeed one observes alternating growth directions of the secondary arms in this alloy. For Al-4 wt.% Cu, anisotropy might still be too weak to constrain the growth of the arm², whereas in Al-15 wt.% Cu the arms start perpendicular to the iso-concentration contours, but later follow the $\langle 100 \rangle$ direction imposed by the higher anisotropy due to their richer copper composition. This would also explain why nickel secondary arms grow only orthogonal to the trunks first, they emerge later due to the strong anisotropy sharpening and stabilizing the tip. Thus, when they emerge, the solute concentration gradient is already almost perpendicular to the trunk. One should also note that in these alloys, anisotropy furthermore constrains the arms along $\langle 100 \rangle$.

6.3 Phase-field simulations

With all the experimental evidence gained in the beginning of this chapter and the still open questions about the growth mechanisms that triggers the DOT, comparison to findings from phase-field calculations in this section will help to shed some more light on the problem.

¹in a system with lower solubility and partition coefficient and a higher liquidus slope than Al-Zn

²as it is probably the case for Al-5 and 10 wt.% Zn

6.3.1 Equiaxed Growth

To observe the dendrite orientation transition as Haxihmali *et al.* [Hax06b] did for a pure material, four line scans (LS) were performed in the anisotropy parameter space $(\varepsilon_1, \varepsilon_2)$. Since all experimental and MD data (see Figure 2.3) seems to show that these parameters are in the range $0 \leq \varepsilon_1 \leq 0.12$ and $-0.01 \leq \varepsilon_2 \leq 0$, the $(\varepsilon_1, \varepsilon_2)$ couples were chosen as indicated by Figure 6.11. No simulations were performed with anisotropy parameters found by the equilibrium shape measurement from the previous chapter. Indeed, at values of $\varepsilon_1 < 0$, the $\langle 110 \rangle$ character of dendrites is simply expressed more strongly, but no change in the dendrite orientation is expected. Thus the line scans are only performed in parameter space region where the DOT is expected.

All line scan simulations were performed with $\Delta x/W_0 = 1$, $\Omega = 0.4$ and $\varepsilon_{4\text{cor}} = -0.0275$ for 6000 time steps ($\Delta t = 0.1\tau_0$), *i.e.*, approximately 27.6 ms, in a box $512 \times 512 \times 512$ units of Δx in size, generating an adaptive mesh with up to 1×10^6 nodes for the most complex structures. It should be recalled that all the calculations are carried out with the material properties of an Al-10 wt.% Zn, listed in Table 4.2.

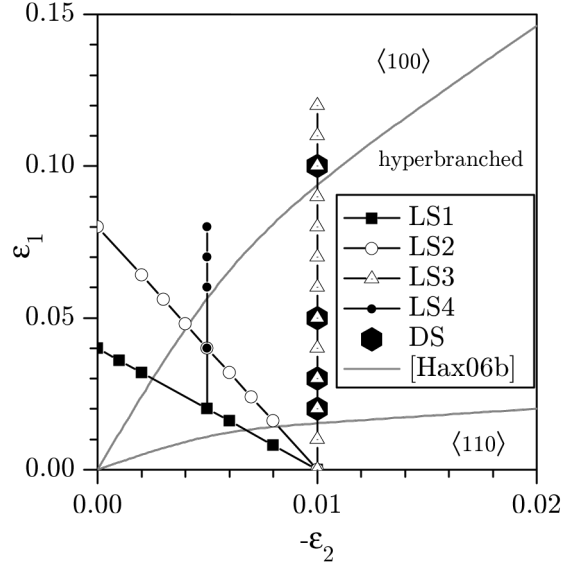


Figure 6.11: Line scans (LS) in the $(\varepsilon_1, \varepsilon_2)$ space parameter where equiaxed growth simulations were performed with the FE phase-field model. Selected $(\varepsilon_1, \varepsilon_2)$ parameters used in the direction solidification (DS) calculations. The solid gray lines show the stability limits between $\langle 100 \rangle$, hyperbranched and $\langle 110 \rangle$ dendrites found by Haxhimali *et al.* [Hax06b].

The results obtained are summarized in Figure 6.12. The first finding is that the domain of existence of $\langle 100 \rangle$ dendrites was shifted to higher values of ε_1 , whereas the boundary to $\langle 110 \rangle$ growth has not moved in comparison with those found by Haxhimali *et al.* [Hax06b]. Such a difference is however not unexpected since these authors studied a pure system and thermal dendrites whilst this work focuses on alloys and solutal dendrites.

Although one might be tempted to find a continuous transition of the growth orientation, the modeling results shows another trend. Indeed, when the $\langle 100 \rangle$ -hyperbranched limit is crossed from above, the growth direction does not tilt away from the original $\langle 100 \rangle$. The tip rather splits with a fourfold symmetry (quadruplon) around that direction and the four resulting tips grow parallel to $\langle 100 \rangle$. As ε_1 is lowered at fixed ε_2 , the center of the $\langle 100 \rangle$ direction recedes compared to the surroundings tips. Similarly, when the $\langle 110 \rangle$ -hyperbranched boundary is crossed from below, the $\langle 110 \rangle$ tip splits, but in a

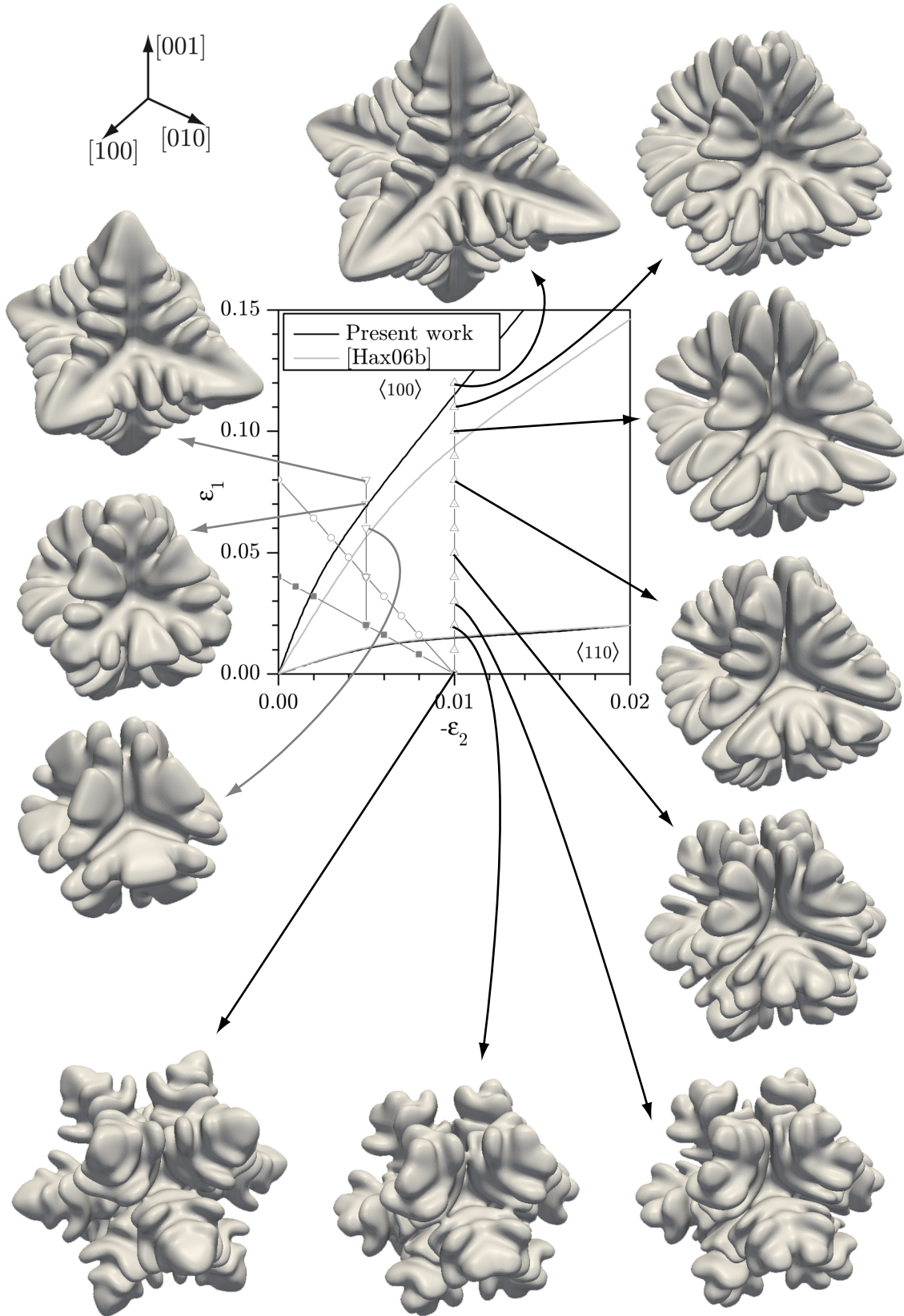


Figure 6.12: Equiaxed growth phase-field results for varying anisotropy parameters. The scale and orientation of all dendrites is identical. The solid lines in the center graph represent the limits between the domains where $\langle 100 \rangle$, hyperbranched and $\langle 110 \rangle$ structures are observed.

twofold (doublon) rather than fourfold fashion, respecting the symmetry of the crystal. As ε_1 increases at fixed ε_2 , the $\langle 110 \rangle$ center is overtaken by the two parallel growing tips around it. There is thus never a true $\langle 320 \rangle$ tip for example, but rather a competition between the fourfold split around $\langle 100 \rangle$ and twofold split around $\langle 110 \rangle$. The splitting in the (100) plane is thus dictated by the respective strength of those two contributions, which gives a growth advantage to one or the other. However, since the competition between those directions is very strong in the hyperbranched range and more so at low anisotropy, neither contribution overpowers the other strongly enough to dominate the morphology. Instead an alternating branching mechanism appears expressing both the $\langle 100 \rangle$ and $\langle 110 \rangle$ character.

These results should be taken with care, in fact, although the growth velocity has converged for the extreme cases with clear $\langle 100 \rangle$ and $\langle 110 \rangle$ dendrites, the speed of the doublon and quadruplon tips are still in the initial transient at the end of the simulation time we considered. Thus, our simulations should be performed for longer times to verify that those structures persist further on and are stable along the found directions in steady state. Nevertheless, our present results show a trend that cannot be ignored.

Lastly, as can be seen when comparing the $\langle 100 \rangle$ case in both vertical line scans, the lower the anisotropy, the lower the growth speed and thus also the longer it takes for selection to operate, and the more weakly the character of a certain orientation is expressed. Results from the measurement of the interfacial energy anisotropy by Napolitano *et al.* [Nap04] and this work show that the alloy used in the Bridgman experiments indeed operate their DOT in this region of weak anisotropy.

6.3.2 Columnar Growth

In order to allow a better comparison with the experimental results, directional solidification (DS) simulations have also been performed. This work is ongoing. The parameters selected for these simulations are listed in Table 6.1. All parameters that are not specifically mentioned here are kept equal to the values used in the equiaxed growth simulations.

Table 6.1: Directional solidification dimensionless simulation parameters and their dimensional equivalents.

Dimensionless parameter	Value	Dimensional equivalent
$\Delta x / W_0$	0.75	$\Delta x = 7.5 \times 10^{-8} \text{ m}$
$\varepsilon_{4\text{cor}}$	-0.025	N/A
$\Delta t / \tau_0$	0.05	$\Delta t = 2.3 \times 10^{-6} \text{ s}$
\tilde{l}_T	1×10^4	$G = 20\,777 \text{ K/m}$
\tilde{v}_P	0.25	$v_P = 543 \mu\text{m/s}$
\tilde{v}_F	0.25	$v_F = 543 \mu\text{m/s}$
Ω	0.6	N/A

In these calculations, the tip radius is not, as in the previous case, controlled by the supersaturation, but by the pulling velocity \tilde{v}_P , equal to the frame velocity \tilde{v}_F and the thermal length \tilde{l}_T . The supersaturation parameter Ω , is used here to impose the fraction

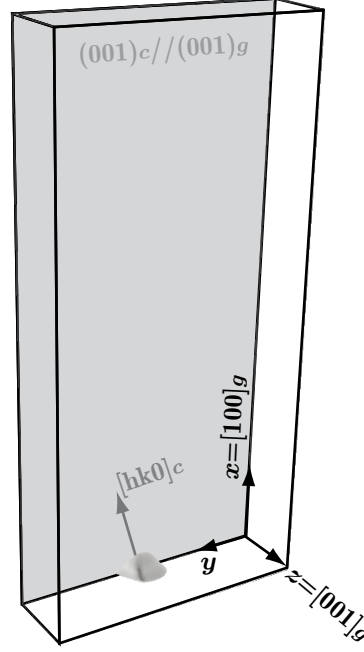


Figure 6.13: DS simulation domain and seed position configuration. A seed after 500 time steps is shown instead of the initial seed because of its small size compared to the simulation domain.

of the mushy zone, of length \tilde{l}_T , that is present in the simulation domain through the relation:

$$f_{M.Z.}(\Omega) = \frac{k\Omega}{1 - (1 - k)\Omega} \quad (6.1)$$

Thus, if $\Omega = 1$, the entire mushy zone is present in the simulation domain, if $\Omega = 0$, the tip of the dendrite would be exactly at the bottom of the domain. The first situation would make the domain very large, leading to long computation times. The value of the supersaturation was chosen to be low enough to keep the computation time reasonable, but high enough to prevent the initial seed from being pulled out of the simulation domain by the moving frame. Given the smaller mesh size chosen here, the grid anisotropy correction is slightly lower than for the equiaxed simulations, performed using $\Omega = 0.4$. Stability considerations associated with the reduction in grid spacing required shorter time steps, and thus the solidification sequence of 6000 time steps corresponds to 13 ms.

In this code, the thermal gradient is imposed along the x -axis of the simulation domain via the thermal length (Equation (2.61)). Note that the thermal gradient is artificially high to compress the mushy zone, allowing for smaller simulation domains. The size of the latter was $360 \times 168 \times 48$ in units of Δx , with the (001) set perpendicular to the z -axis. Since for the anisotropy parameters chosen here, the growth is constrained to the (001) plane, advantage was taken of the symmetry and since in DS simulations only the upper part of the solidification has to be modeled, the calculations could be performed in half a box. A reduction to one octant was not possible because the symmetry axis of the crystal was not necessarily aligned with the grid axis. The crystal seed of $5\Delta x$ in radius was initialized in the middle of the y -axis in the bottom yz -plane. Figure 6.13 shows the general configuration. The morphologies obtained in these simulations generated meshes starting with about 6000 nodes, and ending with about 2×10^6 nodes.

Four directional solidification simulations with the anisotropy parameters shown in Figure 6.11 were performed. For each set of $(\varepsilon_1, \varepsilon_2)$ the crystal orientation was chosen as shown in Table 6.2, leading to the misorientation with respect to the grid also reported in that table.

Table 6.2: DS simulation parameters of the cases shown in Figure 6.14: Anisotropy parameters, Euler angles for the rotation of the crystal with respect to the grid ($[hkl]_g$) and obtained alignments of crystal direction ($[hkl]_c$) in the (001) plane. ε_2 has a fixed value of -0.01.

Case	ε_1	ε_2	Euler angles	Alignment
(a)	0.02	-0.01	45°,0,0	$[110]_c // [100]_g$
(c)	0.03	-0.01	35°,0,0	$[110]_c$ 10° off $[100]_g$
(d)	0.05	-0.01	35°,0,0	$[110]_c$ 10° off $[100]_g$
(b)	0.10	-0.01	30°,0,0	$[110]_c$ 15° off $[100]_g$

The microstructures obtained after 6000 time steps are presented in Figure 6.14. The first observation is that although the growth directions match between experimentally observed and simulated $\langle 110 \rangle$ columnar dendrites (Figure 6.14 (a)), their morphologies are quite different. The phase-field dendrite exhibits an asymmetrical trunk and a very dense structure, whereas the experimental data shows relatively low packed cylindrical trunks and arms. The main effect responsible for this difference is that the real alloy solidifies closer to the eutectic and thus with a large solidification interval, whilst the modeling was performed with parameters corresponding to a low solute content for which the solid phase fraction evolves much faster. Moreover, the equilibrium shape measurement showed that the high zinc concentration alloys like Al-82 wt.% and 90 wt.% Zn, have a stronger $\langle 110 \rangle$ character ($\varepsilon_1 = -0.025$, $\varepsilon_2 = -0.024$) than the one used in the simulation ($\varepsilon_1 = 0.02$, $\varepsilon_2 = -0.01$) and are thus showing cylindrical trunks and arms in X-ray tomography.

An important observation is that the additional constraint brought by the thermal gradient appears to strengthen the $\langle 110 \rangle$ character of the growth mode when a $\langle 110 \rangle$ direction is close \vec{G} . Indeed, Figures 6.14 (a), (b) and (c) show that even with anisotropy parameters at which hyperbranched equiaxed dendrites have been found, the growth direction remains $\langle 110 \rangle$ or close to it, without the twofold tip splitting seen at the limit between the $\langle 110 \rangle$ and hyperbranched dendrite domain of existence in equiaxed growth. Additionally, increasing ε_1 from 0.03 to 0.05 between Figure 6.14 (c) and (d) shows that for the same crystal orientation with respect to the gradient, the higher ε_1 tilts the observed growth direction slightly further away from $[110]_c$ and closer to \vec{G} . This is consistent with what was seen in equiaxed simulations, *i.e.*, that the $\langle 110 \rangle$ character of the growth is weakened by an increase of ε_1 . Note that these calculations are coarse and cannot be taken as the effective orientation change, they merely indicate a trend.

Lastly, Figure 6.14 (b) shows a seaweed type structure, with a trunk growing at an angle with respect to the thermal gradient and secondary arms growing in the (001) on the opposite side. More secondary arms, like the ones observed in A type trunks in Al-50 wt.% Zn (see Figure 6.9) were not seen in this simulation. These other branching arms could have been suppressed by the proximity of other competing trunks, or simply by the constrained dimension perpendicular to the (001) symmetry plane. Whereas in Figures 6.14 (a), (c) and (d), the trunks grow regularly, in Figures 6.14 (b) the trunk manifests as an alternation of two growth directions, similar to those observed in quenched

X-ray tomography samples, thus confirming this alternating growth mechanism.

It must be noted that the results are affected by the use of symmetry rather than periodic boundary conditions. Indeed, the fact that the observed trunks grow at an angle with respect to the thermal gradient and the pulling velocity, makes them drift toward the side of their inclination. After a certain simulation time, the tip or at least the secondary arms start to interact with the boundary on which symmetric conditions were applied. As the solute accumulates, the tip or arms are repulsed by the boundary.

Nonetheless, the observations in this section show certain trends which have to be confirmed by a systematic scan of crystal misorientation angles and sets of anisotropy parameters. Periodic boundary conditions will be implemented in the FE code and applied to the simulation domain lateral boundaries, in a future study.

Equiaxed phase-field simulations showed that the DOT is triggered by a competition between the $\langle 100 \rangle$ and $\langle 110 \rangle$ growth characters, but does not lead to actual intermediate growth directions. X-ray tomography of quenched Bridgman samples showed that in columnar growth, intermediate textures are the consequence of an alternating growth direction mechanism, phenomenon which was confirmed by DS phase-field simulations. The latter also showed the stabilizing effect of the thermal gradient on the growth character and the importance of the relation between the crystal orientation and the anisotropy parameters. This preliminary work has not yet been extended sufficiently to explain the relation between texture and alternating growth directions. Thus, the question of how texture is selected remains open. The findings of Chapter 5 suggest that this could be linked to a curvature criterion that has yet to be assessed.

A systematic DS phase-field study of the influence of the crystal orientation combined with certain anisotropy parameter sets and more information about the relation between texture and actual alternating dendrite orientations by experimental methods, should help to answer this open question.

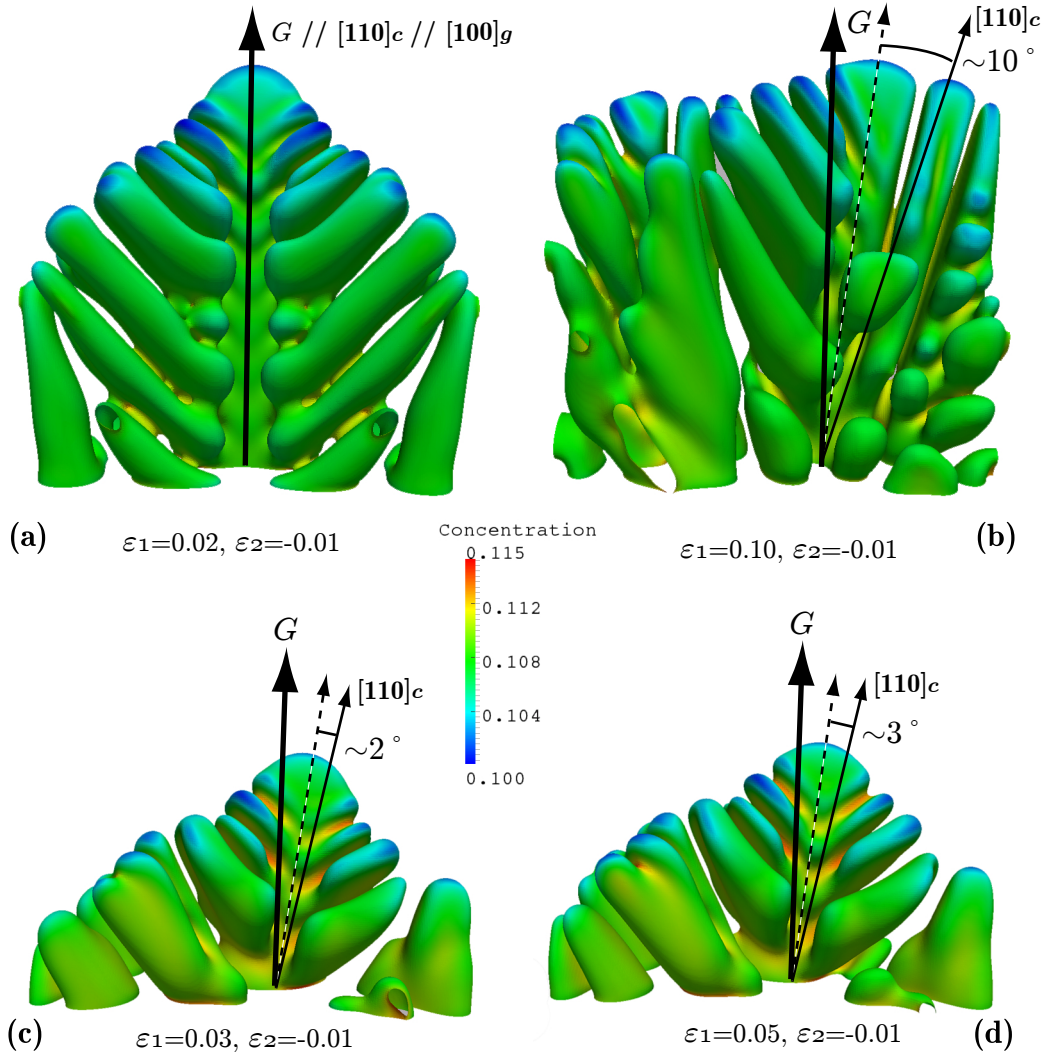


Figure 6.14: Growth structures obtained in directional solidification phase-field simulation with the four sets of anisotropy parameters and Euler rotation listed in Table 6.2. The color corresponds to the concentration at the interface, *i.e.*, where $\psi = 0$. Cases (a) and (b) are shown after 6000 time steps, whereas (c) and (d) have only grown for 4000 time steps. In these simulations the thermal gradient G , shown by the thick arrow, always points along the $[100]$ axis of the grid. The dashed arrows show the approximate growth directions and the thin solid arrows, the closest $\langle 110 \rangle$ crystallographic direction. Note that the angles have been slightly exaggerated for the purpose of illustration. The magnification can be seen from the width of the simulation domain which is $168 \times \Delta x = 12.6 \mu\text{m}$.

Chapter 7

Conclusion

We recall that the three main goals stated in the introduction of this work were:

- The determination of the anisotropy parameters of a highly alloyed Al-Zn via the measurement of equilibrium shapes.
- The further elucidation of dendrite growth morphologies and mechanisms in Al-Zn alloys via X-ray tomography of quenched samples.
- The investigation of the relationship between dendrite growth directions and the anisotropy of the solid-liquid interfacial energy via phase-field modeling of the solidification of Al-Zn alloys.

7.1 Synthesis

This work first showed the wide variety of descriptions used for γ_{sl} in literature and provided the necessary clarification to address the problem properly.

From an engineering point of view, Chapter 3 then showed how different methods, cleverly combined, could be utilized effectively to measure a property difficult to quantify. Indeed, the combination of a gradient experiment, with a successive equilibration heat treatment, generated the desired distribution of fine droplets, which could then be characterized by focused ion beam. The measurement of an equilibrium shape in an Al-82 wt.% Zn alloys allowed to compute the associated interfacial energy anisotropy parameters. They were found to be $\varepsilon_1 = -0.025 \pm 0.023$ and $\varepsilon_2 = -0.024 \pm 0.014$. Although the measurement error is large, this finding shows that the DOT, first observed by Gonzales and Rappaz [Gon06], operates in a regime of very weak anisotropy. On the hypereutectic side of the Al-Zn phase diagram, the conventional equilibrium shape measurement method, originally introduced by Liu *et al.* [Liu01], allowed to characterize the aspect ratio of a zinc equilibrium shape, but failed to measure the basal in-plane anisotropy.

The mathematical tools developed specifically for this work were used to calculate the true curvatures of equilibrium shapes. These results showed that the assumption used for the calculation of the generalized stiffness, *i.e.*, the two principal radii of curvature are equal, is only valid for a very restricted range of anisotropy. The calculations also showed that the most highly curved part of the interface, corresponding to the maximum of the

CONCLUSION

mean curvature, which was believed to dictate the growth direction, does not undergo a continuous transition between the $\langle 100 \rangle$ and $\langle 110 \rangle$ directions, with the variation anisotropy parameters. Even if this maximum curvature did not allow to find an analytical predictive criterion for the DOT, interesting trends in the behavior of the first principal curvature were found. Specific values of this curvature, related to the anisotropy strength, seems indeed to be able to predict continuous orientation transitions with ranges corresponding the those observed in phase-field. The reason for the selection of such specific radii of curvature remains however unexplained.

After performing the assessment of the mesh anisotropy in phase-field models and accounting for its effect with a correction term, equiaxed growth was simulated for a broad range of anisotropy parameters. The results of those calculations showed a slightly shifted stability limit of $\langle 100 \rangle$ dendrites towards higher values of ε_1 , when compared with those previously reported by Haxhimali *et al.* [Hax06b]. This effect was attributed to the difference in the models since this work used a dilute alloy code, whereas Haxhimali *et al.* used a code for the solidification of a pure substance. Furthermore, in the so-called hyperbranched regime, no DOT was observed in equiaxed growth, but rather a competition between $\langle 100 \rangle$ and $\langle 110 \rangle$ directions, at least at the onset of dendritic growth. Calculations at longer times should be performed to ensure that the observed behavior is not only an effect of the initial transient. For now, it thus seems that in equiaxed growth the competition between $\langle 100 \rangle$ and $\langle 110 \rangle$ depends on the selected anisotropy parameter, and favors one or the other character, but no intermediate direction.

The X-ray tomography investigations of the whole range of Al-Zn alloys, firstly confirmed the texture observations made by Gonzales and Rappaz [Gon06]. At zinc concentrations higher than 55 wt.% , dendrites grow in well defined $\langle 110 \rangle$ directions. Below 25 wt.% Zn, primary trunks grow along $\langle 100 \rangle$, but the secondary arms do not follow these directions and show an unexpected palm-tree behaviour. A formation mechanism, which matches the observations, has been proposed but further investigations are necessary to assess it.

At compositions between 25 and 55 wt.% zinc, seaweed structures in a metallic alloy were, for the first time, characterized in 3D with unprecedented details about texture, growth directions and mechanisms. The growth was confirmed to be constrained within a symmetry (100) plane. However, new findings showed that the observed macroscopic texture did not necessarily correspond to the actual growth direction. The growth seems to operate by an alternating growth direction mechanism and could be linked to the competition between $\langle 100 \rangle$ and $\langle 110 \rangle$ characters, which was observed in equiaxed growth.

Finally, directional solidification phase-field simulations showed the stabilizing effect of the thermal gradient on the twofold splitting of $\langle 110 \rangle$ dendrites. Moreover, it showed the importance of the anisotropy parameters, but also of the misorientation angles of the crystal, the thermal gradient and the actual growth direction itself. These were only preliminary results and a more systematic study on the interaction between these parameters would help to better understand the growth mechanisms. However, it was already possible to model a seaweed microstructure which is thus not only dictated by the choice of anisotropy parameters, but is truly a consequence of directional solidification, *i.e.*, the angle of the growth directions with respect to the thermal gradient.

7.2 Perspectives

Although progresses were made in the understanding of the microstructure formation mechanisms in Al-Zn alloys, some open questions remain. The advent of newly developed techniques like X-ray tomography *in situ* solidification could further broaden the spectrum of information available for interpretation. The study of seaweed or palm-tree secondary arm growth would certainly most benefit from this technological progress. Nevertheless, the extension of the post-mortem X-ray tomography study to other intermediate compositions should allow to evidence more precise relations between texture and alternating growth directions.

The reason for the continuous texture evolution observed in the DOT is still unknown and more specifically the question is: What selects the texture orientation if anisotropy, and thus the competition between $\langle 100 \rangle$ and $\langle 110 \rangle$ growth characters, dictates the growth directions of the seaweed trunks. Thus, from a fundamental point of view, the new lead about an optimum first principal curvature criterion, applied to the prediction of texture in the dendrite orientation transition, needs to be addressed with more attention, in order to determine the physical reason for such a criterion to work. The answer to the previous question would also help explaining why the texture actually differs from growth direction. Since the latter is most certainly the fastest growing direction, the reason for the misalignment with the thermal gradient remains unclear. A further question is, if the weaker growth selection mechanism, observed by Gonzales and Rappaz [Gon08] in seaweeds, is the reason or the consequence of these special microstructures?

With the capabilities of the phase-field FE model demonstrated here, the implementation of periodic boundary conditions will allow to conduct a systematic scan of the crystal misorientation, with respect to the thermal gradient in the (100) plane and anisotropy parameters $(\varepsilon_1, \varepsilon_2)$. This should complement the experimental observations suggested at the beginning of this section.

Bibliography

- [Aka95] S. Akamatsu, G. Faivre, and T. Ihle. Symmetry-broken double fingers and seaweed patterns in thin-film directional solidification of a nonfaceted cubic crystal. *Physical Review E - Statistical, Nonlinear, and Soft Matter Physics*, 51(5):4751–4780, 1995.
- [Aka97] S. Akamatsu and T. Ihle. Similarity law for the tilt angle of dendrites in directional solidification of non-axially-oriented crystals. *Physical Review E - Statistical Physics, Plasmas, Fluids, and Related Interdisciplinary Topics*, 56(4):4479–4485, 1997.
- [Aka98] S. Akamatsu and G. Faivre. Anisotropy-driven dynamics of cellular fronts in directional solidification in thin samples. *Physical Review E - Statistical, Nonlinear, and Soft Matter Physics*, 58(3):3302–3315, September 1998.
- [Alk01] J. Alkemper and P. Voorhees. Quantitative serial sectioning analysis. *Journal of Microscopy*, 201(3):388–394, 2001.
- [Ami08] M. Amini and B. Laird. Crystal-melt interfacial free energy of binary hard spheres from capillary fluctuations. *Physical Review B - Condensed Matter and Materials Physics*, 78(14):–, 2008.
- [Ass09] H. Assadi, M. Oghabi, and D. Herlach. Influence of ordering kinetics on dendritic growth morphology. *Acta Materialia*, 57(5):1639–1647, 2009.
- [Ast02] M. Asta, J. J. Hoyt, and A. Karma. Calculation of alloy solid-liquid interfacial free energies from atomic-scale simulations. *Physical Review B - Condensed Matter and Materials Physics*, 66(10):1001011–1001014, 2002.
- [Ast09] M. Asta, C. Beckermann, A. Karma, W. Kurz, R. Napolitano, M. Plapp, G. Purdy, M. Rappaz, and R. Trivedi. Solidification microstructures and solid-state parallels: Recent developments, future directions. *Acta Materialia*, 57(4):941–971, 2009.
- [Ath06] B. Athreya, J. Dantzig, S. Liu, and R. Trivedi. On the role of confinement on solidification in pure materials and binary alloys. *Philosophical Magazine*, 86(24):3739–3756, 2006.
- [BA93] M. Ben Amar and E. Brener. Theory of pattern selection in three-dimensional nonaxisymmetric dendritic growth. *Physical Review Letters*, 71(4):589–592, 1993.

BIBLIOGRAPHY

- [Bar89] A. Barbieri and J. Langer. Predictions of dendritic growth rates in the linearized solvability theory. *Physical Review A*, 39(10):5314–5325, 1989.
- [Bas69] J. D. Basterfield, W. A. Miller, and G. C. Weatherly. Anisotropy of interfacial free energy in solid-fluid and solid-solid system. *Canadian Metallurgy Quarterly*, 8:131, 1969.
- [Bec99] C. Beckermann, H.-J. Diepers, I. Steinbach, A. Karma, and X. Tong. Modeling melt convection in phase-field simulations of solidification. *Journal of Computational Physics*, 154(2):468–496, 1999.
- [Bec07] C. Becker, D. Olmsted, M. Asta, J. Hoyt, and S. Foiles. Atomistic underpinnings for orientation selection in alloy dendritic growth. *Physical Review Letters*, 98(12):–, 2007.
- [BJ86] E. Ben-Jacob, G. Deutsch, P. Garik, N. Goldenfeld, and Y. Lareah. Formation of a dense branching morphology in interfacial growth. *Physical Review Letters*, 57(15):1903–1906, 1986.
- [Boe00] W. Boettinger, S. Coriell, A. Greer, A. Karma, W. Kurz, M. Rappaz, and R. Trivedi. Solidification microstructures: recent developments, future directions. *Acta Materialia*, 48(1):43–70, 2000.
- [Boe02] W. J. Boettinger, J. A. Warren, C. Beckermann, and A. Karma. Phase-field simulation of solidification. *Annual Review of Materials Research*, 32:163–194, 2002.
- [Bre94] E. Brener, T. Ihle, H. Müller-Krumbhaar, Y. Saito, and K. Shiraishi. Fluctuation effects on dendritic growth morphology. *Physica A: Statistical Mechanics and its Applications*, 204:96–110, 1994.
- [Bre96] E. Brener, H. Müller-Krumbhaar, and D. Temkin. Structure formation and the morphology diagram of possible structures in two-dimensional diffusional growth. *Physical Review E - Statistical, Nonlinear, and Soft Matter Physics*, 54(3):2714–2722, 1996.
- [Bro86] J. Broughton and G. Gilmer. Molecular dynamics investigation of the crystal-liquid interface. VI. Excess surface free energies of crystal-liquid systems. *The Journal of Chemical Physics*, 84(10):5759–5768, 1986.
- [Bös07] U. Bösenberg, M. Buchmann, and M. Rettenmayr. Initial transients during solid/liquid phase transformations in a temperature gradient. *Journal of Crystal Growth*, 304(1):281–286, 2007.
- [Buc05] M. Buchmann and M. Rettenmayr. Microstructure evolution during melting and resolidification in a temperature gradient. *Journal of Crystal Growth*, 284(3-4):544–553, 2005.
- [Bur04] E. Burman, A. Jacot, and M. Picasso. Adaptive finite elements with high aspect ratio for the computation of coalescence using a phase-field model. *Journal of Computational Physics*, 195(1):153–174, 2004.

- [Cha64] B. Chalmers. *Principles of Solidification*. John Wiley, New York, 1964.
- [Cha76] S. K. Chan, H. H. Reimer, and M. Kahlweit. On the stationary growth shapes of NH_4Cl dendrites. *Journal of Crystal Growth*, 32(3):303–315, 1976.
- [Cha08] D. Chatain. Anisotropy of wetting. *Annual Review of Materials Research*, 38:45–70, 2008.
- [Cha10] V. Chapuis. Comparaison des courbures calculées par champ de phase et modélisation granulaire, pour une solidification globulaire. Master’s thesis, EPFL, January 2010.
- [Cly80a] T. W. Clyne. Heat flow in controlled directional solidification of metals. I Experimental investigation. *Journal of Crystal Growth*, 50(3):684–690, November 1980.
- [Cly80b] T. W. Clyne. Heat flow in controlled directional solidification of metals. II Mathematical model. *Journal of Crystal Growth*, 50(3):691–700, November 1980.
- [Cru08] K. Cruz, J. Spinelli, I. Ferreira, N. Cheung, and A. Garcia. Microstructural development in Al-Sn alloys directionally solidified under transient heat flow conditions. *Materials Chemistry and Physics*, 109(1):87–98, 2008.
- [Cru09] K. Cruz, I. Ferreira, J. Spinelli, N. Cheung, and A. Garcia. Inverse segregation during transient directional solidification of an Al-Sn alloy: Numerical and experimental analysis. *Materials Chemistry and Physics*, 115(1):116–121, 2009.
- [Dan09a] J. Dantzig and M. Rappaz. *Solidification*, chapter 8. Dendritic Growth, pages 287–344. EPFL Press, 1st edition, 2009.
- [Dan09b] J. Dantzig and M. Rappaz. *Solidification*, chapter 14. Macrosegregation, pages 567–607. EPFL Press, 1st edition, 2009.
- [Dav00] R. L. Davidchack and B. B. Laird. Direct calculation of the hard-sphere crystal/melt interfacial free energy. *Physical Review Letters*, 85(22):4751–4754, 2000.
- [Dav03] R. Davidchack and B. Laird. Direct calculation of the crystal-melt interfacial free energies for continuous potentials: Application to the Lennard-Jones system. *Journal of Chemical Physics*, 118(16):7651–7657, 2003.
- [Dav05] R. Davidchack and B. Laird. Crystal structure and interaction dependence of the crystal-melt interfacial free energy. *Physical Review Letters*, 94(8):1–4, 2005.
- [Dav06] R. Davidchack, J. Morris, and B. Laird. The anisotropic hard-sphere crystal-melt interfacial free energy from fluctuations. *Journal of Chemical Physics*, 125(9):–, 2006.
- [Des06] J. Deschamps, M. Georgelin, and A. Pocheau. Crystal anisotropy and growth directions in directional solidification. *Europhysics Letters*, 76(2):291–297, 2006.

BIBLIOGRAPHY

- [Din91] A. Dinsdale. SGTE data for pure elements. *Calphad*, 15(4):317–425, 1991.
- [Dow99] B. A. Dowd, G. H. Campbell, R. B. Marr, V. Nagarkar, S. Tipnis, L. Axe, and D. Siddons. Developments in synchrotron X-ray computed microtomography at the national synchrotron light source. *Proceedings of SPIE - The International Society for Optical Engineering*, 3772:224–236, 1999.
- [Dre90] D. A. Drew. Evolution of geometric statistics. *SIAM Journal on Applied Mathematics*, 50(3):649–666, 1990.
- [Du03] Y. Du, Y. Chang, B. Huang, W. Gong, Z. Jin, H. Xu, Z. Yuan, Y. Liu, Y. He, and F.-Y. Xie. Diffusion coefficients of some solutes in fcc and liquid al: Critical evaluation and correlation. *Materials Science and Engineering A*, 363(1-2):140–151, 2003.
- [Du07] D. Du, H. Zhang, and D. Srolovitz. Properties and determination of the interface stiffness. *Acta Materialia*, 55(2):467–471, 2007.
- [Ech04] B. Echebarria, R. Folch, A. Karma, and M. Plapp. Quantitative phase-field model of alloy solidification. *Physical Review E - Statistical, Nonlinear, and Soft Matter Physics*, 70(6 1):–, 2004.
- [Emm99] H. Emmerich, D. Schleussner, T. Ihle, and K. Kassner. Confinement effects in dendritic growth. *Journal of Physics Condensed Matter*, 11(46):8981–8993, 1999.
- [Erc94] F. Ercolessi and J. Adams. Interatomic potentials from first-principles calculations: the force-matching method. *Europhysical Letters*, 26:583, 1994.
- [Feh76] W. R. Fehlner and S. H. Vosko. Product representation for cubic harmonics and special directions for the determination of the fermi surface and related properties. *Canadian Journal of Physics*, 54(21):2159–2169, 1976.
- [Fel84] I. Feldkamp, L. Davis, and J. Kress. Practical cone-beam algorithm. *Journal of the Optical Society of America A: Optics and Image Science, and Vision*, 1(6):612–619, 1984.
- [Fis82] M. Fisher, D. Fisher, and J. Weeks. Agreement of capillary-wave theory with exact results for the interface profile of the two-dimensional ising model. *Physical Review Letters*, 48(5):368–, 1982.
- [Fis11] S. Fischer and M. Rettenmayr. Production of fine droplets in metallic samples with the aim of measuring the interfacial energies. Unpublished work, 2011.
- [Gli89] M. E. Glicksman and N. B. Singh. Effects of crystal-melt interfacial energy anisotropy on dendritic morphology and growth kinetics. *Journal of Crystal Growth*, 98(3):277–284, 1989.
- [Gün85] Gündüz and J. Hunt. The measurement of solid-liquid surface energies in the Al-Cu, Al-Si and Pb-Sn systems. *Acta Metallurgica*, 33(9):1651–1672, 1985.

- [Gon06] F. Gonzales and M. Rappaz. Dendrite growth directions in aluminum-zinc alloys. *Metallurgical and Materials Transactions A: Physical Metallurgy and Materials Science*, 37(9):2797–2806, 2006.
- [Gon08] F. Gonzales and M. Rappaz. Grain selection and texture evolution in directionally solidified Al-Zn alloys. *Metallurgical and Materials Transactions A: Physical Metallurgy and Materials Science*, 39(9):2148–2160, 2008.
- [Gon09] F. Gonzales. *Etude des morphologies de solidification dans les alliages aluminium-zinc*. PhD thesis, Ecole Polytechnique Fédérale de Lausanne, 2009.
- [Gra99] A. Gray. *Modern Differential Geometry of Curves and Surfaces with Mathematics*, chapter Surfaces In 3-Dimensional Space, pages 359–390. CRC Press, 2nd edition, 1999.
- [Gra04] L. Granasy, T. Pusztai, T. Börzsönyi, J. Warren, and J. Douglas. A general mechanism of polycrystalline growth. *Nature Materials*, 3(9):645–650, 2004.
- [Hal89] C. Hall. Process of reducing aluminium from its fluoride salts by electrolysis. US Patent No. 400,664, 1889.
- [Hax06a] T. Haxhimali. *Phase-field simulation study of dendritic crystal growth morphologies for cubic and hexagonal symmetries*. PhD thesis, Northeastern University, 2006.
- [Hax06b] T. Haxhimali, A. Karma, F. Gonzales, and M. Rappaz. Orientation selection in dendritic evolution. *Nature Materials*, 5(8):660–664, 2006.
- [Hen98a] S. Henry, P. Jarry, and M. Rappaz. $\langle 110 \rangle$ dendrite growth in aluminum feathery grains. *Metallurgical and Materials Transactions A: Physical Metallurgy and Materials Science*, 29(11):2807–2817, 1998.
- [Hen98b] S. Henry, T. Minghetti, and M. Rappaz. Dendrite growth morphologies in aluminium alloys. *Acta Materialia*, 46(18):6431–6443, 1998.
- [Her51] C. Herring. *The physics of powder metallurgy*, chapter Surface tension as a motivation for sintering, pages 143–177. McGraw-Hill, 1951.
- [Hin10] C. Hintermüller, F. Marone, A. Isenegger, and M. Stampanoni. Image processing pipeline for synchrotron-radiation-based tomographic microscopy. *Journal of Synchrotron Radiation*, 17(4):550–559, 2010.
- [Hof72] D. Hoffman and J. Cahn. A vector thermodynamics for anisotropic surfaces. I. Fundamentals and application to plane surface junctions. *Surface Science*, 31(C):368–388, 1972.
- [Hor61] G. Horvay and J. Cahn. Dendritic and spheroidal growth. *Acta Metallurgica*, 9(7):695–705, July 1961.
- [Hoy01] J. J. Hoyt, M. Asta, and A. Karma. Method for computing the anisotropy of the solid-liquid interfacial free energy. *Physical Review Letters*, 86(24):5530–5533, 2001.

BIBLIOGRAPHY

- [Hoy02] J. J. Hoyt and M. Asta. Atomistic computation of liquid diffusivity, solid-liquid interfacial free energy, and kinetic coefficient in Au and Ag. *Physical Review B - Condensed Matter and Materials Physics*, 65(21):2141061–21410611, 2002.
- [Hoy03] J. J. Hoyt, M. Asta, and A. Karma. Atomistic and continuum modeling of dendritic solidification. *Materials Science and Engineering R: Reports*, 41(6):–, 2003.
- [Hoy04] J. Hoyt, M. Asta, T. Haxhimali, A. Karma, R. Napolitano, R. Trivedi, B. Laird, and J. Morris. Crystal-melt interfaces and solidification morphologies in metals and alloys. *MRS Bulletin*, 29(12):935–939, 2004.
- [Hér86] P. Hérault. Procédé électrolytique pour la préparation de l’aluminium. French Patent No. 175711, 1886.
- [Ihl93] T. Ihle and H. Müller-Krumbhaar. Diffusion-limited fractal growth morphology in thermodynamical two-phase systems. *Physical Review Letters*, 70(20):3083–3086, 1993.
- [Iva47] G. Ivantsov. Temperature field around the spherical, cylindrical and needle-crystals which grow in supercooled melt. *Dokl. Akad. Nauk USSR*, 58:567, 1947.
- [Jac08] A. Jacot. Quantitative phase field model for alloy solidification. Private communication, 2008.
- [Jeo01] J.-H. Jeong, N. Goldenfeld, and J. Dantzig. Phase field model for three-dimensional dendritic growth with fluid flow. *Physical Review E - Statistical, Nonlinear, and Soft Matter Physics*, 64(4 I):416021–4160214, 2001.
- [Jeo03] J.-H. Jeong, J. Dantzig, and N. Goldenfeld. Dendritic growth with fluid flow in pure materials. *Metallurgical and Materials Transactions A: Physical Metallurgy and Materials Science*, 34 A(3):459–466, 2003.
- [Kak87] A. Kak and M. Slaney. *Principles of computerized tomography imaging*. IEEE Press, 1987.
- [Kar97] A. Karma and W.-J. Rappel. Phase-field simulation of three-dimensional dendrites: Is microscopic solvability theory correct? *Journal of Crystal Growth*, 174(1-4):54–64, 1997.
- [Kar98] A. Karma and W.-J. Rappel. Quantitative phase-field modeling of dendritic growth in two and three dimensions. *Physical Review E - Statistical, Nonlinear, and Soft Matter Physics*, 57(4):4323–4349, 1998.
- [Kar01] A. Karma. Phase-field formulation for quantitative modeling of alloy solidification. *Physical Review Letters*, 87(11):–, 2001.
- [Kat01] D. Katrakova and F. Muecklich. Specimen preparation for electron backscatter diffraction - Part I: Metals. *Praktische Metallographie - Practical Metallography*, 38(10):547–565, 2001.

- [Kes88] D. A. Kessler, J. Koplik, and H. Levine. Pattern selection in fingered growth phenomena. *Advances in Physics*, 37(3):255–339, 1988.
- [Kim99] Y.-T. Kim, N. Provatas, N. Goldenfeld, and J. Dantzig. Universal dynamics of phase-field models for dendritic growth. *Physical Review E - Statistical Physics, Plasmas, Fluids, and Related Interdisciplinary Topics*, 59(3 PART A):R2546–R2549, 1999.
- [Kur98] W. Kurz and D. Fisher. *Fundamentals of Solidification*. Trans Tech Publications, 4th edition, 1998.
- [Kur11] G. Kurtuldu, P. Jarry, and M. Rappaz. Unpublished work. 2011.
- [Lai05] B. Laird and R. Davidchack. Direct calculation of the crystal-melt interfacial free energy via molecular dynamics computer simulation. *Journal of Physical Chemistry B*, 109(38):17802–17812, 2005.
- [Lan78] J. Langer and H. Müller-Krumbhaar. Theory of dendritic growth-I. Elements of a stability analysis. *Acta Metallurgica*, 26(11):1681–1687, 1978.
- [Lan87] J. Langer. Chance and matter. In J. Souletie, J. Vannimenus, and R. Stora, editors, *Proceedings of the Les Houches Summer School, Session XLVI*, pages 629–711, Amsterdam, 1987. North-Holland.
- [Liu01] S. Liu, R. E. Napolitano, and R. Trivedi. Measurement of anisotropy of crystal-melt interfacial energy for a binary Al-Cu alloy. *Acta Materialia*, 49(20):4271–4276, 2001.
- [Liu06] S. Liu, J. Li, J. Lee, and R. Trivedi. Spatio-temporal microstructure evolution in directional solidification processes. *Philosophical Magazine*, 86(24):3717–3738, 2006.
- [Lud05] O. Ludwig, M. Dimichiel, L. Salvo, M. Suery, and P. Falus. In-situ three-dimensional microstructural investigation of solidification of an Al-Cu alloy by ultrafast X-ray microtomography. *Metallurgical and Materials Transactions A: Physical Metallurgy and Materials Science*, 36(6):1515–1523, 2005.
- [Mad11] K. Mader, F. Marone, C. Hintermüller, G. Mikuljan, A. Isenegger, and M. Stampanoni. High-throughput full-automatic synchrotron-based tomographic microscopy. *Journal of Synchrotron Radiation*, 18:117–124, 2011.
- [Mar10a] A. Mariaux. *Texture formation in hot-dip galvanized coatings: Nucleation and growth of anisotropic grains in a confined geometry*. PhD thesis, EPFL, 2010.
- [Mar10b] F. Marone, B. Münch, and M. Stampanoni. Fast reconstruction algorithm dealing with tomography artifacts. *Proceedings of SPIE - The International Society for Optical Engineering*, 7804(10):–, 2010.
- [Mas86] T. B. Massalski. *Binary Alloy Phase Diagrams: Volume 1 (Ac-Au to Fe-Rh)*, volume 1, chapter Al-Zn, pages 184–188. American Society for Metals, Materials Park, Ohio, 1986.

BIBLIOGRAPHY

- [Mat99] R. Mathiesen, L. Arnberg, F. Mo, T. Weitkamp, and A. Snigirev. Time resolved X-ray imaging of dendritic growth in binary alloys. *Physical Review Letters*, 83(24):5062–5065, 1999.
- [Mat05] R. Mathiesen and L. Arnberg. X-ray radiography observations of columnar dendritic growth and constitutional undercooling in an Al-30wt%Cu alloy. *Acta Materialia*, 53(4):947–956, 2005.
- [McF93] G. McFadden, A. Wheeler, R. Braun, S. Coriell, and R. Sekerka. Phase-field models for anisotropic interfaces. *Physical Review E - Statistical, Nonlinear, and Soft Matter Physics*, 48(3):2016–2024, 1993.
- [Mei92] J. Mei and J. Davenport. Free-energy calculations and the melting point of Al. *Physical Review B*, 46(1):21–25, 1992.
- [Men03] R. Mendoza, J. Alkemper, and P. Voorhees. The morphological evolution of dendritic microstructures during coarsening. *Metallurgical and Materials Transactions A: Physical Metallurgy and Materials Science*, 34 A(3):481–489, 2003.
- [Men05] M. Mendelev, D. Srolovitz, G. Ackland, and S. Han. Effect of Fe segregation on the migration of a non-symmetric $\sigma 5$ tilt grain boundary in Al. *Journal of Materials Research*, 20(1):208–218, 2005.
- [Mey86] S. a. Mey and G. Effenberg. A thermodynamic evaluation of the aluminum-zinc system. *Zeitschrift fuer Metallkunde/Materials Research and Advanced Techniques*, 77(7):449–453, 1986.
- [Mil69a] W. A. Miller and G. A. Chadwick. The equilibrium shapes of small liquid droplets in solid-liquid phase mixtures: Metallic h.c.p. and metalloid systems. *Proceedings of the Royal Society A - Mathematical, Physical and Engineering Sciences*, 312(1509):257–276, 1969.
- [Mil69b] W. Miller, G. Carpenter, and G. Chadwick. Anisotropy of interfacial free energy of some hexagonal close-packed metals. *Philosophical Magazine*, 19(158):305–319, 1969.
- [Mok10] R. Mokso, F. Marone, and M. Stampanoni. Real time tomography at the Swiss Light Source. *AIP Conference Proceedings*, 1234:87–90, 2010.
- [Mol67] F. Mollar and M. Flemings. *Trans. Met. Soc. AIME*, 239:1543, 1967.
- [Mor02] J. R. Morris. Complete mapping of the anisotropic free energy of the crystal-melt interface in Al. *Physical Review B - Condensed Matter and Materials Physics*, 66(14):1441041–1441047, 2002.
- [Mor03] J. R. Morris and X. Song. The anisotropic free energy of the Lennard-Jones crystal-melt interface. *Journal of Chemical Physics*, 119(7):3920–3925, 2003.
- [Mor07] J. Morris, M. Mendelev, and D. Srolovitz. A comparison of crystal-melt interfacial free energies using different Al potentials. *Journal of Non-Crystalline Solids*, 353(32-40):3565–3569, 2007.

- [Mul63] W. W. Mullins and R. F. Sekerka. Morphological stability of a particle growing by diffusion or heat flow. *Journal of Applied Physics*, 34(2):323–329, 1963.
- [Mul01] A. Mullis, D. Walker, S. Battersby, and R. Cochrane. Deformation of dendrites by fluid flow during rapid solidification. *Materials Science and Engineering A*, 304-306(1-2):245–249, 2001.
- [Mul04] A. Mullis, K. Dragnevski, and R. Cochrane. The transition from the dendritic to the seaweed growth morphology during the solidification of deeply undercooled metallic melts. *Materials Science and Engineering A*, 375-377(1-2 SPEC. ISS.):157–162, 2004.
- [Mur83] K. Murakami, T. Fujiyama, A. Koike, and T. Okamoto. Influence of melt flow on the growth directions of columnar grains and columnar dendrites. *Acta Metallurgica*, 31(9):1425–1432, 1983.
- [Mur84] K. Murakami, H. Aihara, and T. Okamoto. Growth direction of columnar crystals solidified in flowing melt. *Acta Metallurgica*, 32(6):933–939, 1984.
- [Mus92] M. Muschol, D. Liu, and C. H. Z. Surface-tension-anisotropy measurements of succinonitrile and pivalic acid: Comparison with microscopic solvability theory. *Physical Review A*, 46(2):1038–1051, 1992.
- [Nap02] R. E. Napolitano, S. Liu, and R. Trivedi. Experimental measurement of anisotropy in crystal-melt interfacial energy. *Interface Science*, 10(2-3):217–232, 2002.
- [Nap04] R. E. Napolitano and S. Liu. Three-dimensional crystal-melt Wulff-shape and interfacial stiffness in the Al-Sn binary system. *Physical Review B - Condensed Matter and Materials Physics*, 70(21):1–11, 2004.
- [Nar07] J. Narski and M. Picasso. Adaptive finite elements with high aspect ratio for dendritic growth of a binary alloy including fluid flow induced by shrinkage. *Computer Methods in Applied Mechanics and Engineering*, 196(37-40 SPEC. ISS.):3562–3576, 2007.
- [Nie06a] C. Niederberger, J. Michler, and A. Jacot. Inverse method for the determination of a mathematical expression for the anisotropy of the solid-liquid interfacial energy in Al-Zn-Si alloys. *Physical Review E - Statistical, Nonlinear, and Soft Matter Physics*, 74(2):–, 2006.
- [Nie06b] C. Niederberger, J. Michler, and A. Jacot. A multiscale approach for the simulation of dendritic microstructures in al-zn-si coatings. In C.-A. Gandin, M. Bellet, and J. Allison, editors, *Modeling of Casting, Welding and Advanced Solidification Processes XI*, pages 481–488. TMS, Warrendale, 2006.
- [Nie07] C. Niederberger. *Experimental and numerical study of microstructure formation and the origin of crystallographic misorientations in Al-Zn-Si alloy coatings*. PhD thesis, EPFL, 2007.

BIBLIOGRAPHY

- [Oso06] W. Osorio, J. Spinelli, N. Cheung, and A. Garcia. Secondary dendrite arm spacing and solute redistribution effects on the corrosion resistance of Al-10 wt% Sn and Al-20 wt% Zn alloys. *Materials Science and Engineering A*, 420(1-2):179–186, 2006.
- [Pap35] A. Papapetrou. Untersuchungen über dendritisches Wachstum von Kristallen. *Zeitschrift für Kristallographie*, 92:89–130, 1935.
- [Pas80a] A. Passerone and N. Eustathopoulos. Experimental study of the solid-liquid equilibrium roughening transition in zn-in alloys. *Journal of Crystal Growth*, 49:757–760, 1980.
- [Pas80b] A. Passerone, R. Sangiorgi, and N. Eustathopoulos. Isothermal faceted to non-faceted equilibrium transition of solid-liquid interfaces in Zn-Bi-In alloys. *Scripta metallurgica*, 14(10):1089–1092, 1980.
- [Pas82] A. Passerone and N. Eustathopoulos. Equilibrium structural transitions of solid-liquid interfaces in zinc based alloys. *Acta Metallurgica*, 30(7):1349–1356, 1982.
- [Pat06] M. Patra and M. Karttunen. Stencils with isotropic discretization error for differential operators. *Numerical Methods for Partial Differential Equations*, 22(4):936–953, 2006.
- [Pet89] K. Pettersen and N. Ryum. Crystallography of directionally solidified magnesium alloy az91. *Metallurgical Transactions A - Physical metallurgy and materials science*, 20(5):847–852, 1989.
- [Pet90] K. Pettersen, O. Lohne, and N. Ryum. Dendritic solidification of magnesium alloy az91. *Metallurgical Transactions A - Physical metallurgy and materials science*, 21(1):221–230, 1990.
- [Pet01] G. Petzow. *Metallographic Etching*, chapter Aluminum, pages 57–64. American Society of Metals, second edition, 2001.
- [Por01] D. Porter and K. Easterling. *Phase transformations in metals and alloys*, chapter Diffusional transformations in solids, page 304. Nelson Thornes Ltd, second edition, 2001.
- [Pro98] N. Provatas, N. Goldenfeld, and J. Dantzig. Efficient computation of dendritic microstructures using adaptive mesh refinement. *Physical Review Letters*, 80(15):3308–3311, 1998.
- [Pro99a] N. Provatas, N. Goldenfeld, and J. Dantzig. Adaptive mesh refinement computation of solidification microstructures using dynamic data structures. *Journal of Computational Physics*, 148(1):265–290, 1999.
- [Pro99b] N. Provatas, N. Goldenfeld, J. Dantzig, J. Lacombe, A. Lupulescu, M. Koss, M. Glicksman, and R. Almgren. Crossover scaling in dendritic evolution at low undercooling. *Physical Review Letters*, 82(22):4496–4499, 1999.

- [Pro03] N. Provatas, Q. Wang, M. Haataja, and M. Grant. Seaweed to dendrite transition in directional solidification. *Physical Review Letters*, 91(15):1555021–1555024, 2003.
- [Pro05] N. Provatas, M. Greenwood, B. Athreya, N. Goldenfeld, and J. Dantzig. Multiscale modeling of solidification: Phase-field methods to adaptive mesh refinement. *International Journal of Modern Physics B*, 19(31):4525–4565, 2005.
- [Rad17] J. Radon. Ueber die Bestimmung von Funktionen durch ihre Integralwerte längs gewisser Mannigfaltigkeiten. *Berichte über die Verhandlungen der Sächsische Akademie der Wissenschaften Leipzig*, 69:262–277, 1917.
- [Rad21] J. Radon. Mengen konvexer Körper, die einen gemeinsamen Punkt enthalten. *Mathematische Annalen*, 83(1-2):113–115, 1921.
- [Ran00] V. Randle. *Electron Backscatter Diffraction in Materials Science*. Kluwer Academic, 2000.
- [Rap10] M. Rappaz, J. Friedli, A. Mariaux, and M. Salgado-Ordorica. The influence of solid-liquid interfacial energy anisotropy on equilibrium shapes, nucleation, triple lines and growth morphologies. *Scripta Materialia*, 62(12):904–909, 2010.
- [Ret06] M. Rettenmayr and M. Buchmann. Solidification and melting - asymmetries and consequences. *Materials Science Forum*, 508:205–210, 2006.
- [Rhe08] M. Rheme, F. Gonzales, and M. Rappaz. Growth directions in directionally solidified Al-Zn and Zn-Al alloys near eutectic composition. *Scripta Materialia*, 59(4):440–443, 2008.
- [Rin72] M. Rinaldi, R. Sharp, and M. Flemings. Growth of ternary composites from the melt: Part II. *Metallurgical Transactions*, 3(12):3139–3148, 1972.
- [Roz11] R. Rozas and J. Horbach. Capillary wave analysis of rough solid-liquid interfaces in nickel. *Europhysics Letters*, 93(2):–, 2011.
- [Sal06] L. Salvo, M. Pana, M. Suery, M. Dimichiel, O. Nielsen, and D. Bernard. Fast X-ray tomography investigation of solidification microstructure and defect formation in aluminium alloys. In *Modeling of Casting, Welding and Advanced Solidification Processes - XI*, volume 1, pages 351–358, ICMCB-CNRS, 33608 Pessac Cedex, France, 2006.
- [Sem00] A. Semoroz, S. Henry, and M. Rappaz. Application of the phase-field method to the solidification of hot-dipped galvanized coatings. *Metallurgical and Materials Transactions A: Physical Metallurgy and Materials Science*, 31(2):487–495, 2000.
- [Sem01] A. Semoroz, Y. Durandet, and M. Rappaz. EBSD characterization of dendrite growth directions, texture and misorientations in hot-dipped Al-Zn-Si coatings. *Acta Materialia*, 49(3):529–541, 2001.
- [Smi55] V. Smith, W. Tiller, and J. Rutter. A mathematical analysis of solute redistribution during solidification. *Canadian Journal of Physics*, 33:723–745, 1955.

BIBLIOGRAPHY

- [Smi83] C. Smithells and E. Brandes. *Smithells Metals Reference Book*, chapter The physical properties of pure metals. Butterworths, London, sixth edition, 1983.
- [Sni98] M. Snir, S. Otto, S. Hauss-Lederman, D. Walker, and J. Dongarra. *MPI - The complete reference: Volume 1, The MPI Core*. The MIT Press, 1998.
- [SO08] M. Salgado-Ordorica and M. Rappaz. Twinned dendrite growth in binary aluminum alloys. *Acta Materialia*, 56(19):5708–5718, 2008.
- [SO09a] M. Salgado-Ordorica. *Characterization and Modeling of Twinned Dendrite Growth*. PhD thesis, EPFL, 2009.
- [SO09b] M. Salgado-Ordorica, J.-L. Desbiolles, and M. Rappaz. Phase field modelling of twinned dendrite growth. In *Proceedings from the 12th International Conference on Modeling of Casting, Welding, and Advanced Solidification Processes*, pages 545–552, Computational Materials Laboratory, Ecole Polytechnique Fédérale de Lausanne, CH-1015 Lausanne, Switzerland, 2009.
- [SO09c] M. Salgado-Ordorica, J. Vallotton, and M. Rappaz. Study of twinned dendrite growth stability. *Scripta Materialia*, 61(4):367–370, 2009.
- [Sta06] M. Stampanoni, A. Groso, A. Isenegger, G. Mikuljan, Q. Chen, A. Bertrand, S. Henein, R. Betemps, U. Frommherz, P. Böhler, D. Meister, M. Lange, and R. Abela. Trends in synchrotron-based tomographic imaging: The SLS experience. *Progress in Biomedical Optics and Imaging - Proceedings of SPIE*, 6318:1605–7422, 2006.
- [Stu00] J. Sturgeon and B. Laird. Adjusting the melting point of a model system via gibbs-duhem integration: Application to a model of aluminum. *Physical Review B - Condensed Matter and Materials Physics*, 62(22):14720–14727, 2000.
- [Sun64] B. E. Sundquist. A direct determination of the anisotropy of the surface free energy of solid gold, silver, copper, nickel and alpha and gamma iron. *Acta Metallurgica*, 12:67–86, 1964.
- [Til69] W. Tiller. Migration of a liquid zone through a solid. *Journal of Crystal Growth*, 6:77–85, 1969.
- [Tön98] R. Tönhardt and G. Amberg. Phase-field simulation of dendritic growth in a shear flow. *Journal of Crystal Growth*, 194(3-4):406–425, 1998.
- [Tri94] R. Trivedi and W. Kurz. Dendritic growth. *International Materials Reviews*, 39(2):49–74, 1994.
- [Val10] J. Valencia and P. Quested. *Metals Process Simulation*, volume 22B of *ASM Handbook*, chapter Thermophysical Properties, pages 18–32. ASM International, Materials Park, Ohio, 2010.
- [Whe92] A. Wheeler, W. Boettinger, and G. McFadden. Phase-field model for isothermal phase transitions in binary alloys. *Physical Review A*, 45(10):7424–7439, 1992.
- [Wul01] G. Wulff. Zur Frage der Geschwindigkeit des Wachstums und der Auflösung der Krystallflächen. *Zeitschrift für Kristallographie*, 34:449–530, 1901.

Appendix A

Notation

Latin Characters

a_1, a_2	Numerical constant of the phase-field model
c_ℓ^*	Liquid composition at the dendrite tip
c_ℓ^0	Liquid composition of a flat interface
c_ℓ^z	Equilibrium composition at temperature T_z
c_∞	Composition far from the interface
c_0	Nominal composition of an alloy
c_P	Heat capacity
D, D_ℓ, D_s	Solute diffusion coefficients
d_0	Chemical capillary length
E, F, G	Coefficients of the first fundamental form
e, f, g	Coefficients of the second fundamental form
\mathcal{F}	Free energy functional
$ Fo$	Fourier number
$f_{M.Z.}$	Fraction of the mushy zone
$f(\phi, T, c)$	Volumetric free energy density (phase field model)
G	Thermal gradient
$g(\phi)$	Double-well function (phase field model)
H	Mean curvature
\mathcal{H}	Coefficient of the double-well energy term (phase field model)
$Iv(x)$	Ivantsov's function
\vec{j}	Flux of solute
k_0	Partition coefficient
K	Gaussian curvature
K_1, K_2	Principal curvatures
$\underline{\underline{K}}$	Curvature tensor

NOTATION

$\mathcal{K}_i(\theta, \varphi)$	Cubic harmonics (order i)
L_f	Latent heat
l_T	Thermal length
M	Phase mobility (phase field model)
m_ℓ	Liquidus slope
N_i	Normalization constant of cubic harmonics
\vec{n}, n_x, n_y, n_z	Normal unit vector and its x -, y -, z -components
Pe	Péclet number
P_l^m	Legendre polynomial
Q, S, M	Fonctions respecting the fourfold symmetry of cubic crystals
R_1, R_2	Principal radii of curvature
R_{tip}	Dendrite tip radius
\vec{r}	Position vector in \mathbb{R}^3
$r(\theta, \varphi)$	Surface point in spherical coordinates
T	Temperature
T_M	Melting point
t	Time
\tilde{U}	Dimensionless supersaturation
V	Volume
V^m	Molar volume
v	Speed
v_P	Pulling speed
W_0	Interface thickness in the non-dimensional phase-field model
Y_l^m	Spherical harmonic function of order l, m
$[hkl]_g$	Direction with respect to the grid
$[hkl]_c$	Direction with respect to the crystal
\sim	Dimensionless variables

Greek Characters

Γ_{sl}	Gibbs-Thomson coefficient
γ_{sl}	Solid-liquid interfacial energy
γ_{sl}^0	Orientation averaged interfacial energy
ΔT	Undercooling
Δt	Time step (phase field model)
Δx	Mesh spacing (phase field model)
$\Delta\mu$	Variation of the chemical potential
δ	Interface thickness (dimensional phase field model)
δ_i	Amplitude of the deformation of the spherical harmonics (order i)
ϵ	Coefficient of the phase-gradient energy term (phase field model)
ε_i	Interfacial energy anisotropy parameter
ε_{ieff}	Effective anisotropy parameter
$\eta(\vec{n})$	Anisotropy function (phase field model)
\vec{t}	Dimensionless antitrapping current
θ	Polar angle in spherical coordinates
λ_1, λ_2	Primary and secondary dendrite arm spacing
$\vec{\xi}$	Cahn and Hoffman's $\vec{\xi}$ -vector, vector geometry construction of Wulff's plot
τ	Time in the non-dimensional phase field model
τ_0	Relaxation time in the non-dimensional phase field model
ρ_a, ρ_b, ρ_c	Radius ratios
$\vec{\rho}$	Position vector
σ^*	Dendrite tip selection constant
Φ_{sl}	Generalized interface stiffness
$\underline{\underline{\Phi}}_{sl}$	Stiffness tensor
φ	Azimuthal angle in spherical coordinates
ϕ	Phase variable in the dimensional phase field model
ψ	Phase variable in the non-dimensional phase field model
Ω	Supersaturation

Appendix B

List of X-ray tomography samples and scanning conditions

X-ray tomography conditions used for the scans of Bridgman solidified and quenched samples. All stacks were reconstructed with the GridRec algorithm. Unless otherwise specified, scans started with the dendrite tips (observable in radiography) at one fifth of the height of the field of view from the top of the first scan. Multi-blocks scans were acquired from there on downwards into the mushy zone, overlapping by a few μm .

Table B.1: Aluminum copper alloys.

Sample	Cu [wt.%]	v_P [mm/min]	\varnothing [μm]	Optic	Field of view [μm]	Pixel size [μm]	CCD w \times h	Energy [keV]	Transmission [%]	Exposure time [ms]	Projections	Scan time per block [min]	Blocks	Comment
A4C2	4	4	1400	10	1514	0.74	2048 \times 2048	21	27	220	1501	12	3	
A4Cy	4	10	1400	10	1515	0.74	2048 \times 2048	20	26	360	1501	12	2	
A15C6	15	1	2400	4	3785	1.85	2048 \times 1649	28	17	600	1501	24	2	
A15C1	15	4	2400	4	3785	1.85	2048 \times 1649	28	17	600	1501	24	2	
A15C4	15	10	1400	10	1515	0.74	2048 \times 2048	28	32	600	1501	16	2	
A15C3	15	20	1400	10	1515	0.74	2048 \times 2048	28	32	600	1501	16	2	

LIST OF X-RAY TOMOGRAPHY SAMPLES AND SCANNING CONDITIONS

Table B.2: Aluminum zinc alloys.

Sample	Zn [wt. %] v_P [mm/min] \varnothing [μm]			Optic	Field of view [μm]	Pixel size [μm]	CCD w \times h	Energy [keV]	Transmission [%]	Exposure time [ms]	Projections	Scan time per block [min]	Blocks	Comment
A5Z6	5	1	3000	4	3785	1.85	2048 \times 2048	25	17	480	1501	12	1	
A5Z2	5	4	2000	4	3785	1.85	2048 \times 2048	25	27	480	1501	12	1	
A5Z4	5	10	1560	10	1515	0.74	2048 \times 2048	20	15	360	1501	12	2	
A10Z6	10	1	2400	4	3700	1.85	2048 \times 1249	30	24	1400	1501	35	2	
A10Z1	10	4	600	20	757	0.74	1024 \times 1024	17	20	200	1501	6	1	1
A10Z1	10	4	600	20	757	0.74	1024 \times 1024	17	20	200	1501	6	3	
A10Zx	10	4	1200	10	1515	0.74	2048 \times 2048	22	20	160	1501	11	2	
A10Zx2	10	4	3000	4	3785	1.85	2048 \times 1649	28	17	600	1501	24	2	
A10Z4	10	10	1200	10	1515	1.48	1024 \times 1024	22	19	80	1001	4	1	
A10Z4	10	10	1200	10	1515	0.74	2048 \times 2048	22	18	160	1501	11	2	
A10Z2	10	20	600	20	757	0.74	1024 \times 1024	17	15	200	1501	6	3	1
A20Z6	20	1	2400	4	3700	1.85	2048 \times 1249	32	17	1800	1501	45	2	
A20Z1	20	4	600	20	757	0.74	1024 \times 1024	20	18	120	1501	6	2	
A20Z2	20	4	600	20	757	0.74	1024 \times 1024	20	17	120	1501	6	3	
A20Z4	20	10	1200	10	1515	0.74	2048 \times 2048	23	20	650	1501	16	2	
A20Z3	20	20	600	20	757	0.74	1024 \times 1024	22	22	200	1501	6	2	
A35Z6	35	1	1200	10	1515	1.48	1023 \times 1023	30	17	450	1001	15	2	
A35Z6b	35	1	1400	10	1515	1.48	1024 \times 674	34	19	340	1001	6	1	
A35Z1	35	4	600	20	757	0.74	1024 \times 1024	22	17	200	1501	6	3	
A35Z2	35	4	1200	10	1515	0.74	2048 \times 2048	28	19	650	1501	16	3	
A35Z4	35	10	1200	10	1515	0.74	2048 \times 2048	28	19	650	1501	16	1	
A35Z3	35	20	600	20	757	0.74	1024 \times 1024	24	17	250	1501	6	2	
A50Z6a	50	1	700	20	757	0.74	1024 \times 1024	36	25	450	1001	8	2	
A50Z6b	50	1	700	20	757	0.74	1024 \times 1024	36	22	450	1001	8	2	
A50Zw	50	1	700	20	757	0.74	1024 \times 1024	32	27	360	1001	6	2	
A50Z1T	50	4	600	20	757	0.74	1024 \times 1024	28	17	250	1501	6	2	
A50Z2T	50	4	600	20	757	0.74	1024 \times 1024	28	20	250	1501	6	3	
A50Zx	50	4	600	20	757	0.74	1024 \times 1024	33	19	900	1501	23	2	
A50Z4	50	10	600	20	757	0.74	1024 \times 1024	33	19	900	1501	23	2	
A50Zy	50	10	700	20	757	0.74	1024 \times 1024	36	30	450	1001	8	2	

continued on the next page

Sample	Zn [wt. %]	v_P [mm/min]	\varnothing [μm]	Optic	Field of view [μm]	Pixel size [μm]	CCD w \times h	Energy [keV]	Transmission [%]	Exposure time [ms]	Projections	Scan time per block [min]	Blocks	Comment
A50Z3	50	20	600	20	757	0.74	1024 \times 1024	28	20	250	1501	6	1	
S1PD	55	4	600	20	757	0.74	1024 \times 1024	30	15	500	1501	19	1	
S2PD	55	4	600	20	757	0.74	1024 \times 1024	30	15	500	1501	19	5	
S3PD	55	4	600	20	757	0.74	1024 \times 1024	30	18	500	1501	19	1	
S3M	55	4	600	20	757	0.74	1024 \times 1024	30	16	500	1501	19	1	²
S3FE	55	4	600	20	757	0.74	1024 \times 1024	30	16	500	1501	19	1	³
A55Z4	55	10	600	20	757	0.74	1024 \times 1024	33	26	900	1501	23	2	
A55Z3	55	20	600	20	757	0.74	1024 \times 1024	33	26	900	1501	23	1	
A65Z1b	65	4	700	20	757	0.74	1024 \times 1024	36	22	450	1001	8	3	
A65Z4	65	10	700	20	757	0.74	1024 \times 1024	36	25	450	1001	8	2	
A82Z1	82	4	700	20	757	0.74	1024 \times 1024	40	16	660	1001	11	2	
A82Z4	82	10	700	20	757	0.74	1024 \times 1024	40	19	660	1001	11	2	
A82Z3	82	20	700	20	757	0.74	1024 \times 1024	40	17	660	1001	11	2	
D1PD	90	4	600	20	757	0.74	1024 \times 1024	38	13	650	1501	23	1	
D3PD	90	4	600	20	757	0.74	1024 \times 1024	38	13	650	1501	23	2	⁴
D3FE	90	4	600	20	757	0.74	1024 \times 1024	38	13	650	1501	23	1	³
A90Z4	90	10	700	20	757	0.74	1024 \times 1024	40	13	750	1001	13	2	
D5	90	20	600	20	757	0.74	1024 \times 1024	40	14	900	1501	23	2	

¹Sample scintillator distance was increased by 5 cm to increase edge contrast

⁴Non-overlapping scans, taken at different heights in the sample.

³Scan at the height corresponding to the eutectic temperature.

²Scan at the height corresponding to the temperature half way between the liquidus and the eutectic.

Resume

Jonathan Friedli
Les Riaux 68
1746 Prez-vers-Noréaz
Switzerland

+41 26 470 18 32

jonathan.friedli@a3.epfl.ch

Born on July 15, 1982
Single
Swiss citizen

Education

2007–2011	PhD degree in materials science and engineering, EPFL, Lausanne, Switzerland. Teaching assistant at the Computational materials laboratory (LSMX) of EPFL.
2001–2006	Engineering degree in Materials Science and Engineering at Ecole Polytechnique Fédérale de Lausanne (EPFL), Switzerland.
2004–2005	Exchange program between EPFL and Ecole Polytechnique de Montréal

Professional Experience

2006	Engineer work for Rolex SA in collaboration with the Computational materials laboratory (LSMX) at EPFL, Lausanne, Switzerland (4 months).
------	-------------------------------------------------------------------------------------------------------------------------------------------